7-11-2016

Bioengineering of 2D Nanomaterials via Green and Sustainable Routes

Ajith Pattammattel
University of Connecticut - Storrs, ajith.pattammattel@uconn.edu

Bioengineering of 2D Nanomaterials via Green and Sustainable Routes

Ajith Pattammattel

University of Connecticut, 2016

Abstract

Applications nanomaterials in biology resulted in many exciting fields of research such as nanomedicine, nanotheraputics and bionanosensors. The development of these fields highly depends on the nature and stability of nanomaterials in biological fluids. The poor stability of nanomaterials in biological media due to the aggregation and/or agglomeration with the biomolecules, particularly with serum proteins, is a challenging problem. Conversely, the defined formation of protein corona around the nanomaterials is very useful to improve properties such as cellular uptake and compatibility of the materials. The primary goal of this thesis will be to design and develop methods for biologically stable, nontoxic nanomaterials. In specific, the project is designed to biofunctionalize 2D nanolayers such as graphene and use the resulting materials in biology. The initial aims of this study was focused on the utility of graphene as a platform for the design of 'stable–on-the-table' biomaterials using the well-established techniques in our lab. The developments in this study will lead to the engineering of enzymatic biofuel cells with improved power density and sustainability. The second part of the project is to produce graphene in large quantities, in aqueous media using proteins as exfoliators. The produced graphene, called biographene, was characterized and used to evaluate the protein binding capabilities. Finally, graphene and other 2D analogues, such as Boron nitride (BN), Molybdenum sulfide (MoS_2) and Zirconium phosphate (ZrP), will be exfoliated in animal serum. Production and characterization of the layered materials in serum from bovine, porcine, chicken, rat, human and so on will be executed and the *in vivo* and *in vitro* toxicity will be tested for specific samples.

Bioengineering of 2D Nanomaterials via Green and Sustainable Routes

Ajith Pattammattel

MSc., Cochin University of Science and Technology, Kerala, India 2010

A Dissertation

Submitted in Partial Fulfillment of the

Requirements for the Degree of

Doctor of Philosophy

at the

University of Connecticut

2016

APPROVAL PAGE

Doctor of Philosophy Dissertation

Bioengineering of 2D Nanomaterials via Green and Sustainable Routes

Presented By

Ajith Pattammattel, M.Sc.

Major Advisor _____

Dr. Challa V. Kumar

Associate Advisor _____

Dr. Rajeshwari Kasi

Associate Advisor _____

Dr. Ashis K. Basu

University of Connecticut

2016

ACKNOWLEDGEMENT

I am thankful to my thesis advisor Dr. Challa V. Kumar for his excellent guiding for last 5 years to make this thesis real. Kumar group was the best place to learn about cutting edge research and the knowledge I have learned from him and the group is unimaginable. Dr. Kasi and Dr. Basu, my associate advisor also collaborated with me and both of them helped me to gain right scientific approach to problems. I also thank Dr. He for his time send for my general exam and thesis and his inputs will be useful in future. Dr. Selampinar was my teaching advisor for several years and she was an excellent personality. I am glad that I could make maintain a healthy relation with her even after teaching duties were over.

Current and past group members also helped me to learn experimental techniques, keeping the lab organized, and for having useful scientific discussions throughout my career here. I my grateful to Inoka for her mentoring and the excellent XRDs. Other past group members, Vindya, Ruma and Dhurga also supported me throughout their time here. Kyle Cole and Marc Novak are two individuals worth mentioning specifically for their friendliness and cool. Marc and myself had an excellent project were we enthralled by the results we got every day during the project. My colleagues Clive, Bobbi, Omkar, Caterina, Kyle Benson, Ananta, Melissa, Jinguwen and Megan supported me for last few years and the lab was so much fun with everyone. Clive was a wonderful person with so much patience and maturity, and thank you Clive for discussions about chemistry, basketball, football and cricket. Omkar was my best friend at UConn, it would have been a difficult time without him. I also acknowledge all the undergraduates worked with me: Megan, Christina, Esti, Jai, Shailaja Bree and Will. I thank all my collaborators, Paritosh, Deepa, Dr. Roshni, Subra (OSU), Prof. Dutta (OSU) and Oleg (NT-MDT) for their contributions to my thesis.

I would like to express my gratitude to the countless number of friends for their support for last decade. Amit and Abhay were very close to me and their views in life were valuable. Dr. Girish Kumar is my godfather, without him I would be at UConn and my gratitude to him is beyond any word I can write here.

Chaitra, my life partner, another gift UConn gave me. She is supporting me all the time we were together. Again, her place in my life cannot be written in words. I also thank all my family members for their support and keeping the family together. My new family, Chaitra's parents and Chandana is supporting us for last year, I thank them too. My sister, Paru, we went through so many hardships in life together, I am thankful to her for her support. My *Aliyan* Santhosh and niece Ponnu cheering me up all the time, they were real gifts. My *Achan,* who couldn't wait in this world to see this achievement, he wanted me to be a cook. I couldn't be one but I am closer as a chemist! I feel his presence at times, I am sure he is happy seeing me like this. My *Amma,* without whom I couldn't have paid my hostel bills in MSc, without whom I couldn't have gone to the best school, without whom I wouldn't be who I am now, is my inspiration, motivation and breath. It's not easy to thank her, but please be with me forever.

Finally, I thank my God, *Shiva*, for being in me. He is my subconscious mind, keeping my brain working and giving me whatever I have. He gave me whatever I asked and I am always thankful to him.

TABLE OF CONTENTS

List of Schemes

List of Figures

List of Tables

LIST OF ABBREVATIONS

α-ZrP	Layered Zirconium phosphate
TBA	Tetra Butyl Ammonium
DNA	Deoxy-ribose nucleic acid
RNA	Ribose nucleic acid
CD	Circular dichroism
TEM	Transmission electron microscopy
SEM	Scanning electron microscopy
DSC	Differential scanning calorimetry
XRD	X-ray diffractometry
EDX	Energy Dispersive X-Ray
FTIR	Fourier transform infrared spectroscopy
Hb	Hemoglobin
Mb	Myoglobin
CHT	Chymotrypsin
Lys	Lysozyme
Cyt	Cytochrome c
HRP	Horseradish peroxidase
GOX	Glucose oxidase

GO	Graphene Oxide
BSA	Bovine serum albumin
cBSA	Cataionized Bovine serum Albumin
HSA	Human serum albumin
ICPB	Ion-coupled protein binding
bZrP	Biofunctionalized α-ZrP
FITC	Fluorescein isothiocynate
TEPA	Tetraethylene pentamine
TMDs	Transition Metal Dichalogenides
BNI	Bio Nano Interface
EDC	1-Ethyl-3-(3-dimethylaminopropyl)carbodiimide

Introduction: Recent Advances in Biological interaction of 2D Nanomaterials

Applications of nanomaterials in biology stemmed in many exciting fields of research such as nanomedicine, nanotheraputics and bionanosensors.[1] The development of these fields highly depends on the stability and toxicity of materials in biological systems.[2] Stabilizing nanomaterials in biological media without harmful capping or stabilizing agents is an unaddressed challenge, which require immediate attention for the rapid development in the field. The major challenge in stabilizing these materials in protein rich biofluids is the non-specific adsorption of serum proteins, commonly known as protein corona, because this is initially noted for spherical nanoparticles.[2]

The consequences of corona formation are 1) binding of nanomaterials to non-targeted areas in drug delivery,[3] 2) aggregation induced precipitation of materials which could lead to lodges in veins or lungs[4] and 3) non-specific binding in biosensors.[5] Modification with hydrophilic polymers such as poly (etheleneglycol) (PEG) on nanosurface prevents non-specific adsorption to certain extent, but not completely.[5] Also, PEG functionalization (PEGylation) requires another step in the design of nanomaterials, where the material has to be amenable to the PEGylation conditions. Biological functionalization of nanosurface is another novel way to improve biological properties of nanomaterials.

Modification of nanosurfaces with biomolecules such as proteins, nucleic acids, and carbohydrates is recently used to improve the colloidal stability and compatibility of nanomaterials.[6] Both covalent and non-covalent chemistry can be used to biofunctionalize nanosurfaces, which can be post-modification or *in situ* at the synthesis step. Profound understanding of the interface of biomolecule and nanosurface is the basis for such modifications and manipulations of these functionalized materials. With the help of advanced spectroscopic and microscopic techniques, an overview of recent improvements in this field is described below.

1.1. Surface Chemistry of Nanolayers

Chemistry of nanomaterials is mostly controlled by elemental composition at the surface, the surface groups, particle size, area per unit mass etc. Ligands bound to nano layers function as a stabilizing agents in solution and to tune the size and optoelectronic nature by controlling the bulkiness, chain length and chemical reactivity of the ligand.[7] Nano layered materials usually possess surface functional groups, which stabilizes the nanosurface in colloidal form, present within its chemical structure. This is true for a class of materials known as layered double hydroxides [8] layered phosphates and phosphonates where charged hydroxides or phosphate groups provide charge separation between individual layers in solution.[9] Although these materials have colloidal stability by electrostatic repulsions, stabilizing agents are usually required for long term stability.[10,11]

Recent invention of single layer graphene paid much attention due to unexpected stability of single atom thick carbon layers, without folding or scrolling to low surface energy sphere or tube like structures.[12] Graphene was stable on different substrates such as Si wafer, Cu and also in

solutions phase in specific organic solvents.[13,14] The dispersive property of graphene in water was extremely poor due to the inherent hydrophobicity of carbon.[15] However, the oxidized from of graphene called graphene oxide (GO) possess oxygen functional groups to provide enough surface charge for aqueous stability.[16] After the invention of graphene materials such as transition metal dichalogenides (TMDs), h-Boron Nitride, MXenes and many more are synthesized or prepared from the bulk.[17,18,19] Exciting features of these materials are known or yet to be discovered for advanced electronics and functional materials.

Covalent chemistry of NMs is limited to the chemistry of surface coating groups except for strong gold-sulfur (Au-S) bonds.[20] Silica NPs can be modified using the hydroxyl group chemistry.[21] In case of nanolayers synthesized via chemical methods (top to bottom approach) reactive groups such as –COOH and NH_2 can be incorporated during synthesis. Graphene oxide with reactive hydroxyl, carboxyl and carbonyl groups can be easily modified using standard carbonyl chemistry.[22] The post modification of NMs is useful to control the surface properties required to tune the optoelectronic and biological properties.

1.2. Governing factors at Bio-Nano Interface

Macromolecular interactions between biomolecules and nanosurface are very complex because of its multivalent nature. Both targeted and non-targeted interactions can be tailored at this interface (**Figure 1.1**). Widely used specific binding strategies are mediated by streptavidin-avidin (or biotin),[23] sugar-lectin,[24] antigen antibody interactions etc, which has limitations in terms of scalability and cost.[25] Also post modification with one of the components is required to for this chemistry. However, controlling the non-targeted interactions, which does not require complementary ligands, is challenging. Bio-Nano interactions can be molecularly controlled by

electrostatic or weak non-covalent interactions, by appropriate design.[27] Most of these interactions are susceptible to solvent parameters such as, pH and ionic strength.[26] The major goal in controlling Bio-Nano interaction is to conserve the function of biomolecule under these non-physiological environments. Since the optimum activity of biomolecules are required for any biomedical devices or techniques, control of BioNano interface (BNI) deserves much importance.[27]

Non-covalent interactions at bio-nano interface using electrostatic interactions are very versatile approach, because no post modifications are required and both the surface and the biomolecule possess surface charges, hydrogen bonding donors and/or acceptors, hydrophobic sites etc. (**Figure 1.2**). The role of solvent and counter ions at charged interfaces is thoroughly investigated by our group and ion coupled protein binding (ICPB) mechanism was proposed.[26] according to ICPB mechanism, counter ions are released from the interface when a positive protein interacts with negative substrate. On the other hand, sequestration of ions to the interface is required for the interaction of a negative protein and negative surface. Immobilization of DNA to mica surface achieved only in presence of divalent metal ions underlines the ion sequestration mechanism.[28]

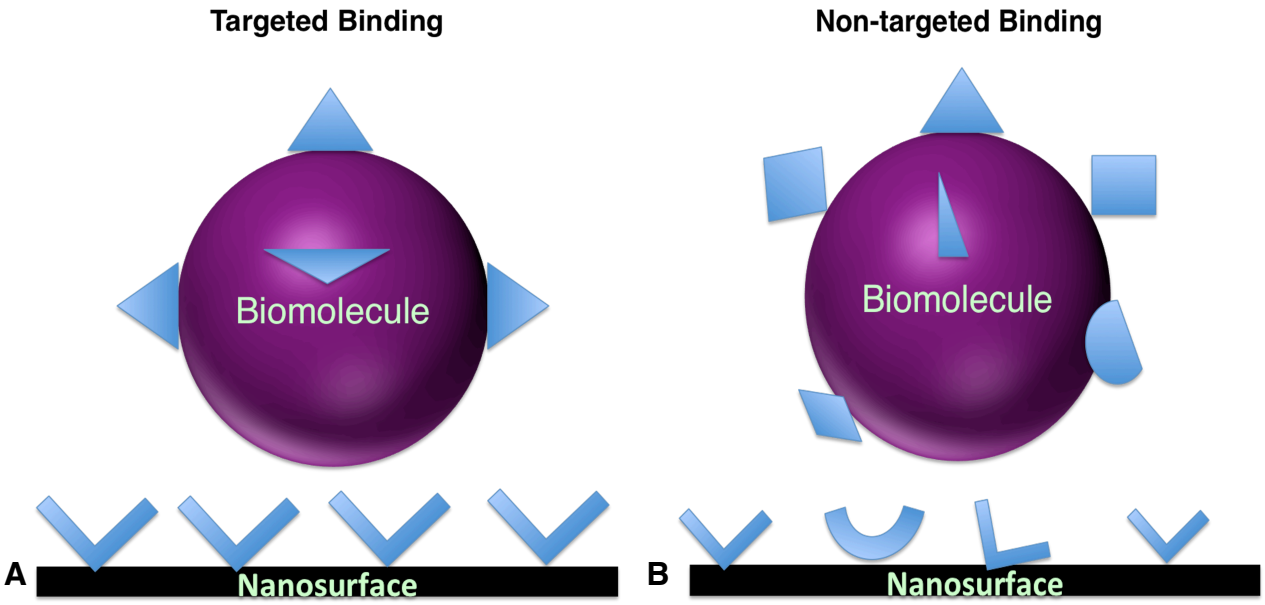

Figure 1.1. Targeted (A) and non-targeted (B) binding at bionano interfaces. Complementary groups are introduced at biomolecule and nanosurface for targeted binding, whereas random binding of groups on the biomolecule to the surface groups results in non-targeted binding.

Interaction between positive and negative groups by electrostatic force is used at for applications in sensing and drug delivery using nanosurfaces. DNA or RNA with phosphate backbone form salt bridges with amino groups in polymers (eg; polyetheleneimine), widely used for applications such as siRNA delivery.[29] On the other hand, lysine and arginine side chains can also have affinity phosphate, carboxyl or hydroxyl groups. Covalent like nature of arginine-phosphate interaction is noted because of cooperative salt bridges between the groups that from stable hexagonal structure.[30] Non-charged surface biomolecule interactions usually driven by hydrophobic and van der Waal's forces.

Hydrophobic interactions are successfully used to control protein nanolayers interactions particularly for hydrophobic proteins. [31] Lipase was immobilized to polystyrene and hydrophobically modified agarose by using strong hydrophobic interactions.[32] This interaction led to the hyperactivation of enzymatic activity of lipase called as interfacial activation. Interaction of carbon surfaces (such as in CNT, graphene or GO) with proteins, peptides or DNA is also hydrophobic in nature.[33] Because of the same, proteins tend to denature on GO by exposing the inner hydrophobic amino acids in the secondary structure.[34] The hydrophobic interaction between graphene and DNA was used to fabricate 'turn-on' fluorescent sensors.[35] The mechanistic aspect of hydrophobic interactions provide another key to control this interactions.

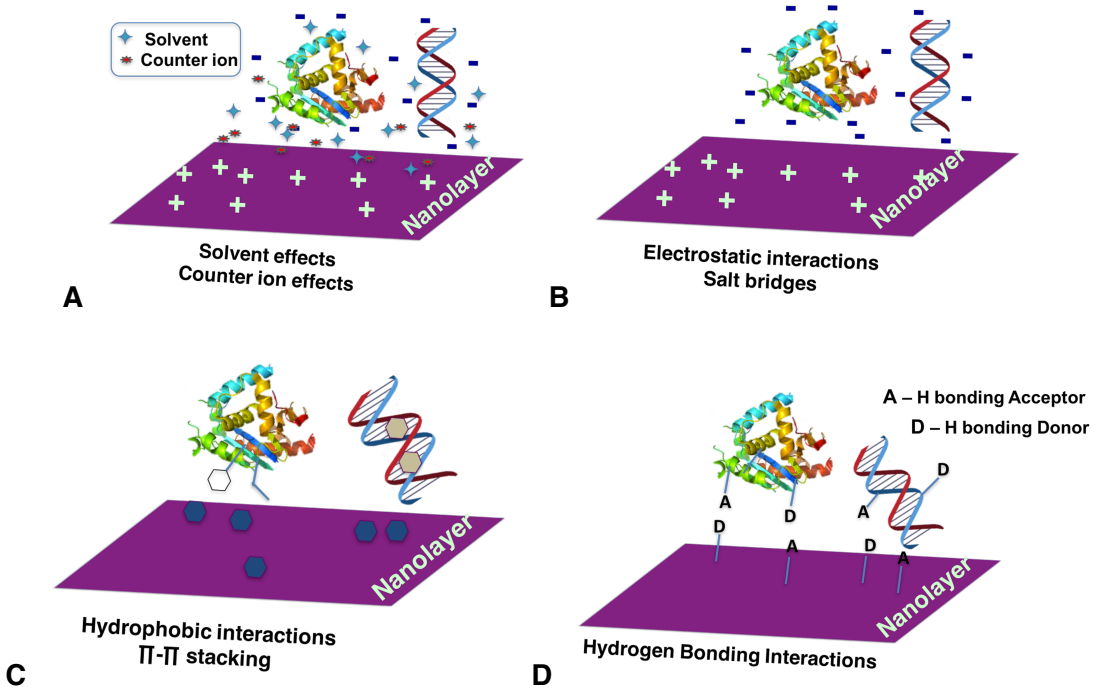

Figure 1.2. Major non-targeted interactions at Bio-nanolayer interfaces.

The hydrophobic interaction of proteins with substrates was proposed to be entropic in nature.[36] Interaction of hydrophobic surfaces water molecules and counter ions from the interface moves to the bulk results in increase in entropy of water and ions. This mechanism is supported by measuring water diffusion constant at the interfaces of mussel foot protein (mfp) on surfaces.[37] When weakly hydrated amino acids in the protein approaches to hydrophobic styrene surface, strong eviction of water molecules from the surface. As a result, diffusion time of water at the interface increased from 335 to 842 ps at pH 5.5). The role of water in hydrophobic interactions is irrefutable but actual thermodynamics behind this interaction is a mystery.[38]

Interactions at BNI are also influenced by heterogeneity, edges, roughness and defects at the surfaces.[27] There could also be hot spot residues on the protein or DNA, which strongly interacts with the surfaces.[39] More efforts in this area with the help of computational analysis needed to define interactions at BNI in future.

1.3. Biological Functionalization of Nanolayers

Surface functionalization of NMs with biomolecules to improve its biological or non-biological function is usually termed as biofunctionalization.[40] Biofunctionalization can be executed to nanomaterials either *in situ* or by post modification steps, and the latter one is the most common approach. Post modification is recommended when biomolecule does interfere with the synthesis of nanomaterial. Also any biological activity of the capping agent can be avoided by substituting them with biomolecules at the post modification step.[41] The disadvantage with the post modification is the lack of stability of nanomaterials to the biological molecules or fluids.

When NMs are introduced to biofluids, serum proteins segregate around the nanosurface called as biocorona (or protein corona) formation.[42]

Protein corona on nanosurface causes significant increase in size and interferes with the surface chemistry of the material.[42] On contrary, studies protein corona masks the toxicity of the material by reducing the exposure of the materials to the biological systems.[43] But protein corona severely affects the specificity of the nanomaterials, if they are targeted to a specific region or cells.[44] The field of nanomedicine faces a big challenge in recent times due to the non-specific nature of the nanoparticles in biological fluids. A new study shows that only 0.7% of the total nanomaterial loaded with drug molecules, injected to an *in vivo* system has delivered to the targeted region (average of 117 independent experiments).[45] This mean 99.3% of the particles are accumulated in the other part of the body; usually spleen, liver or kidney causes damage to the organ or ends up in mortality of the animal. These findings point out to the need of biofunctionalization to keep the nanoparticle intact in body fluids before going to *in vivo* models. Another consequences of protein corona formation is the accumulation of nanomaterials in liver, spleen and kidney, causes acute or chronic toxic effects.[45]

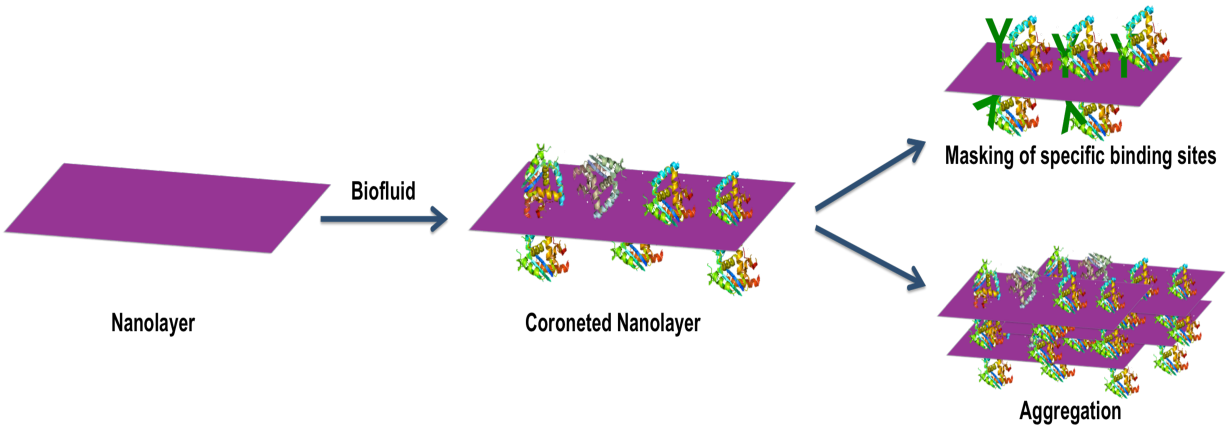

Figure 1.3. Bio-corona formation on nanolayers and its consequences.

Nanotoxicity is a major concern in nanotechnology field for last two decades, particularly for materials with applications in biomedical and environmental applications.[46] Well dispersed nanomaterials in cell culture or blood stream of an *in vivo* organism is necessary to evaluate the extent toxicity. However, aggregation or agglomeration of the materials driven by corona formation interferes the toxicity analysis and overestimated exposure levels may be reported.[47] In other words, aggregated portion of the material will not be in contact with the cell or animal will also be taken in account in the dose dependent studies. For example, assume that 50% of the material precipitates when added to cell culture media and the remaining 50% is well dispersed. The well-dispersed portion is responsible for the toxicity to the cells because it is in contact. But the reported dose for the exposure of the nanomaterial will be reported for 100%, although 50% were inert. It is also noted that dispersible portion of the aggregated nanoparticles are more toxic than well-dispersed particles in case of carbon nanotubes.[48] This inconsistency in evaluation nanotoxicity of materials from the lack of colloidal stability can be solved by appropriate biofunctionalization.

Preparation of NMs in or with the help of biomolecules is a probable solution to the challenges associated with corona formation. Unfortunately, few attempts are done this area and those materials are rarely used for application or toxicity analysis. Nanoparticles and nanoclusters of gold and silver particles are synthesized using proteins or DNA.[49] For example, gold nano clusters are synthesized using the reactivity of cysteine residue (34^{th} position) in BSA.[50] Nanolayered materials are delaminated from the bulk using proteins as exfoliating agents, where the 3D structure of the protein prevents the individual layers from aggregation. The avenue of biomolecules and NMs offer opportunities to explore new green synthetic routes for well-dispersed materials in biofluids.

1.4. Toxicity of Nanolayers

Toxic effects of NMs to humans and environment became a major concern after the nano-revolution in the past few decades.[51] The adverse effect of NMs on living organisms and environment is different from that of molecules because of their size, shape and surface chemistry.[52] Primarily, the biological effects of NMs are usually studied using mammalian cells as model systems. Most of these studies are carried out to analyze the cytotoxicity of NMs to cell lanes, after incubating certain doses of the material with the cell media. Nanoparticles are widely studied systems to evaluate the toxic effect of NMs and the effect of size, surface functionalization is noted. Toxicity of layered materials is initially examined for nanoclay materials.[53]

Nanoclay materials are found to be little or no toxicity in *in vivo* models.[54] Recent invention of graphene and related materials resulted in toxicity analysis of these layered materials in detail. Both in vivo and in vitro models suggest that oxidized graphene derivates, called graphene oxide (GO) and reduced GO (rGO) is very toxic to the model systems (**Table 1.1**). Most of the studies indicates the generation of reactive oxygen species in the presence of these materials, leading to cell death or inflammation. Since GO is defective and mass production is limited because of the synthetic requirements, dispersible graphene is particularly attractive.

Toxicity study of graphene is well known in the field because of low availability of water dispersible graphene. However, studies using aggregated graphene and polymer supported graphene showing inconsistent results (**Table 1.1**). In general, well-dispersed graphene (in polymer solutions) are less toxic comparable aggregated graphene platelets in solution. These

studies point out to the need of well dispersed carbon materials in biological fluids to improve the biocompatibility of graphene and its derivatives.

Table 1.1. Toxicity of Graphene tested in in vitro and in vitro models

Material	Properties	Model	Dose	Results
Graphene (CVD)[55]	3-5 layers Charge = -36 mV (in water)	PC12 Cells	0.1-100 μg/mL	ROS generation, Apoptosis induction
Graphene Platelets (Sonication in 2% Pluronic F108)[56]	Thickness = 5 nm (5-15 layers)	Mice	50 μg/animal	No direct toxicity from graphene Well dispersed graphene was less toxic than aggregates
Graphene Nano-platelets (Plasma exfoliated, dispersed in 0.5% BSA)[57]	10 nm thick 5 μm in size	Mice	50 µg/animal (aspiration) 5 µg/animal (injection)	Lung and Pleural inflammation Frustrated phagocytocis ROS, pro inflammatory cytokine activation
Aggregated	3-5 nm thickness	Mice	50 μg/animal	Lodges the airways in lung and induces local

graphene (Flocculation of graphite)[58]	when dispersed in 2% Pluronic acid			fibrotic response
Multilayer graphene (Sonication of thermally expanded graphite)[59]	30 layers	Nematode	50-250 μg/mL	No effect on both longevity and reproduction
NanoGO-PEG (Hummers Method)[60]	Well-dispersed nanoGO-PEG 5-50 nm size	HCT-116	0.5-150 μg/mL	No or reduced toxicity
Single layer GO (Modified Hummers method)[61]	<500 nm size	A549	8-125 μg/mL	No toxicity up to 100 μg/mL Toxicity due to synthetic and metallic impurities

				are noted
BSA coated GO (Hummers method)[62]	420-860 nm size	C2C12	10-100 μg/mL	No effect on metabolic activity
rGO (Hummers /Hydrazine)[63]	1.0 nm thickness	A549	20-85 μg/mL	20% viability at 85 μg/mL
rGO (Hummers/ Thermal reduction)[64]	Bilayer 0.2-5 μm	mice	250 μg/kg	Less platelet aggregation compared to GO

1.5. Conclusions, Challenges and Perspectives

Understanding of bionano interface in a profound manner is necessary for the applications of nanomaterial in cell biology, biomedical field and in nanomedicine. The applications of NMs in biological filed is highly depend on two factors 1) stability of NMs in biological media and 2) toxicity of NMs to cells or animals. Stability of nanomaterials in biological media is poor because of protein corona formation, which also affects the performance of NM in the system by masking the target sites in the NMs. The corona formation can overcome by appropriate post modifications and *in situ* biofunctionalization of NMs.[5] Manipulation of BNI at molecular level is needed for these functionalization strategies. Concerns about nanotoxicity is the other avenue

hampering the biological applications of NMs. Studies show that layered materials are toxic or nontoxic based on their composition (**Table 1.1**). Large interest in graphene materials motivated several groups to evaluate material toxicity of GO, rGO and pristine graphene. Graphene platelets and aggregated found to be less toxic compared to oxidized counterparts. However, several inconsistencies in graphene toxicity analysis is noted in many cases, originated because of poor dispersive properties. Major attention is needed in this field to define the toxicity of graphene under completely dispersed graphene in biological liquids and the role of dispersibility, size, number of layers, extent of oxidation and defects is also need to be documented. This is possible only by preparation these materials under biologically benign conditions with minimum chemical treatments. Bioengineering of NMs becomes extremely relevant in this context.

1.6. Properties of proteins used in this thesis

Protein	pI /net charge at pH 7	Mol. Wt. (kDa)	Key amino acid composition
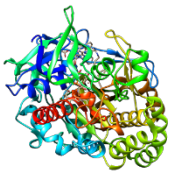 Glucose Oxidase (GOx)[65] *(Aspergillus niger)*	4.6/-27	160	Lys – 30 Arg – 22 Asp – 36 Glu – 30
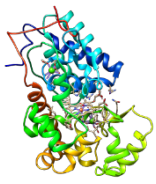 Horseradish peroxidase (HRP)[66]	6.3/-1	34	Lys – 6 Arg – 21 Asp – 21 Glu – 7

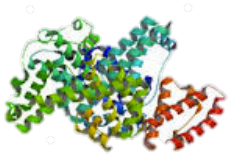 Bovine Serum Albumin (BSA)[67]	5.6/-17	66	Lys – 59 Arg – 23 Asp – 40 Glu – 59
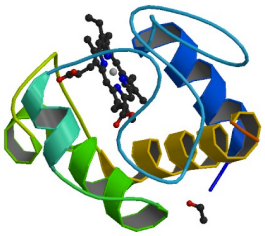 Cytochrome *c*[68] (equine heart)	10/+13	26	Lys – 32 Arg – 4 Asp – 10 Glu – 13
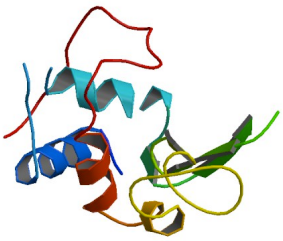 Lysozyme (Lyz)[69] (Chicken egg)	11.3/+8	14	Lys – 6 Arg – 11 Asp – 7 Glu – 2
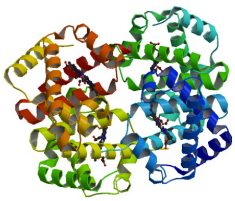 Bovine Hemoglobin (Hb)[70]	6.8/+1	62	Lys – 48 Arg – 14 Asp – 34 Glu – 26

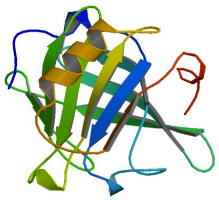 Beta-lactoglobulin (BLG) (Bovine Milk)[71]	5.1/-18	37	Lys – 30 Arg – 6 Asp – 20 Glu – 16
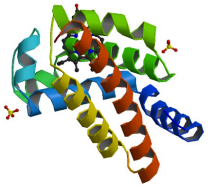 Bovine Myoglobin (Mb)[72]	6.8/0	17	Lys – 19 Arg – 2 Asp – 8 Glu – 13
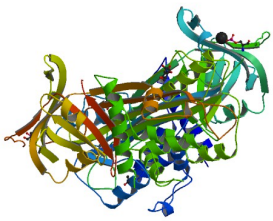 Ovalbumin (OVL) (Chicken egg)[73]	4.9/-12	43	Lys – 20 Arg – 15 Asp – 14 Glu – 33
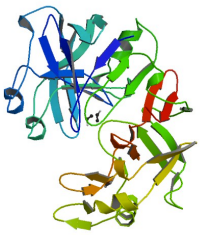 Bovine Pepsin A (PepA)[74]	1/-40	35	Lys – 1 Arg – 2 Asp – 30 Glu – 13

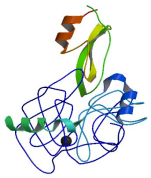 Bovine Trypsin (Trp)[75]	9.3/+7	30	Lys – 18 Arg – 8 Asp – 8 Glu – 6
 Bovine Catalase (Cat)[76]	5.4/-5	60 (mono)	Lys – 28 Arg – 32 Asp – 39 Glu – 26
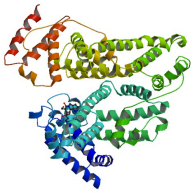 Human Serum Albumin (HSA)[77]	4.7/-15	66	Lys – 59 Arg – 24 Asp – 36 Glu – 62
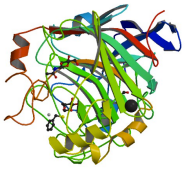 Cellulase *(Trichoderma reesei)*[78]	5.3/-24	46	Lys – 13 Arg – 7 Asp – 24 Glu – 20
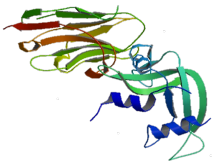 RNase A[79] (Bovine)	9.3/+4	14	Lys – 10 Arg – 4 Asp – 5 Glu – 5

1.7. Properties of Materials used in this thesis

1. α - Zirconium Phosphate (α - ZrP)

α - ZrP is phosphate based layered material with general Formula Zr(HPO4)2·nH2O. The structure of α - ZrP composed for hexavalent Zr(IV) cation, bridged to tetravalent phosphorous atom through divalent oxygens (**Figure 1.4.A**). In the crystal structure, α - ZrP layers stack where the phosphate groups are facing each other (**Figure 1.4.B**), with 7.6 Å interlayer distance.[80] Free oxygen atoms exposed to the solvent, when exfoliated attributed to the stability of layered structure in solution. Phosphate groups the structure results in unit negative charge in every very 24 $Å^2$ area, when deprotonated.[81] The surface charge of α - ZrP makes it attractive for electrostatic interactions with metal ions, proteins, DNA and small molecules.

Key Properties

Surface Area: 2.4 m^2/g (BET)[82]

Proton conductivity: 10^{-5} - 10^{-6} s cm^{-1} (25°C, 90% RH)[83]

Zeta potential; ~ -40 mV (pH 7.0)[84]

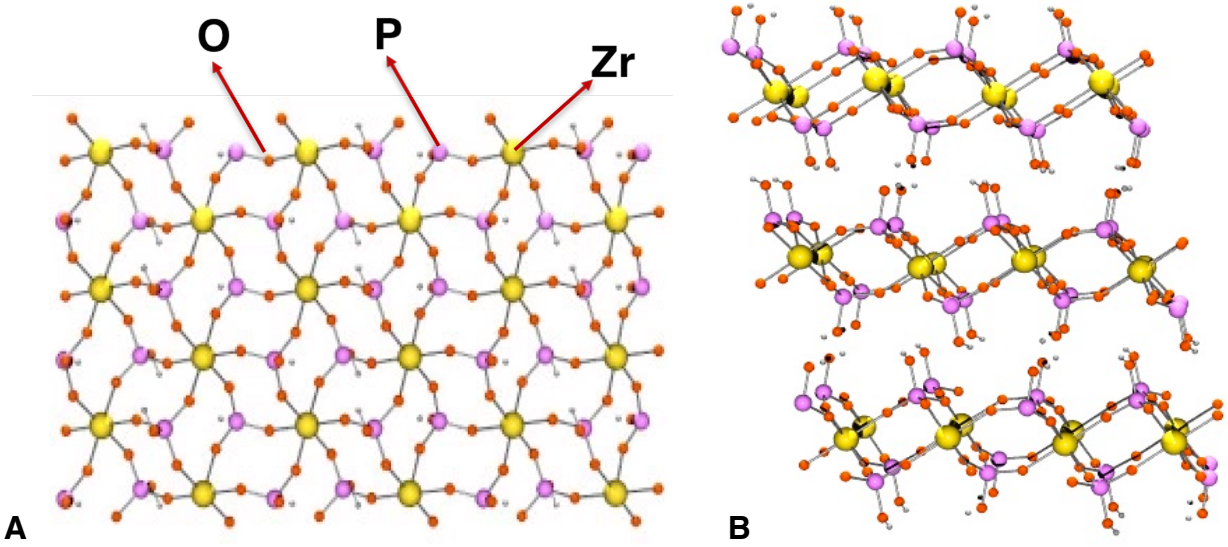

Figure 1.4.A. Structure of α - ZrP. **B.** Alignment of α - ZrP layers in crystal structure.

2. Graphene Oxide

Graphene Oxide (GO) is the water dispersible graphene derivative derived from graphite via strong oxidation procedure known as Hummers method.[85] Graphene does not mix with water because of its inherent hydrophobic nature, but the oxygen functional groups on GO provides surface charge and hydrophilicity to the sheets makes it dispersible in water. Typically, C:O of 2.1 to 2.9 was noted for GO produced using Hummers method, and the oxygen portion present as hydroxyl, carboxyl, and epoxy groups.[86] In a packed structure GO shows 7 Å spacing corresponding to the carbon layers and intercalated water molecules. GO shows insulation property in contrary to high carrier mobility of pristine graphene but the solution processability of GO makes it attractive for wide applications in materials field.[87]

Key properties

Surface Area: 760 m^2/g[88]

Electrical Resistivity: 10^3 kΩ/sq (25°C)[89]

Thermal Conductivity: 900 ± 45 W m−1 K−1[90]

Young's Modulus: ~ 207 GPa (single layer)[91]

Tensile Strength: 32 GPa[91]

Zeta potential; ~ -50 mV (pH 7.0)[92]

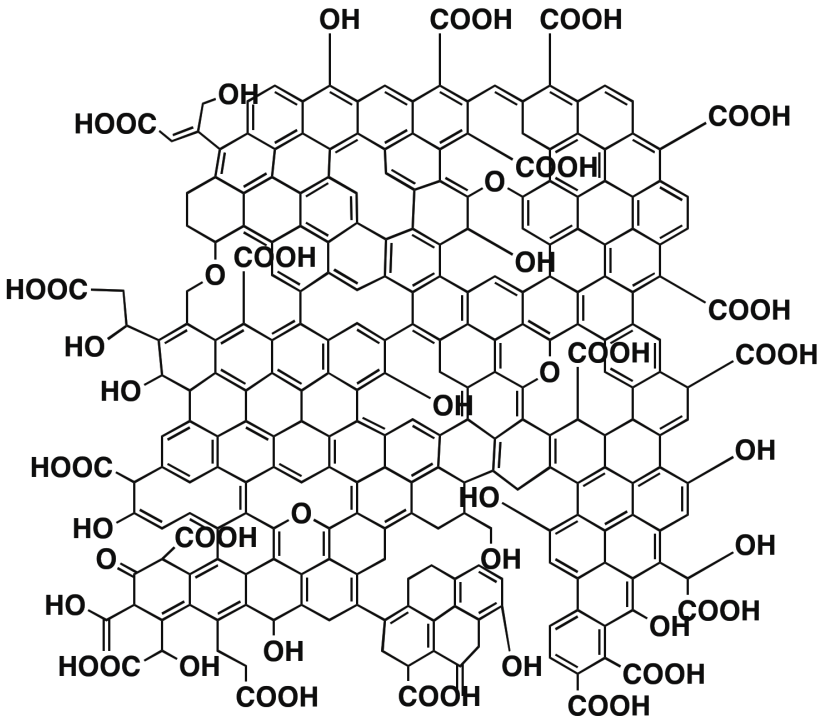

Figure 1.5. Structure of graphene oxide

3. Graphene

Graphene, one atom thick sp2 carbon layers, known as the 'wonder material' of 21st century. Graphene has amazing electronic and material properties compared to any existing material. Structure of graphene can be visualized as the ultimate member of poly cyclic aromatic hydrocarbon family. Graphene is prepared by bottom down approach from parent graphite by exfoliation process or by bottom up approach from carbon sources (such as methane) by chemical vapor deposition like methods.[93] Key properties of graphene is noted below.

Theoretical surface area: 2360 m^2/g[94]

Thermal conductivity: ~5000 W/mK[95]

Young's modulus: ~1 TPa[96]

Optical transmittance: ~97.7% (single layer)[93]

Tensile Strength: 130 GPa[97]

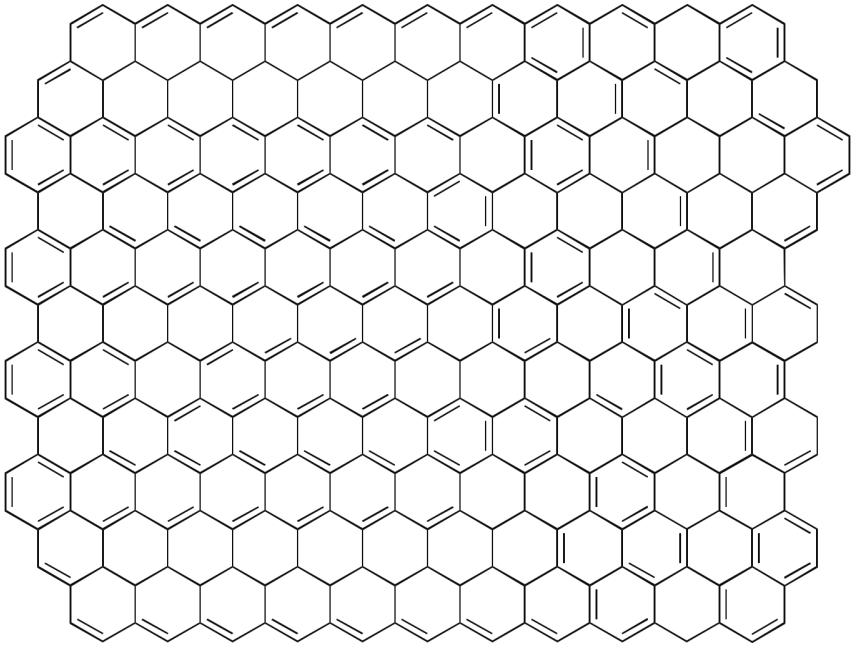

Figure 1.6. Structure of graphene

References

1. (a) Oliveira, O. N.; Iost, R. M.; Siqueira, J. R.; Crespilho, F. N.; Caseli, L., Nanomaterials for Diagnosis: Challenges and Applications in Smart Devices Based on Molecular Recognition. *J. Appl. Mater. Interfaces* **2014**; (b) Chung, C.; Kim, Y.-K.; Shin, D.; Ryoo, S.-R.; Hong, B. H.; Min, D.-H., Biomedical Applications of Graphene and Graphene Oxide. *Acc. Chem. Res.* **2013,** *46*, 2211-2224; (c) Riehemann, K.; Schneider, S. W.; Luger, T. A.; Godin, B.; Ferrari, M.; Fuchs, H., Nanomedicine—Challenge and Perspectives. *Angew. Chem. Int. Ed.* **2009,** *48*, 872-897; (d) Yang, K.; Feng, L.; Shi, X.; Liu, Z., Nano-graphene in biomedicine: theranostic applications. *Chem. Soc. Rev.* **2013,** *42* , 530-547.

2. Pino, P. d.; Pelaz, B.; Zhang, Q.; Maffre, P.; Nienhaus, G. U.; Parak, W. J., Protein corona formation around nanoparticles - from the past to the future. *Materials Horizons* **2014,** *1*, 301-313.

3. Pearson, R. M.; Juettner, V.; Hong, S., Biomolecular Corona on Nanoparticles: A Survey of Recent Literature and its Implications in Targeted Drug Delivery. *Frontiers in Chemistry* **2014,** *2*.

4. Serpooshan, V.; Mahmoudi, M.; Zhao, M.; Wei, K.; Sivanesan, S.; Motamedchaboki, K.; Malkovskiy, A. V.; Goldstone, A. B.; Cohen, J. E.; Yang, P. C.; Rajadas, J.; Bernstein, D.; Woo, Y. J.; Ruiz-Lozano, P., Protein Corona Influences Cell–Biomaterial Interactions in Nanostructured Tissue Engineering Scaffolds. *Advanced Functional Materials* **2015,** *25*, 4379-4389.

5. Dai, Q.; Walkey, C.; Chan, W. C. W., Polyethylene Glycol Backfilling Mitigates the Negative Impact of the Protein Corona on Nanoparticle Cell Targeting. *Angewandte Chemie International Edition* **2014,** *53*, 5093-5096.

6. Ju, H.; Zhang, X.; Wang, J., Biofunctionalization of Nanomaterials. In *NanoBiosensing: Principles, Development and Application*, Springer New York: New York, NY, 2011; pp 1-38.

7. Krommenhoek, P. J.; Wang, J.; Hentz, N.; Johnston-Peck, A. C.; Kozek, K. A.; Kalyuzhny, G.; Tracy, J. B., Bulky Adamantanethiolate and Cyclohexanethiolate Ligands Favor Smaller Gold Nanoparticles with Altered Discrete Sizes. *ACS Nano* **2012,** *6* (6), 4903-4911.

8. He, J.; Wei, M.; Li, B.; Kang, Y.; Evans, D. G.; Duan, X., Preparation of Layered Double Hydroxides. In *Layered Double Hydroxides*, Duan, X.; Evans, D. G., Eds. Springer Berlin Heidelberg: Berlin, Heidelberg, 2006; pp 89-119.

9. Cao, G.; Hong, H. G.; Mallouk, T. E., Layered metal phosphates and phosphonates: from crystals to monolayers. *Accounts of Chemical Research* **1992,** *25*, 420-427.

10. Adachi-Pagano, M.; Forano, C.; Besse, J.-P., Delamination of layered double hydroxides by use of surfactants. *Chemical Communications* **2000,** 91-92.

11. Feng, H.; Hu, Z.; Liu, X., Facile and efficient exfoliation of inorganic layered materials using liquid alkali metal alloys. *Chemical Communications* **2015,** *51*, 10961-10964.

12. Novoselov, K. S.; Geim, A. K.; Morozov, S. V.; Jiang, D.; Zhang, Y.; Dubonos, S. V.; Grigorieva, I. V.; Firsov, A. A., Electric Field Effect in Atomically Thin Carbon Films. *Science* **2004,** *306*, 666-669.

13. Batzill, M., The surface science of graphene: Metal interfaces, CVD synthesis, nanoribbons, chemical modifications, and defects. *Surface Science Reports* **2012,** *67*, 83-115.

14. Coleman, J. N., Liquid-Phase Exfoliation of Nanotubes and Graphene. *Advanced Functional Materials* **2009,** *19*, 3680-3695.

15. Li, L.; Bedrov, D.; Smith, G. D., Water-Induced Interactions between Carbon Nanoparticles. *The Journal of Physical Chemistry B* **2006,** *110*, 10509-10513.

16. Si, Y.; Samulski, E. T., Synthesis of Water Soluble Graphene. *Nano Letters* **2008,** *8*, 1679-1682.

17. Chhowalla, M.; Shin, H. S.; Eda, G.; Li, L.-J.; Loh, K. P.; Zhang, H., The chemistry of two-dimensional layered transition metal dichalcogenide nanosheets. *Nat Chem* **2013,** *5*, 263-275.

18. Golberg, D.; Bando, Y.; Huang, Y.; Terao, T.; Mitome, M.; Tang, C.; Zhi, C., Boron Nitride Nanotubes and Nanosheets. *ACS Nano* **2010,** *4*, 2979-2993.

19. Anasori, B.; Xie, Y.; Beidaghi, M.; Lu, J.; Hosler, B. C.; Hultman, L.; Kent, P. R. C.; Gogotsi, Y.; Barsoum, M. W., Two-Dimensional, Ordered, Double Transition Metals Carbides (MXenes). *ACS Nano* **2015,** *9*, 9507-9516.

20. Pensa, E.; Cortés, E.; Corthey, G.; Carro, P.; Vericat, C.; Fonticelli, M. H.; Benítez, G.; Rubert, A. A.; Salvarezza, R. C., The Chemistry of the Sulfur–Gold Interface: In Search of a Unified Model. *Accounts of Chemical Research* **2012,** *45*, 1183-1192.

21. Morrow, B. A.; McFarlan, A. J., Chemical reactions at silica surfaces. *Journal of Non-Crystalline Solids* **1990,** *120*, 61-71.

22. Dreyer, D. R.; Park, S.; Bielawski, C. W.; Ruoff, R. S., The chemistry of graphene oxide. *Chemical Society Reviews* **2010,** *39*, 228-240.

23. Hsing, I. M.; Xu, Y.; Zhao, W., Micro- and Nano- Magnetic Particles for Applications in Biosensing. *Electroanalysis* **2007,** *19* (7-8), 755-768.

24. Dai, Z.; Kawde, A.-N.; Xiang, Y.; La Belle, J. T.; Gerlach, J.; Bhavanandan, V. P.; Joshi, L.; Wang, J., Nanoparticle-Based Sensing of Glycan–Lectin Interactions. *Journal of the American Chemical Society* **2006,** *128*, 10018-10019.

25 . Wang, S.; Mamedova, N.; Kotov, N. A.; Chen, W.; Studer, J., Antigen/Antibody Immunocomplex from CdTe Nanoparticle Bioconjugates. *Nano Letters* **2002,** *2*, 817-822.

26. Deshapriya, I. K.; Kumar, C. V., Nanobio Interfaces: Charge Control of Enzyme/Inorganic Interfaces for Advanced Biocatalysis. *Langmuir* **2013,** *29*, 14001-14016.

27. Nel, A. E.; Madler, L.; Velegol, D.; Xia, T.; Hoek, E. M. V.; Somasundaran, P.; Klaessig, F.; Castranova, V.; Thompson, M., Understanding biophysicochemical interactions at the nano-bio interface. *Nat Mater* **2009,** *8*, 543-557.

28. Pastré, D.; Piétrement, O.; Fusil, S.; Landousy, F.; Jeusset, J.; David, M.-O.; Hamon, L.; Le Cam, E.; Zozime, A., Adsorption of DNA to Mica Mediated by Divalent Counterions: A Theoretical and Experimental Study. *Biophysical Journal* **2003,** *85*, 2507-2518.

29. Nimesh, S.; Chandra, R., Polyethylenimine nanoparticles as an efficient in vitro siRNA delivery system. *European Journal of Pharmaceutics and Biopharmaceutics* **2009,** *73*, 43-49.

30 . Woods, A. S.; Ferré, S., Amazing Stability of the Arginine–Phosphate Electrostatic Interaction. *Journal of Proteome Research* **2005,** *4* (4), 1397-1402.

31. Secundo, F., Conformational changes of enzymes upon immobilisation. *Chemical Society Reviews* **2013,** *42* (15), 6250-6261.

32. Rodrigues, R. C.; Ortiz, C.; Berenguer-Murcia, A.; Torres, R.; Fernandez-Lafuente, R., Modifying enzyme activity and selectivity by immobilization. *Chemical Society Reviews* **2013,** *42* (15), 6290-6307.

33. Nepal, D.; Geckeler, K. E., Interactions of Carbon Nanotubes with Biomolecules: Advances and Challenges. In *Advanced Nanomaterials*, Wiley-VCH Verlag GmbH & Co. KGaA: 2010; pp 715-742.

34. Zhang, Y.; Zhang, J.; Huang, X.; Zhou, X.; Wu, H.; Guo, S.: Assembly of Graphene Oxide–Enzyme Conjugates through Hydrophobic Interaction. *Small* **2012**, *8*, 154-159.

35.Hu, Y.; Li, F.; Han, D.; Niu, L., Graphene for DNA Biosensing. In *Biocompatible Graphene for Bioanalytical Applications*, Springer Berlin Heidelberg: Berlin, Heidelberg, 2015; pp 11-33.

36 . Meyer, E. E.; Rosenberg, K. J.; Israelachvili, J., Recent progress in understanding hydrophobic interactions. *Proceedings of the National Academy of Sciences* **2006,** *103*, 15739-15746.

37. Akdogan, Y.; Wei, W.; Huang, K.-Y.; Kageyama, Y.; Danner, E. W.; Miller, D. R.; Martinez Rodriguez, N. R.; Waite, J. H.; Han, S., Intrinsic Surface-Drying Properties of Bioadhesive Proteins. *Angewandte Chemie International Edition* **2014,** *53*, 11253-11256.

38. Blokzijl, W.; Engberts, J. B. F. N., Hydrophobic Effects. Opinions and Facts. *Angewandte Chemie International Edition* **1993,** *32*, 1545-1579.

39. T. M.; Kolinski, M.; Filipek, S.; Mukerjee, S.; Kannan, A. M.; Thavasi, V.; Ramakrishna, S.; Chin, M.; Somasundaran, P.; Viswanathan, S.; Keles, R. S.; Renugopalakrishnan, V., Protein hot spots at bio-nano interfaces. *Materials Today* **2011,** *14*, 360-365.

40. Ju, H.; Zhang, X.; Wang, J., Biofunctionalization of Nanomaterials. In *NanoBiosensing: Principles, Development and Application*, Springer New York: New York, NY, 2011; pp 1-38.

41. Duan, H.; Wang, D.; Li, Y., Green chemistry for nanoparticle synthesis. *Chemical Society Reviews* **2015,** *44*, 5778-5792.

42. Pino, P. d.; Pelaz, B.; Zhang, Q.; Maffre, P.; Nienhaus, G. U.; Parak, W. J., Protein corona formation around nanoparticles - from the past to the future. *Materials Horizons* **2014,** *1*, 301-313.

43. Tenzer, S.; Docter, D.; Kuharev, J.; Musyanovych, A.; Fetz, V.; Hecht, R.; Schlenk, F.; Fischer, D.; Kiouptsi, K.; Reinhardt, C.; Landfester, K.; Schild, H.; Maskos, M.; Knauer, S. K.; Stauber, R. H., Rapid formation of plasma protein corona critically affects nanoparticle pathophysiology. *Nat Nano* **2013,** *8*, 772-781.

44. Salvati, A.; Pitek, A. S.; Monopoli, M. P.; Prapainop, K.; Bombelli, F. B.; Hristov, D. R.; Kelly, P. M.; Aberg, C.; Mahon, E.; Dawson, K. A., Transferrin-functionalized nanoparticles lose their targeting capabilities when a biomolecule corona adsorbs on the surface. *Nat Nano* **2013,** *8*, 137-143.

45. Wilhelm, S.; Tavares, A. J.; Dai, Q.; Ohta, S.; Audet, J.; Dvorak, H. F.; Chan, W. C. W., Analysis of nanoparticle delivery to tumours. *Nature Reviews Materials* **2016,** *1*, 16014.

46. Donaldson, K.; Poland, C. A., Nanotoxicity: challenging the myth of nano-specific toxicity. *Current Opinion in Biotechnology* **2013,** *24*, 724-734.

47. Albanese, A.; Chan, W. C. W., Effect of Gold Nanoparticle Aggregation on Cell Uptake and Toxicity. *ACS Nano* **2011,** *5*, 5478-5489.

48. Wick, P.; Manser, P.; Limbach, L. K.; Dettlaff-Weglikowska, U.; Krumeich, F.; Roth, S.; Stark, W. J.; Bruinink, A., The degree and kind of agglomeration affect carbon nanotube cytotoxicity. *Toxicology Letters* **2007,** *168*, 121-131.

49. Chen, W.-Y.; Lan, G.-Y.; Chang, H.-T., Use of Fluorescent DNA-Templated Gold/Silver Nanoclusters for the Detection of Sulfide Ions. *Analytical Chemistry* **2011,** *83*, 9450-9455.

50. Au, L.; Lim, B.; Colletti, P.; Jun, Y.-S.; Xia, Y., Synthesis of Gold Microplates Using Bovine Serum Albumin as a Reductant and a Stabilizer. *Chemistry – An Asian Journal* **2010,** *5*, 123-129.

51. Hussain, S. M.; Warheit, D. B.; Ng, S. P.; Comfort, K. K.; Grabinski, C. M.; Braydich-Stolle, L. K., At the Crossroads of Nanotoxicology in vitro: Past Achievements and Current Challenges. *Toxicological Sciences* **2015,** *147*, 5-16.

52. Carnovale, C.; Bryant, G.; Shukla, R.; Bansal, V., Size, shape and surface chemistry of nano-gold dictate its cellular interactions, uptake and toxicity. *Progress in Materials Science* **2016,** *83*, 152-190.

53. Baek, M.; Kim, I.-S.; Yu, J.; Chung, H. E.; Choy, J.-H.; Choi, S.-J., Effect of Different Forms of Anionic Nanoclays on Cytotoxicity. *Journal of Nanoscience and Nanotechnology* **2011,** *11*, 1803-1806.

54. Kryuchkova, M.; Danilushkina, A.; Lvov, Y.; Fakhrullin, R., Evaluation of toxicity of nanoclays and graphene oxide in vivo: a Paramecium caudatum study. *Environmental Science: Nano* **2016,** *3*, 442-452.

55. Zhang, Y.; Ali, S. F.; Dervishi, E.; Xu, Y.; Li, Z.; Casciano, D.; Biris, A. S., Cytotoxicity Effects of Graphene and Single-Wall Carbon Nanotubes in Neural Phaeochromocytoma-Derived PC12 Cells. *ACS Nano* **2010,** *4*, 3181-3186.

56. Duch, M. C.; Budinger, G. R. S.; Liang, Y. T.; Soberanes, S.; Urich, D.; Chiarella, S. E.; Campochiaro, L. A.; Gonzalez, A.; Chandel, N. S.; Hersam, M. C.; Mutlu, G. M., Minimizing Oxidation and Stable Nanoscale Dispersion Improves the Biocompatibility of Graphene in the Lung. *Nano Letters* **2011,** *11*, 5201-5207.

57. Schinwald, A.; Murphy, F. A.; Jones, A.; MacNee, W.; Donaldson, K., Graphene-Based Nanoplatelets: A New Risk to the Respiratory System as a Consequence of Their Unusual Aerodynamic Properties. *ACS Nano* **2012,** *6*, 736-746.

58. Roberts, J. R.; Mercer, R. R.; Stefaniak, A. B.; Seehra, M. S.; Geddam, U. K.; Chaudhuri, I. S.; Kyrlidis, A.; Kodali, V. K.; Sager, T.; Kenyon, A.; Bilgesu, S. A.; Eye, T.; Scabilloni, J. F.; Leonard, S. S.; Fix, N. R.; Schwegler-Berry, D.; Farris, B. Y.; Wolfarth, M. G.; Porter, D. W.; Castranova, V.; Erdely, A., Evaluation of pulmonary and systemic toxicity following lung exposure to graphite nanoplates: a member of the graphene-based nanomaterial family. *Particle and Fibre Toxicology* **2016,** *13*, 1-22.

59. Zanni, E.; De Bellis, G.; Bracciale, M. P.; Broggi, A.; Santarelli, M. L.; Sarto, M. S.; Palleschi, C.; Uccelletti, D., Graphite Nanoplatelets and Caenorhabditis elegans: Insights from an in Vivo Model. *Nano Letters* **2012,** *12*, 2740-2744.

60. Liu, Z.; Robinson, J. T.; Sun, X.; Dai, H., PEGylated Nanographene Oxide for Delivery of Water-Insoluble Cancer Drugs. *Journal of the American Chemical Society* **2008,** *130*, 10876-10877.

61. Ali-Boucetta, H.; Bitounis, D.; Raveendran-Nair, R.; Servant, A.; Van den Bossche, J.; Kostarelos, K., Purified Graphene Oxide Dispersions Lack In Vitro Cytotoxicity and In Vivo Pathogenicity. *Advanced Healthcare Materials* **2013,** *2*, 433-441.

62. Mu, Q.; Su, G.; Li, L.; Gilbertson, B. O.; Yu, L. H.; Zhang, Q.; Sun, Y.-P.; Yan, B., Size-Dependent Cell Uptake of Protein-Coated Graphene Oxide Nanosheets. *ACS Applied Materials & Interfaces* **2012,** *4*, 2259-2266.

63. Hu, W.; Peng, C.; Luo, W.; Lv, M.; Li, X.; Li, D.; Huang, Q.; Fan, C., Graphene-Based Antibacterial Paper. *ACS Nano* **2010,** *4*, 4317-4323.

64. Singh, S. K.; Singh, M. K.; Nayak, M. K.; Kumari, S.; Shrivastava, S.; Grácio, J. J. A.; Dash, D., Thrombus Inducing Property of Atomically Thin Graphene Oxide Sheets. *ACS Nano* **2011,** *5*, 4987-4996.

65. Hecht, H. J.; Kalisz, H. M.; Hendle, J.; Schmid, R. D.; Schomburg, D., Crystal Structure of Glucose Oxidase from Aspergillus niger Refined at 2·3 Å Reslution. *Journal of Molecular Biology* **1993,** *229*, 153-172.

66. Gajhede, M.; Schuller, D. J.; Henriksen, A.; Smith, A. T.; Poulos, T. L., Crystal structure of horseradish peroxidase C at 2.15 A resolution. *Nat Struct Mol Biol* 1997, 4, 1032-1038.

67. Majorek, K. A.; Porebski, P. J.; Dayal, A.; Zimmerman, M. D.; Jablonska, K.; Stewart, A. J.; Chruszcz, M.; Minor, W., Structural and immunologic characterization of bovine, horse, and rabbit serum albumins. *Molecular Immunology* **2012,** *52*, 174-182.

68. Takano, T.; Dickerson, R. E., Redox conformation changes in refined tuna cytochrome c. *Proceedings of the National Academy of Sciences* **1980,** *77*, 6371-6375.

69. Diamond, R., Real-space refinement of the structure of hen egg-white lysozyme. *Journal of Molecular Biology* **1974,** *82*, 371-391.

70. Aranda, R.; Cai, H.; Worley, C. E.; Levin, E. J.; Li, R.; Olson, J. S.; Phillips, G. N.; Richards, M. P., Structural analysis of fish versus mammalian hemoglobins: Effect of the heme pocket environment on autooxidation and hemin loss. *Proteins: Structure, Function, and Bioinformatics* **2009,** *75*, 217-230.

71. Brownlow, S.; Cabral, J. H. M.; Cooper, R.; Flower, D. R.; Yewdall, S. J.; Polikarpov, I.; North, A. C. T.; Sawyer, L., Bovine β-lactoglobulin at 1.8 Å resolution — still an enigmatic lipocalin. *Structure* **1997,** *5*, 481-495.

72. Oohora, K.; Kihira, Y.; Mizohata, E.; Inoue, T.; Hayashi, T., C(sp3)–H Bond Hydroxylation Catalyzed by Myoglobin Reconstituted with Manganese Porphycene. *Journal of the American Chemical Society* **2013**, *135*, 17282-17285.

73. Stein, P. E.; Leslie, A. G. W.; Finch, J. T.; Carrell, R. W., Crystal structure of uncleaved ovalbumin at 1·95 Å resolution. *Journal of Molecular Biology* **1991**, *221*, 941-959.

74. Abad-Zapatero, C.; Rydel, T. J.; Erickson, J., Revised 2.3 Å structure of porcine pepsin: Evidence for a flexible subdomain. *Proteins: Structure, Function, and Bioinformatics* **1990**, *8*, 62-81.

75. Marquart, M.; Walter, J.; Deisenhofer, J.; Bode, W.; Huber, R., The geometry of the reactive site and of the peptide groups in trypsin, trypsinogen and its complexes with inhibitors. *Acta Crystallographica Section B* **1983**, *39*, 480-490.

76. Foroughi, L. M.; Kang, Y.-N.; Matzger, A. J., Polymer-Induced Heteronucleation for Protein Single Crystal Growth: Structural Elucidation of Bovine Liver Catalase and Concanavalin A Forms. *Crystal Growth & Design* **2011**, *11*, 1294-1298.

77. Wang, Z.-m.; Ho, J. X.; Ruble, J. R.; Rose, J.; Rüker, F.; Ellenburg, M.; Murphy, R.; Click, J.; Soistman, E.; Wilkerson, L.; Carter, D. C., Structural studies of several clinically important oncology drugs in complex with human serum albumin. *Biochimica et Biophysica Acta (BBA) - General Subjects* **2013**, *1830*, 5356-5374.

78. Divne, C.; Stahlberg, J.; Reinikainen, T.; Ruohonen, L.; Pettersson, G.; Knowles, J.; Teeri, T.; Jones, T., The three-dimensional crystal structure of the catalytic core of cellobiohydrolase I from Trichoderma reesei. *Science* **1994**, *265*, 524-528.

79. Fanning, S. W.; Walter, R.; Horn, J. R., Structural basis of an engineered dual-specific antibody: conformational diversity leads to a hypervariable loop metal-binding site. *Protein Engineering Design and Selection* **2014**, *27*, 391-397.

80. Clearfield, A.; Stynes, J. A., The Preparation of Crystalline Zirconium Phosphate and Some Observations on Its Ion Exchange Behaviour. *J Inorg Nucl Chem* **1964**, 26, 117-129.

81. Clearfield, A.; Smith, G. D., Crystallography and structure of α-zirconium bis(monohydrogen orthophosphate) monohydrate. *Inorg. Chem.* **1969**, 8, 431-436.

82. Bellezza, F.; Cipiciani, A.; Costantino, U.; Negozio, M. E., Zirconium Phosphate and Modified Zirconium Phosphates as Supports of Lipase. Preparation of the Composites and Activity of the Supported Enzyme. *Langmuir* 2002, 18, 8737-8742.

83. G. Alberti, M. Casciola, Layer hydrates, in: P. Colomban (Ed.), Proton Conductors, Cambridge University Press, New York, 1992, p. 238.

84. Deshapriya, I. K.; Kim, C. S.; Novak, M. J.; Kumar, C. V., Biofunctionalization of α-Zirconium Phosphate Nanosheets: Toward Rational Control of Enzyme Loading, Affinities, Activities and Structure Retention. *ACS Applied Materials & Interfaces* **2014,** *6*, 9643-9653.

85. Hummers, W. S.; Offeman, R. E., Preparation of Graphitic Oxide. *Journal of the American Chemical Society* **1958,** *80*, 1339-1339.

86. Dreyer, D. R.; Park, S.; Bielawski, C. W.; Ruoff, R. S., The chemistry of graphene oxide. *Chemical Society Reviews* **2010,** *39*, 228-240.

87. Ray, S. C., Chapter 2 - Application and Uses of Graphene Oxide and Reduced Graphene Oxide. In *Applications of Graphene and Graphene-Oxide Based Nanomaterials*, William Andrew Publishing: Oxford, 2015; pp 39-55.

88. Montes-Navajas, P.; Asenjo, N. G.; Santamaría, R.; Menéndez, R.; Corma, A.; García, H., Surface Area Measurement of Graphene Oxide in Aqueous Solutions. *Langmuir* **2013,** *29*, 13443-13448.

89. Bittolo Bon, S., and L. Valentini. "Restoring the electrical conductivity of graphene oxide films by UV light induced oxygen desorption." *arXiv preprint arXiv:1010.2108* (2010).

90. Kumar, P.; Shahzad, F.; Yu, S.; Hong, S. M.; Kim, Y.-H.; Koo, C. M., Large-area reduced graphene oxide thin film with excellent thermal conductivity and electromagnetic interference shielding effectiveness. *Carbon* **2015,** *94*, 494-500.

91. Suk, J. W.; Piner, R. D.; An, J.; Ruoff, R. S., Mechanical Properties of Monolayer Graphene Oxide. *ACS Nano* **2010,** *4*, 6557-6564.

92. Konkena, B.; Vasudevan, S., Understanding Aqueous Dispersibility of Graphene Oxide and Reduced Graphene Oxide through pKa Measurements. *The Journal of Physical Chemistry Letters* **2012,** *3*, 867-872.

93. Novoselov, K. S.; Falko, V. I.; Colombo, L.; Gellert, P. R.; Schwab, M. G.; Kim, K., A roadmap for graphene. *Nature* **2012,** *490*, 192-200.

94. McAllister, M. J.; Li, J.-L.; Adamson, D. H.; Schniepp, H. C.; Abdala, A. A.; Liu, J.; Herrera-Alonso, M.; Milius, D. L.; Car, R.; Prud'homme, R. K.; Aksay, I. A., Single Sheet Functionalized Graphene by Oxidation and Thermal Expansion of Graphite. *Chemistry of Materials* **2007,** *19*, 4396-4404.

95. Balandin, A. A., Thermal properties of graphene and nanostructured carbon materials. *Nat Mater* **2011,** *10*, 569-581.

96. Lee, J.-U.; Yoon, D.; Cheong, H., Estimation of Young's Modulus of Graphene by Raman Spectroscopy. *Nano Letters* **2012,** *12*, 4444-4448.

97. Lee, C.; Wei, X.; Kysar, J. W.; Hone, J., Measurement of the Elastic Properties and Intrinsic Strength of Monolayer Graphene. *Science* **2008,** *321*, 385-388.

2

Metal Enzyme Frameworks: Role of Metal ions in self-assembly of proteins on α-Zirconium Phosphate Nanolayers

2.1. Abstract

Previously, ion-coupled protein binding (ICPB) model was proposed to explain the thermodynamics of protein binding to negatively charged α-Zr(IV) phosphate (α-ZrP). This model is tested here using glucose oxidase (GOx) and met-hemoglobin (Hb) and with several cations (Zr(IV), Cr(III), Au(III), Al(III), Ca(II), Mg(II), Zn(II), Ni(II), Na(I), and (H(I)). The binding constant of GOx with α-ZrP was increased ~380-fold by the addition of either 1 mM Zr(IV) or 1 mM Ca(II), and affinities followed the trend Zr(IV) $\simeq$ Ca(II) > Cr(III) > Mg(II) >> H(I) > Na(I). Binding studies could not be conducted with Au(III), Al(III), Zn(II), Cu(II) and Ni(II), as these precipitated both proteins. Zr(IV) increased Hb binding constant to α-ZrP by 43-fold, and affinity enhancements followed the trend Zr(IV) > H(I) > Mg(II) > Na(I) > Ca(II) > Cr(III). Zeta potential studies clearly showed metal ion binding to α-ZrP and affinities followed the trend, Zr(IV) >> Cr(III) > Zn(II) > Ni(II) > Mg(II) > Ca(II) > Au(III) > Na(I) > H(I). Electron microscopy showed highly ordered structures of protein/metal/α-ZrP intercalates on micron length scales, and protein intercalation was also confirmed by powder XRD. Specific activities of GOx/Zr(IV)/α-ZrP and Hb/Zr(IV)/α-ZrP ternary complexes were 2.0 x 10^{-3} $M^{-1}s^{-1}$ and 6.5 x 10^{-4} $M^{-1}s^{-1}$, respectively. While activities of all GOx/cation/α-ZrP samples were comparable, those of Hb/cation/α-ZrP followed the trend Mg(II) > Na(I) > H(I) > Cr(III) > Ca(II) $\simeq$ Zr(IV). Metal ions enhanced protein

binding by orders of magnitude, as predicted by ICPB model, and binding enhancements depended on charge as well as the phosphophilicity/oxophilicity of the cation.

2.2. Introduction

Protein self-assembly at liquid-solid interfaces is of current interest and this is often achieved via chemical[1], biomolecular[2], thermal[3] or metal-induced assembly[4,5,6]. Protein self-assembly is challenging because of the large size of proteins, multiple functional groups on their surfaces, their fragility to solvents, sensitivity to particular ions and extreme pH, and their vulnerability to degradation by proteases, which are ubiquitous. Protein assemblies are increasingly being used in biosensing,[7] biomaterials,[8] biocatalysis[9] and biomedicine.[10] Therefore, it is critical to understand how such assemblies can be constructed by a systematic approach and establish the details of the mechanism of protein assembly, so that protein assembly can be controlled in a rational, predictable manner. Despite the wide spread interest in the application of proteins bound to solid surfaces, there are no quantitative models or rational approaches to address these important issues.

The mechanism of protein binding to solid surfaces is complex and not fully understood.[11] However, in the case of most water-soluble, charged proteins, protein binding requires charge neutralization at the protein-solid interface, and this electrostatic requirement imposes the participation of appropriately charged species (ions) in the protein binding mechanism. Although, there have been several qualitative studies on the promotion of binding of anionic biomolecules such as DNA to negatively charged solids such as mica,[12] or other solids,[13] there have been no quantitative studies evaluating the role of metal ions in biomolecule binding to ionic solids.

Previously, protein binding to charged solid surfaces was proposed to involve the sequestration or release of ions at/from the protein-solid interface.[14,15] That is, binding of

negatively charged proteins to a negatively charged solid would require sequestration of cations of proper charge, affinity and concentration to support protein binding.[14,15] The ion sequestration at the interface would neutralize the excess charge and facilitate protein assembly, and this ion-coupled protein binding (ICPB) model, where the metal ions played a critical role in protein binding, was also supported by pH and temperature dependence studies.[15]

Here, the ICPB model is tested explicitly, and we demonstrate metal-mediated binding of two model proteins glucose oxidase (GOx) and met-hemoglobin (Hb) to anionic α-Zirconium(IV)phosphate ($Zr(HPO_4)_2.H_2O$, abbreviated as α-ZrP.[16,17] α-ZrP consists of chemically and topologically homogeneous nanosheets, with large surface area per unit mass and high charge density. The stacks of α-ZrP nanosheets are exfoliated with tetrabutyl ammonium chloride[18] to bind metal ions, small molecules, metal complexes and proteins, regardless of their size.[11,19,20] Protein/α-ZrP assemblies, for example, indicated better thermal stability of the intercalated proteins, and the structure as well as the biological activities of the intercalated proteins have been retained to a significant extent.[13] However, one issue with α-ZrP is that its affinity for negatively charged proteins is often quite low due to unfavorable charge-charge interactions with the solid.[10] Consistent with this evaluation, we previously noted that conversion of the anionic proteins to the corresponding cationic-derivatives, via chemical modification of the surface carboxyl groups to the corresponding amide derivatives, enhanced protein binding affinities to α-ZrP.[21]

According to the ICPB model, high affinity binding of anionic proteins to anionic α-ZrP requires sequestration of appropriate cations at the protein-solid interface to neutralize the excess negative charge. Therefore, we examined the binding of GOx (isoelectric point, pI, of 4.0.[22]) and Hb (pI=6.7) to α-ZrP nanodiscs the role of a few metal ions, Zr(IV), Au(III), Cr(III),

Mg(II), Zn(II), Ni(II), Ca(II), Na(I) and H(I) in the binding mechanism. GOx is chosen for its importance as a biocatalyst and it catalyzes the conversion of β-D-glucose to δ-gluconolactone while reducing ambient O_2 to H_2O_2 [23,24,25] Hb does not function as an enzyme in nature, but its role as a peroxidase is well known.[26] Both GOx and Hb are negatively charged at neutral pH,[27] and their binding to α-ZrP should be influenced by metal ions. The selection of the cations for the current studies depended on several factors. We chose pH 3 for these studies, since 1 mM Zr(IV) (pH 3) indicated the highest increases of protein binding to α-ZrP. Au(III), Cr(III), Al(III), Zn(II), Ni(II) and Cu(II) precipitated these two proteins even at pH 3, while many others were not soluble in water at pH 3. Systematic variation of charge, size and chemical nature of the metal ions provided valuable insight into the role of these ions in the binding mechanism.

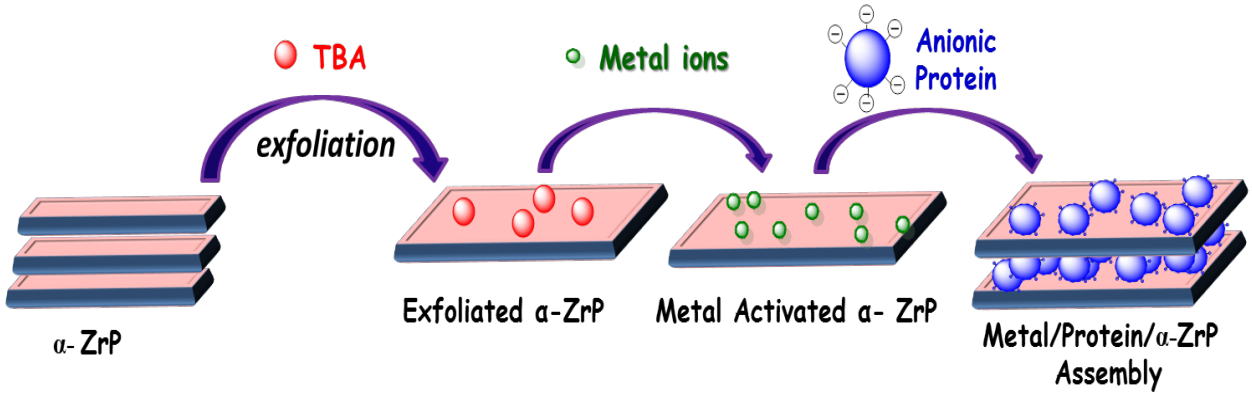

Scheme 2.1. Cation-induced binding of anionic proteins to α-ZrP nanosheets.

Zr(IV) is strongly oxophilic, thus coordinates readily with the carboxyl groups of aspartate and glutamate residues of proteins.[28] It binds to the iron-transporter protein[29], β-casein,[30] the phosphate groups of α-ZrP,[31] and thereby it could potentially function as a metal glue between the anionic proteins and the anionic α-ZrP (**Scheme 2.1**). Zr(IV)-activated phosphate/phosphonate surfaces were used to study biomolecular interactions[32] where the metal mediated the binding.[33] Tetravalent Zr(IV) was expected to have greater binding affinity when compared to trivalent or lower valent metal ions. Many trivalent metal ions could not be used for the current studies, as these tended to precipitate both proteins even at 1 mM metal concentration and pH 3. Ca(II) is known to have a higher sorption to α-ZrP over other divalent metal ions[34] and Ca(II) was expected to bind to the COOH groups of anionic proteins with moderate to high affinities.[35] Mg(II) also coordinates to certain amino acids and phosphate groups on proteins, even though much more weakly than Ca(II) or Zr(IV).[36]

Many divalent and monovalent metal ions have poor coordination abilities for monovalent ligands, but they have better affinities for poly acids and polyamines due to the chelate effect.[37] Generally, protein surfaces have numerous carboxyl and amino groups, which are appropriate for the coordination of metal ions. Na(I) and H(I) are selected as the monovalent ions for our studies, and H(I) is required to adjust the pH to 3 to solubilize the above metal salts. Na(I) is commonly used in many buffers and served as a good control to compare with H(I). Zr(IV), Cr(III), Ca(II), Mg(II), H(I) and Na(I) provided a simple series to test the role of metal ions on protein binding to α-ZrP. It is not obvious how the charge or the coordination abilities of metal ions promote or even inhibit protein binding, and it is not clear how metal-mediation would depend on the nature of the protein. For example, metal ions can enhance binding due to

neutralization of α-ZrP negative charge, or they could inhibit binding due to increased ionic strength or by competing for the phosphate groups of α-ZrP. Therefore, it is not obvious how these opposing contributions depend on the nature metal ions, metal concentration and nature of the protein. Here, we clearly establish a method to enhance protein binding using metal ions and clearly demonstrate that the nature of the metal ion (oxophilicity and phosphophilicitiy) plays an important role in protein binding. The metal behavior did not depend solely on its charge, size or coordination behavior, and could not be predicted *a priori*. Conceptually, both oxophilicity as well as the phosphophilicty of the metal ion determine its ability to promote protein binding. Thus, current studies are justified to evaluate these important aspects.

Our data show that metal ions play a major role in protein binding to α-ZrP, in support of ICPB mechanism. Zr(IV) turned out to be the best metal glue for both proteins, while Ca(II) promoted the binding of GOx much better than that of Hb. Thus, binding enhancement depended on both the metal ion as well as the isoelectric point of the protein.

2.3. Materials & Methods

2.3.1. Materials. Glucose oxidase (GOx, *Aspergillus niger, 90%*) and peroxidase type 1 from horseradish (HRP; specific activity of 356 U/mg) purchased from Calzyme laboratories Inc. (San Luis Obispo, CA) was used without further purification. Bovine met-hemoglobin (Hb), glucose, guaiacol, $ZrOCl_2$ and all metal chlorides were purchased from Sigma-Aldrich Co (St. Louis, MO). Carbon coated TEM grids were purchased from Ted Pella Inc.

2.3.2. Synthesis of α-ZrP. Synthesis and characterization of α-ZrP were performed according to the previously reported method.[16,10] In brief, α-ZrP was prepared by mixing $Zr(IV)OCl_2$ solution with phosphoric acid (9 M) followed by heating at 70 ˚C for 24 h. The resulting white crystalline solid was filtered, washed with acetone and dried. X-ray powder diffraction data showed crystalline material with layer spacing of 7.6 Å.

2.3.3. Exfoliation and Enzyme intercalation. Stacks of α-ZrP plates were exfoliated using tetrabutyl ammonium (TBA)[38] and the nanodiscs were exposed to desired enzyme-metal solutions at pH 3, which ultimately resulted in the formation of enzyme/metal/α-ZrP intercalates. The layer spacing increased when enzymes were intercalated in α-ZrP, as monitored by powder X-ray diffraction. The layer spacing increased from 7.6 Å for α-ZrP to 16 Å for TBA/α-ZrP and these further increased to ~60 Å when GOx or Hb are bound to the solid in the presence of 1 mM Zr(IV). In the case of Hb, we observed the second order diffraction peak at 31 Å, and this value is consistent with the layer spacing reported earlier for Hb/α-ZrP of 64 Å.

2.3.4. Binding studies. Protein binding to exfoliated α-ZrP nanodiscs was determined in the absence or the presence of specific metal ions at constant concentration of metal ion (1 mM) and α-ZrP (3 mM), but at increasing concentrations of the protein. The concentration of metal-

ion, was chosen such that there is substantial binding of the protein to the solid but the protein remained in solution. In other words, the metal did not precipitate the protein, under our experimental conditions.

Since the pH of $ZrOCl_2$ (1 mM) solution was 3, we chose this pH in control studies (H(I)) to account for the pH effect (pH adjusted using dilute HCl). Metal ion, protein and α-ZrP mixtures were equilibrated for 30 minutes and centrifuged at 10000 rpm for 5 minutes in a Fisher Scientific microfuge, Acspin micro 17 to separate the free enzyme from the bound. Concentration of free protein in the supernatant was determined by monitoring GOx absorbance at 280 nm using the corresponding extinction coefficients (ε = 1.336 x 10^5 $M^{-1}cm^{-1}$) or Hb absorbance at 406 nm (ε = 3.397 x 10^5 $M^{-1}cm^{-1}$). Binding isotherms were constructed from these data and analyzed using Scatchard equation (1).[39] In equation 1, K_b, n, r, c_f are the binding constant, the number of binding sites, binding density (ratio of the concentration of the bound enzyme to the concentration of α-ZrP) and concentration of free enzyme, respectively. Scatchard model is designed to quantify the interaction of an identical set of ligands to non-interacting, identical, non-overlapping binding sites on a protein. This single-set of identical binding sites model is often used as a simplistic model to examine the binding of proteins to solid surfaces, and any deviations from the model is indicated by poor fits of the data to equation 1. Best fits to the data by non-linear least squares analysis resulted in the corresponding binding parameters. All conditions for the binding studies with specific metal ions are collected in **Table 2.1.**

$$r/c_f = k_b (n-r) \text{ ----------(1)}$$

2.3.5. Zeta Potential studies. Laser Doppler Velocimetry was used to measure the zeta potentials on a Brookhaven Zeta Plus zeta potential analyzer. Sample suspensions (1.5 ml, 3 mM α-ZrP) in deionized water are prepared and pH adjusted to 3.0 using dilute HCl. The sample was transferred to a 4 mL polystyrene cuvette (Fisher Scientific). The zeta potential values were obtained by the Smoluchowski fit by software supplied by the manufacturer and zeta potentials were calculated from the corresponding electrophoretic mobilities of the samples. Samples were equilibrated with the appropriate amounts of the metal salt, protein and exfoliated α-ZrP for 30 minutes at 25° C, prior to the measurements.

2.3.6. Activity studies. Activities were measured by suitable modification of published protocols, and activities of the ternary complexes have been compared with those of the corresponding binary complexes as well as untreated enzymes, under similar conditions of buffer, temperature, pH and ionic strength. The enzyme/metal/α-ZrP complexes were re-suspended in 10 mM Tris HCl buffer pH 7.0 for activity studies at 25 °C. In a typical GOx assay,[40] 2-methoxyphenol (10 mM) HRP (2 μM) glucose (0,2 mM) and GOx (1 μM) were used. The hydrogen peroxide generated by the reduction of oxygen, coupled with the oxidation of glucose, reacts with 2-methoxyphenol, catalyzed by HRP, to produce a colored product, which has an absorption maximum at 470 nm. Kinetic data were plotted using Kaleida Graph (version 3.0), and the initial data points (0-15 s) were used to calculate the initial velocities and specific activities.

In a typical Hb assay, 2-methoxyphenol (2.5 mM in 10 mM Tris HCl buffer at pH 7.0) and H_2O_2 (1.0 mM in DI) were added to Hb (1 μM in 10 mM Tris HCl buffer at pH 7) and product formation has been monitored, at 470 nm, as a function of time.[41] The initial velocities and the specific activities were calculated from the kinetic curves, as described above.

2.3.7. Transmission electron microscopy and XRD studies. A carbon-coated Cu grid (400-mesh) was treated with plasma (Harrick PDC-32G) and coated with 1 mg/mL BSA solution. Aliquots of 3 μL of 0.5 mM α-ZrP were incubated on the grid for 1 h to allow particle adhesion. The grids were dried for 1 h and then moved directly to the microscope for imaging. For the imaging of enzyme/metal/α-ZrP complexes, 3 μL of mixture was applied where the protein concentration was 0.2 mg/mL and metal was 10 μM. All the imaging has been done with FEI Tecnai™ Spirit TEM with an operating voltage of 80 kV. The micrographs were recorded in a 4 Mega Pixel AMT camera and presented as they are. The size bars for representative structures were drawn for clarity.

Suspensions of Protein/Zr(IV)/α-ZrP (2 mL) were spotted on glass slides and air-dried. XRD analysis of the samples was carried out with a Scintag Model 2000 diffractometer using nickel-filtered CuKR radiation. Scan rates for these runs were 2°/min. The interlayer distances were measured from the 00l reflections ((l) 1, 2, etc.,) using Bragg's law.

2.3.8. Circular dichroism (CD) studies. The CD spectra were recorded on a Jasco J-710 CD spectrometer using 1 μM GOx or 2 μM Hb, 0.05 or 0.1 cm path length quartz cuvette from 260-190 nm, and 1 cm cuvette has been used for recording the Soret CD spectra from 380-450 nm. Other operating parameters were: sensitivity 20 mdeg, bandwidth 1.0 nm, response time 4 sec, resolution 0.5 nm, speed 50 nm/min and average of 3 scans. The CD spectra were corrected by subtracting the buffer signal, and data have been normalized as ellipticity per micromolar enzyme per unit path length.

2.4. Results

In simple terms, the assembly of negatively charged proteins on a negatively charged solid is feasible when excess negative charge at the protein-solid junction is neutralized by the sequestration of appropriate metal ions (**Scheme 2.1**). Explicit binding studies are carried out here to test this mechanistic model, using particular metal ions. Among the cations used here, Zr(IV) is the most acidic, 1 mM solution in water had pH 3, and hence, binding studies with all other metal ions were carried out at pH 3. Details of our studies are enumerated below.

2.4.1. Effect of Zr(IV) on protein binding. The stacks of α-ZrP were exfoliated by exposure to stoichiometric amounts of tetrabutyl ammonium hydroxide (TBA) and exposed to appropriate enzyme/metal ion mixtures (**Scheme 2.1**). The metal ion concentrations and protein concentrations were chosen such that the proteins did not precipitate in the presence of the added metal ion. At each metal ion concentration, bound protein concentration has been determined in centrifugation studies (**Figure 2.1**).

GOx did not bind to α-ZrP substantially, in the absence of Zr(IV), and binding increased from ~ 5% to ~90% at 0-1.0 mM [Zr(IV)] (**Figure 2.1.A**). Further addition of the metal had no effect on binding, and after centrifugation of the samples, the GOx/Zr(IV)/α-ZrP appeared as yellow precipitates (inset in **Figure 2.1.A**). In the absence of α-ZrP, the metal did not precipitate the protein, under any of these conditions.

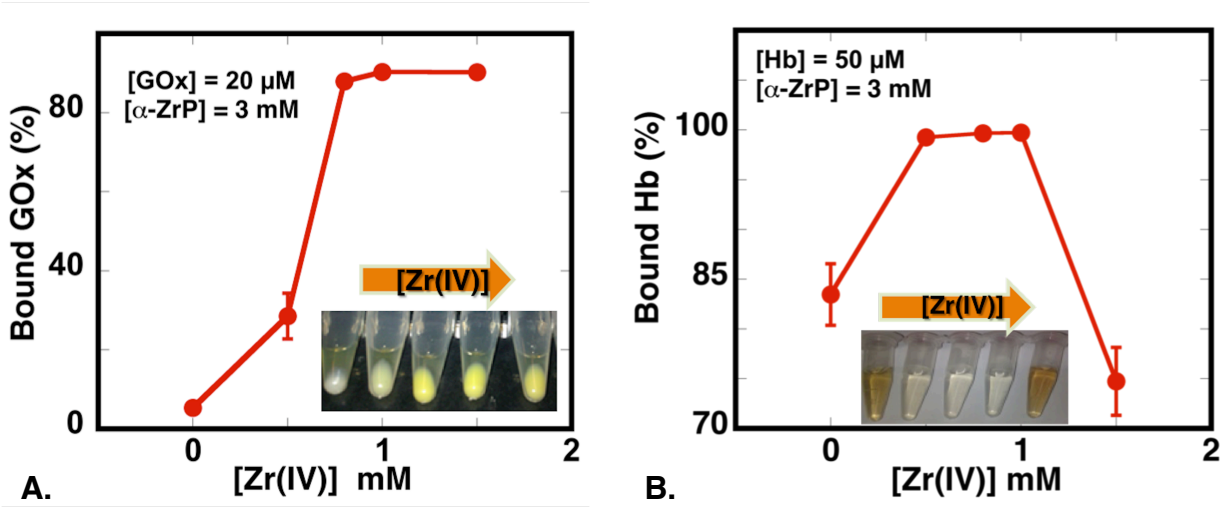

Figure 2.1 (A) Binding of GOx (20 µM) and Hb (50 μM) to α-ZrP (3 mM) as a function of the added Zr(IV) ion concentration (0 to 1.5 mM) in DI water, at room temperature. The color of α-ZrP changed from white to light yellow due to the binding of GOx, after centrifugation, as indicated in the inset photograph. (B) Enhanced binding of Hb to α-ZrP by Zr(IV) and binding inhibition at higher concentrations. The color change of the supernatant accompanying Hb binding is shown in the inset picture. Error bars on some points are too small to be visible.

Encouraged by the above findings, we tested if this strategy would also enhance the binding of moderately negatively charged Hb (pI 6.7). Hb (80 μM) binding to α-ZrP (3 mM) increased from ~85 to 100% by the addition of Zr(IV) (0-0.5 mM) and reached a plateau (1 mM Zr(IV)) and further addition (> 1 mM) inhibited Hb binding altogether (**Figure 2.1.B**). Under these conditions, Zr(IV) did not precipitate Hb, and binding inhibition above 1m M Zr(IV) is not due to Hb precipitation. Zr(IV) may compete and displace Hb from the surface. The colors of the supernatants of Hb/Zr(IV)/α-ZrP mixtures after centrifugation, as a function of increasing Zr(IV) concentration, are shown in inset in **Figure 2.1.B**. Hb binding to α-ZrP was also promoted by Zr(IV), not as dramatically as with GOx because of the high affinity of Hb in the absence of Zr(IV), and binding saturated at 100%, even at high protein concentration (80 μM) and low metal ion concentration (0.5 mM).

2.4.2. Effect of other metal ions on the binding affinities. Encouraged by the facile, Zr(IV)-mediated, binding of both GOx and Hb to α-ZrP, next we tested if this metal-promoted binding is unique to Zr(IV). The binding of GOx (20 μM) to α-ZrP (3 mM) was monitored in the presence of Cr(III), Ca(II), Mg(II), Na(I) and H(I) (1 mM cations, pH 3) and compared the data with that of Zr(IV)-mediated binding (**Figure 2.2**, right bars). Ca(II) improved GOx binding substantially (~70%), slightly less than that of Zr(IV) (80%), but much better than Cr(III) (~35%), Mg(II) improved GOx binding by ~30%, while Na(I) had essentially no measurable effect.

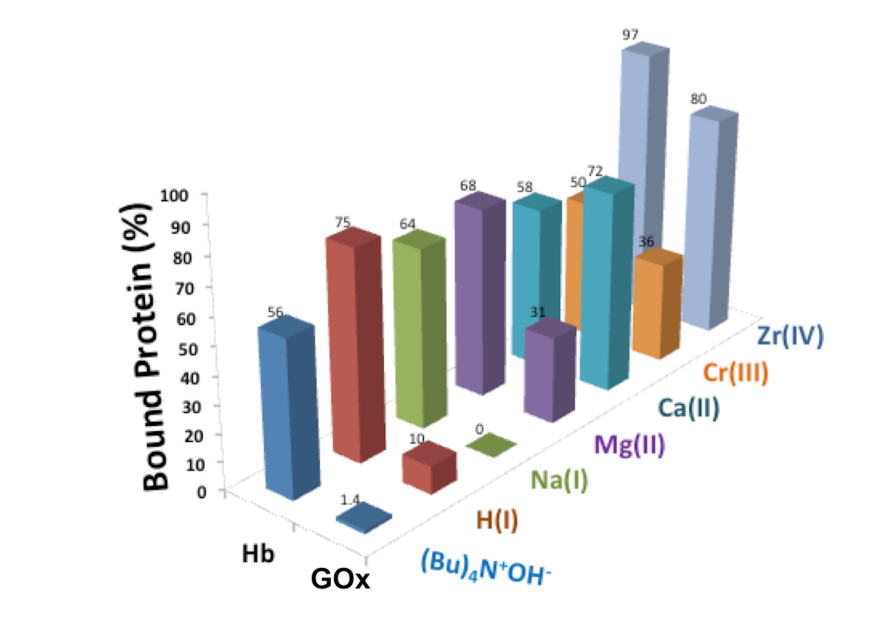

Figure 2.2. Binding of GOx (20 μM) and Hb (80 μM) to α-ZrP (3 mM) as a function of specific metal ions (1 mM, pH 3), as marked. Data in the absence of added metal ion were obtained at pH 7, and Cr(III) data are corrected for a small amount of protein precipitation by the metal ion.

H(I) (pH 3) improved GOx binding marginally (10%) but it was much better than that by Na(I) and highlights the weak role of pH in GOx binding to α-ZrP. The role of H(I) depends on the pKa values of the specific functional groups at the interface, protonation and deprotonation, while the role of Na(I) depends on its binding/dissociation at the interface. H(I) and Na(I), having the same charge, served to evaluate specific roles of these ions in the binding process. Au(III), Al(III), Zn(II), Cu(II) and Ni(II) precipitated the protein even at pH 3, and could not be used for binding studies. The metal-mediated GOx binding (1 mM metal ion, pH 3) followed the trend, Zr(IV) > Ca(II) >> Cr(III) > Mg(II) >> H(I) > Na(I), which indicated that the metal ion charge is not the absolute criterion to predict the ability of metal ions to promote protein binding.

Intrigued by the above unexpected trend, we examined the role of the protein by replacing strongly anionic GOx by a more moderately anionic Hb. Hb (80 μM) binding to α-ZrP (3 mM, pH 3) was also influenced by metal ions and the corresponding binding data are shown in **Figure 2.2** (left bars) for comparison with those of the corresponding GOx data.

One major difference between GOx and Hb is that Hb binds to α-ZrP with moderate affinity (56% binding, 80 μM Hb, 3 mM α-ZrP, pH 7), even in the absence of added metal ions (**Figure 2.2**). However, the binding was essentially quantitative (97%) in the presence of 1 mM Zr(IV). When compared to data in **Figure 2.1**, the Hb concentration in this experiment was increased to 80 μM, so that there will be a substantial amount of free protein available for metal-promoted binding. Zr(IV) enhanced the loading capacity of Hb to 1:38 (protein to phosphate) mole ratio or 400% w/w. Such high loadings of proteins are rare to achieve and high loadings of the biocatalyst are advantageous for catalytic applications.

The next best promoter of Hb binding among all ions tested here was H(I), and this is primarily because Hb is strongly positively charged at pH 3 (pI 7). Hb affinity improved at pH 3

(75%) when compared to binding at pH 7 (56%), while all cations, except Zr(IV), did not exceed the effect of H(I), and Hb binding followed the order Zr(IV) > H(I) > Mg(II) > Na(I) > Ca(II) > Cr(III). Thus, H(I) is more effective than the trivalent Cr(III), which suggests that charge is not the primary criterion. Ca(II), which promoted the binding of GOx strongly, had no such effect on Hb. Thus, the metal ion effect on the binding depended on the protein as well as the metal ion.

2.4.3. Effect of Protein concentration on binding. Improved binding of both GOx and Hb to α-ZrP by added metal ions prompted us to quantify the binding constants. Binding studies were carried out at constant metal (1 mM) and α–ZrP (3 mM) concentrations, while varying the protein concentration at pH 3 (**Figure 2.3**).

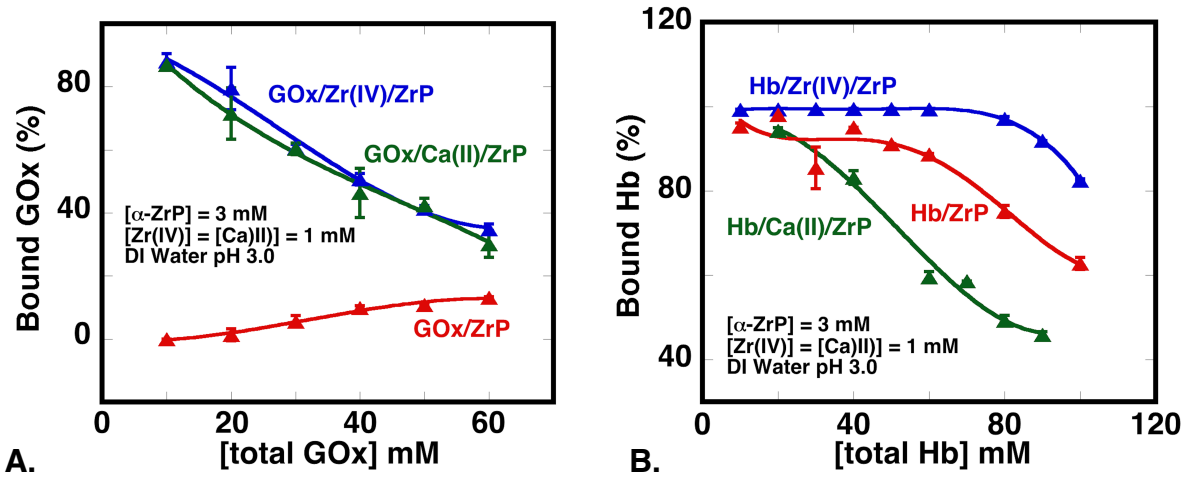

Figure 2.3. Binding isotherms of GOx (A) and Hb (B), per cent bound protein as a function of total protein concentration at a constant Zr(IV) (blue curves), Ca(II) (green curves) and H(I) (red curves) concentration (1 mM) and constant α-ZrP (3 mM) at pH 3.

In the presence of Zr(IV) and Ca(II), as observed above, GOx exhibited high per cent of binding and nearly 90% binding has been achieved at low GOx concentration (10 μM) and 1 mM Zr(IV) (**Figure 2.3.A**, blue triangles). Even at the highest GOx concentration (60 μM) 58% of GOx was still bound, or 100% w/w (GOx to α-ZrP), and the amount of bound protein increased steadily with increase in protein concentration. These data were compared with the isotherms obtained in the presence of Ca(II) (green triangles) and H(I) (blue triangles, (**Figure 2.4.A**). Isotherms for Ca(II) and Zr(IV)-mediated GOx binding are nearly the same, but these indicated higher loading than that of H(I).

The binding isotherm with Mg(II) indicated a similar effect as H(I) (**Figure 2.4.B**, black triangles), but Na(I) had essentially no effect (green triangles). Binding isotherms with Cr(III) could not be obtained because of extensive protein precipitation by Cr(III) at > 20 μM GOx.

We also quantified the binding of Hb to α-ZrP in the presence of Zr(IV) to construct the corresponding binding isotherms, and the data are shown in **Figure 2.3.B**. Nearly 100% of Hb was bound in the presence of Zr(IV) (1 mM), α-ZrP (3 mM), and this continued up until 80 μM Hb and then the percent binding began to decrease (100 μM Hb). Highest loading of Hb (80 μM Hb, 400% w/w Hb to α-ZrP) was obtained with Zr(IV), which is nearly twice as much as that of Ca(II) but better than that with H(I).

The binding isotherms of Hb depended on the type of cation used (**Figure 2.4.B**), as in the case of GOx. At low Hb concentrations, all cations promoted binding substantially (~100%), nearly equally, but the differences are clearer at higher Hb concentrations. At 80 μM Hb, for example, the order of binding was Zr(IV) > H(I) > Mg(II) > Na(I) > Ca(II), where Zr(IV) nearly doubled Hb loading on α-ZrP.

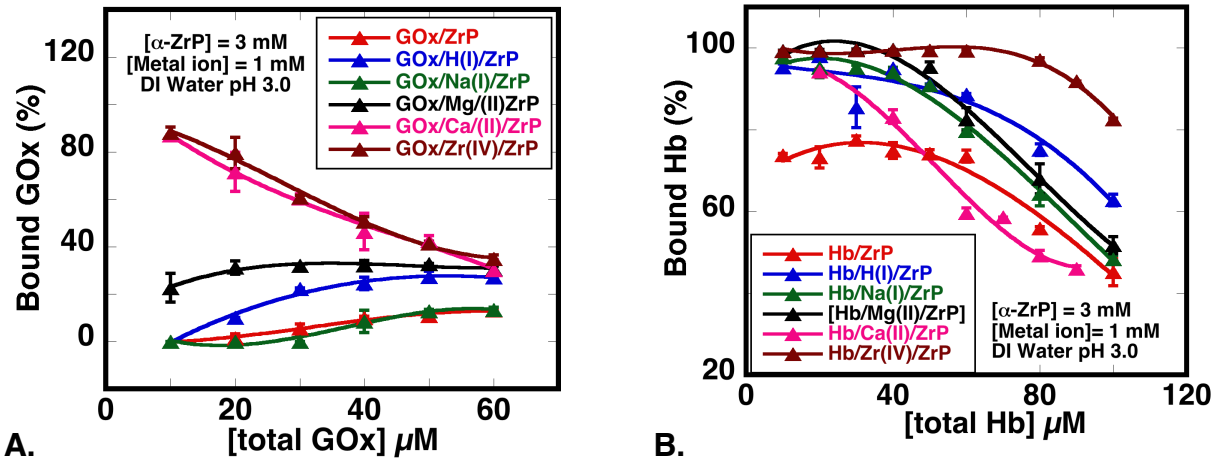

Figure 2.4. Effect of protein concentration in binding for different metal ions and pH 3. Extent of binding against protein concentration in the presence of xpecific metal ions. **A.** GOx/metal/α-ZrP data shows that Zr(IV) increased the affinity of GOx the largest, when compared to any other system. **B**. Hb/metal/α-ZrP binding data which shows that after certain concentrations lead to maximum loading. Studies done with 1 mM metal concentration in DI water. Data at pH 7 (protein/α-ZrP) were shown for comparison.

2.4.4. Binding constants. The above data was analyzed using the single, identical binding site model (Scatchard analysis), and the corresponding binding plots have been obtained for GOx and Hb with Zr(IV), Ca(II) and H(I) (**Figure 2.5**). The Scatchard plot of GOx obtained in the presence of 1 mM Zr(IV) was linear (**Figure 2.5.A**), and the best fit to equation 1 yielded a K_b of 5.4 x 10^5 M^{-1} and a binding site size of 140 phosphates per GOx. Six data points were used to calculate the binding constant and the R value is 0.95. Almost the same results were obtained for Ca(II) with a binding constant of 5.1 x 10^5 M^{-1}. In the absence of Zr(IV), the binding of GOx was too weak to obtain a good Scatchard plot, but the best estimate was 0.014x10^5 M^{-1} (pH 3). GOx binding affinity was enhanced ~380-fold by both Zr(IV) and Ca(II) (1 mM). The binding of a large ligand such as a protein with a solid surface involves, multi-point vs multi-point binding, and the Scatchard analysis is too simplistic a model. Scatchard model appears to be valid here, as indicated from the above reasonable linear fits to equation 1 in **Figure 2.5**, and validity of such analysis can be understood in terms of the assumption that the protein functions as a single binding domain and that the entire binding site on the solid functions as a single integral binding site. This simplistic treatment is not unique to the current systems and it has been widely noted ealier.[11-15]

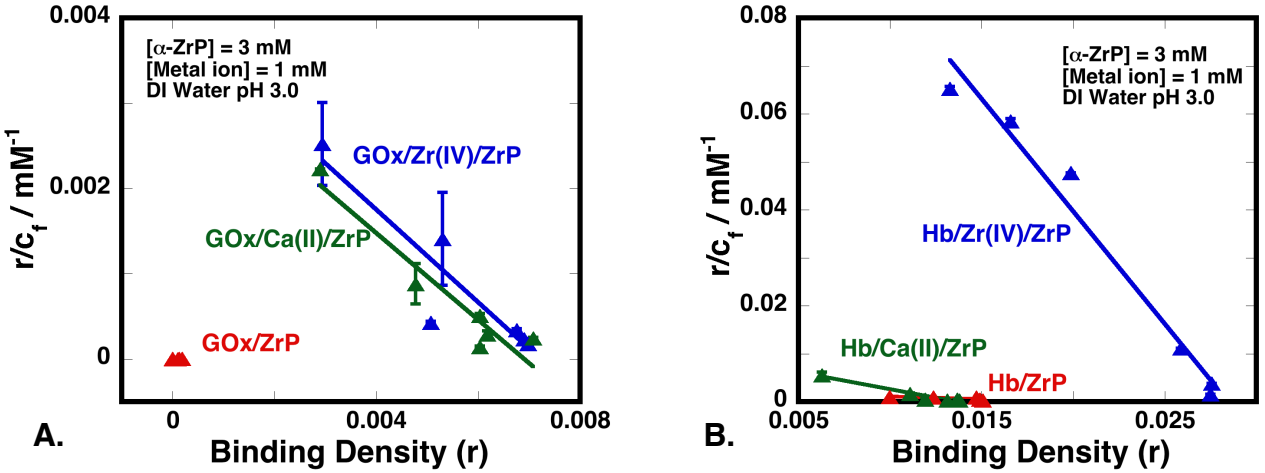

Figure 2.5. Scatchard plots in the presence of Zr(IV) (1 mM) (blue triangles), Ca(II) (green triangles) and H(I) (red triangles) for the binding of **(A)** GOx and **(B)** Hb to α-ZrP (3 mM, pH 3). The error bars on some points are too small to be visible.

In contrast to the high affinity binding of GOx, the binding constant of Hb increased only ~ 40-fold from 1.08 x 10^5 M^{-1} (H(I)) to 4.7 x 10^6 M^{-1} by Zr(IV) (**Figure 2.5.B**), and the number of phosphates occupied per Hb decreased from ~50 to ~35, thus enhancing the affinity and capacity. In case of Hb binding data, 6 data points were used to calculate the binding constants and R value was 0.88. Ca(II) did not have any effect on the binding constant of Hb, nearly the same as that with H(I) (**Figure 2.6**) The binding plots with other metal ions were also obtained (**Table 2.1**) and the binding constants varied in the order Zr(IV) >> Mg(II) > Na(I) > Ca(II) > H(I) while the binding site sizes (n) varied from 35 to 60 phosphates per Hb. The maximal loading of Hb (400%) was nearly twice as that observed with GOx (200%). 3

Table 2.1: Binding constants and number of phosphate groups coordinated per protein Values obtained from **Figure 2.6:** Some systems did not fit well and the corresponding binding constants were not estimated.

System	Binding constant K_b (10^5 /M^{-1})	Number of phosphate groups, n	Maximum Loading(w/w %) Protein to α-ZrP
GOx/Zr(IV)/ α-ZrP	5.4	140	100
GOx/Ca(II)/Z α-ZrP	5.1	145	100
GOx/ α-ZrP	0.014	412	40
Hb/Zr(IV)/ α-ZrP	46.9	35	400
Hb/Ca(II)/ α-ZrP	7.1	73	220
Hb/Mg(II)/ α-ZrP	24.5	56	250
Hb/Na(I)/ α-ZrP	11.2	60	240
Hb/ α-ZrP @pH 3	6.6	47	300
Hb/ α-ZrP	1.0	50	200

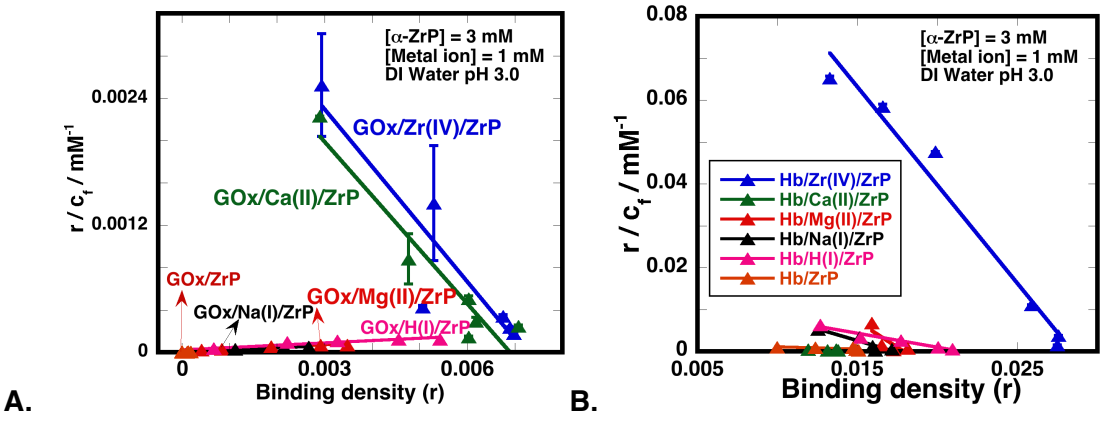

Figure 2.6: Schatchard Plots of specific enzyme/metal/α-ZrP systems. The pH was 3.0 in all cases except for the ones denoted as GOx/α-ZrP and Hb/α-ZrP (pH ~6.0). Binding constants and number of phosphate groups occupied was calculated and given in **Table 2.1.**

2.4.5. Zeta Potential Studies. The above data indicated the strong role of metal ions in protein binding to α-ZrP, and we examined metal binding to α-ZrP nanosheets by zeta potential measurements, which provides the average charge of the suspended particles. The binding of metal ions to α-ZrP nanosheets is expected to lower its negative charge, and hence, zeta potential would be a direct measure of metal binding to the phosphate groups of the α-ZrP nanosheets (phosphophilicity).

The charge of exfoliated α-ZrP (3 mM) at pH 3 was -42 ± 3 mV, for example, it linearly increased with the addition of Zr(IV), reached zero at 0.4 mM Zr(IV) and further addition increased to +45 ± 4 mV at 1 mM Zr(IV), **Figure 2.7.A**). This charge variation and charge reversal is a direct evidence of Zr(IV) binding to α-ZrP nanosheets, even at these low mM concentrations of Zr(IV). Zeta potential measurements, therefore, were used to compare the relative affinities of specific metal ions (1 mM) to α-ZrP (**Figure 2.7.B**) where some metal ions are much more effective in lowering its negative charge or imparting it a net positive charge. The net charge on α-ZrP nanosheets followed the order, Zr(IV) >> Cr(III) > Zn(II) > Ni(II) > Mg(II) > Ca(II) > Au(III) > Na(I), a direct measure of the relative phosphophilicities of these metal ions. Despite the high charge, Au(III) is a poor binder to α-ZrP, while Cr(III) is much better than all other metal ions, except Zr(IV). The divalent metal ions differed substantially, in terms of their affinities for α-ZrP and Zn(II) showed the highest affinity while Ca(II) had the lowest. Thus, metal binding to α-ZrP cannot be predicted solely based on metal ion charge.

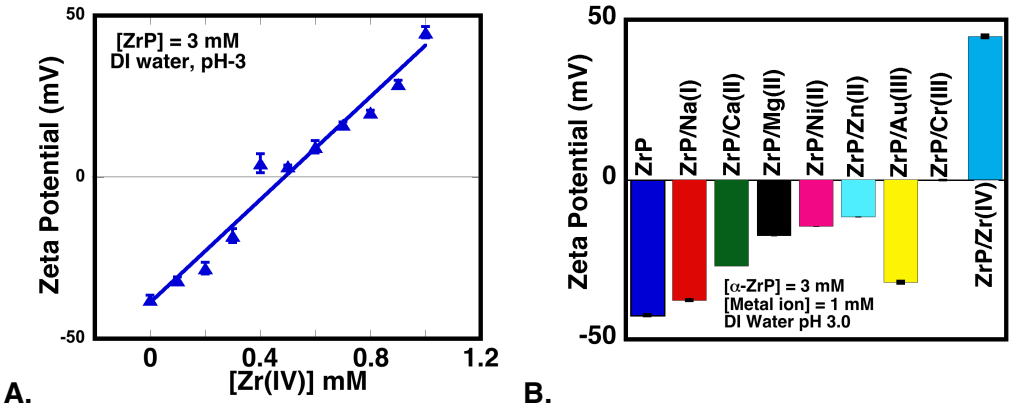

Figure 2.7. Zeta potential of exfoliated α-ZrP nanosheets **(A)** as a function of [Zr(IV)] at pH 3, and **(B)** as a function of specific metal ions (1 mM) at pH 3.0, 25˚ C.

Zeta potential measurements were also useful to follow the binding of proteins to α-ZrP (**Figure 2.8.A & B**). The gradual addition of GOx (up to 6 μM GOx) to a mixture of Zr(IV) (1 mM) and α-ZrP (3 mM, pH 3) decreased the charge from 45 ± 4 mV to +20 ± 4, and then there was no significant change with further increase in protein concentration. In the case of Hb, charge decreased almost linearly with protein concentration from + 45 ± 4 to +16.0 ± 4 mV (**Figure 2.8.B**).

The charges on specific protein/metal/α-ZrP complexes were also compared (**Figure 2.8.C**), and zeta potentials followed the order, Zr(IV)/ α-ZrP > GOx/Zr(IV)/ α-ZrP > Hb/Zr(IV)/ α-ZrP > Hb/α-ZrP > GOx/α-ZrP > α-ZrP. The metal/protein/α-ZrP complexes had a net positive charge, lower than that of Zr(IV)/ α-ZrP, which indicated charge neutralization by protein binding; while the protein/α-ZrP complexes had a net negative charge, lower than that of α-ZrP, which also indicated charge neutralization by protein binding. We observe that there was an average drop of +20 mV after protein binding to metal/α-ZrP, and an average drop of -25 mV of charge due to protein binding to α-ZrP. Both these opposing observations indicate charge reduction, which can be explained only if ions are released or absorbed during protein binding.

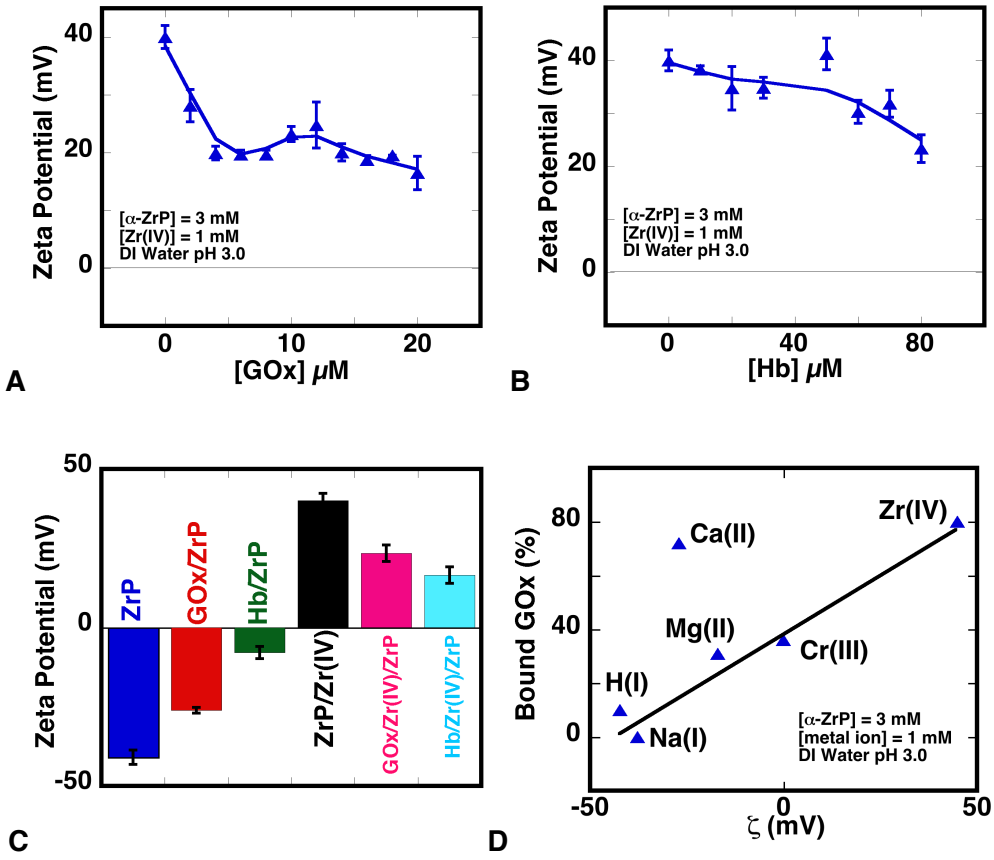

Figure 2.8. Variation of zeta potential by the addition of 2 μM increments of GOx in **(A)** and 10 μM increments of Hb **(B)** to Zr(IV) activated α-ZrP; **(C)** Zeta Potential of intercalated systems at binding saturation. α-ZrP, Zr(IV) bound to α-ZrP, GOx/Zr(IV)/ α-ZrP, GOx/α-ZrP, Hb/Zr(IV)/ α-ZrP and Hb/α-ZrP, 3 mM α-ZrP, 1 mM Zr(IV) , 20 μM GOx and 80 μM Hb were used here. All analysis has done in DI water at pH 3.0. **(D)** Efficiency of Anionic protein (GOx) binding plotted against charge on α-ZrP layers (3 mM). Surface charge of the nanolayer was modulated using different metal ions (1 mM) as noted in the plot.

2.4.6. TEM studies. Morphology studies were carried out to confirm the assembly of GOx in α-ZrP galleries in the presence of Zr(IV). The micrographs of exfoliated α-ZrP showed nanosheets of 200-300 nm in size (**Figure 2.9**) while GOx/Zr(IV)/ α-ZrP (**Figure 2.9.B**) formed elongated, uniform stacks of several micrometers in length, which is quite surprising.

Previously, powder XRD studies showed that exfoliated α-ZrP plates re-assemble back to the layered structure after enzyme binding.[19] But the neat, ordered arrangement was rarely seen in the TEMs or SEMs after protein intercalation. The formation of long strands of metal/enzyme/inorganic strands of over a micron length and about half a micron in diameter are novel features of these materials.

The powder XRD also confirmed the TBA/α-ZrP stacks (a sharp peak at 16.9 Å) (Supplementary Materials, **Figure 2.10**, as reported earlier.[19] Layered structures of protein/Zr(IV)/ α-ZrP are observed. The TEM data, combined with the powder XRD, confirm that proteins intercalate between the layers of α-ZrP, and these appear to form large self-assembled structures.

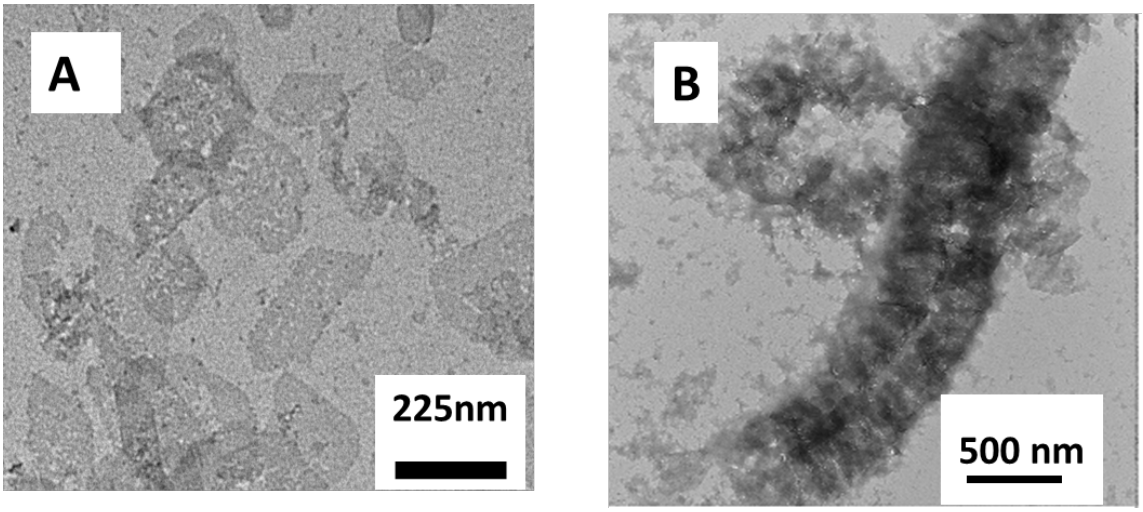

Figure 2.9. TEM images of exfoliated α-ZrP **(A)** and GOx/Zr(IV)/α-ZrP (0.2 mg/mL GOx, 0.01 mM Zr(IV), 0.5 mM α-ZrP) **(B)** indicated the layered structures of the metal enzyme assemblies in α-ZrP on a micrometer scale.

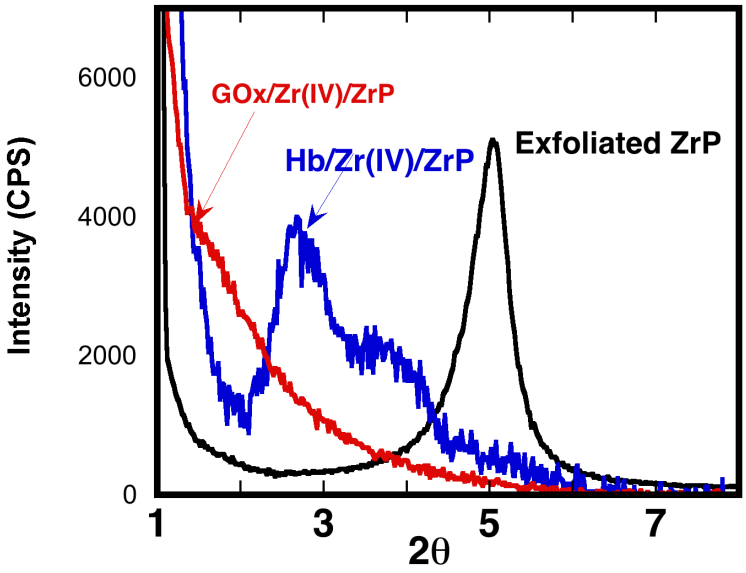

Figure 2.10. XRD of Metal/ enzyme–α-ZrP films showing the difference in spacing. Exfoliated α-ZrP showed a d value of 16 Å. Hb/Zr(IV)/ α-ZrP showed 31 Å and Go/Zr(IV)/ α-ZrP showed a broad peak around 51 Å. Hb/Zr(IV)/ α-ZrP data is multiplied by factor of 10 and normalized. Hb has average radius around 60 Å. So we assume that the diffraction is second order.

2.4.7. Enzyme structure retention and activities of the bound enzymes. One very important aspect of a biocatalyst is that it should have substantial structure retention and activity. Circular dichroism (CD) studies are used to examine the extent of retention of protein structure in the above assemblies. The far UV CD spectra of the samples are recorded in the 190-260 nm region and compared with those of free proteins Data showed that the CD spectra of GOx and Hb are distorted to some extent by the metal ions but this distortion is relieved in the case of Cr(III), on binding to α-ZrP (**Figure 2.11)**.

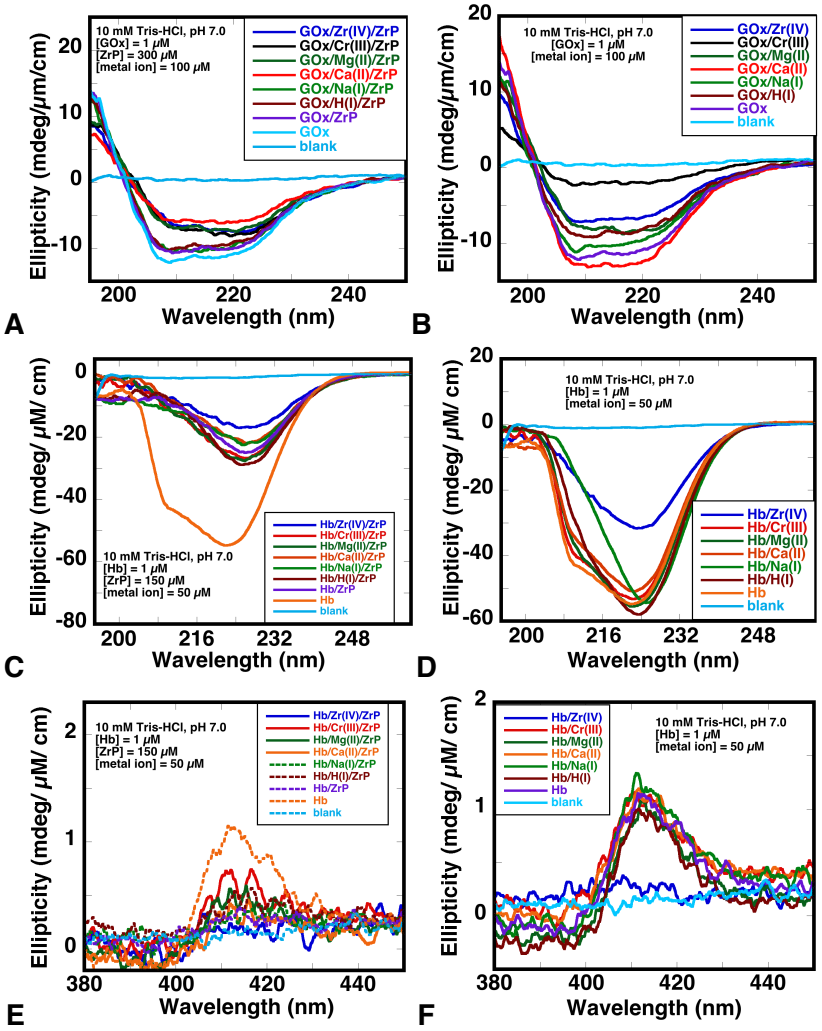

Figure 2.11. Circular dichroism spectra show that the protein secondary structure is conserved after intercalation to a significant extent. **A & C**; CD spectra of intercalated GOx and Hb respectively. We find that when the intercalation is strong the intensity got reduced. **B & D;** Data for GOx and Hb in presence of metal ions shows the effect of metal ions on protein secondary structure. **E & F**; Soret band CD spectra of Hb after intercalation and in the presence of metal ions respectively. All analysis was done in 10 mM Tris-HCl at pH 7.0 and 25^{o}C.

The loss of structure was a concern and we examined this aspect by quantitating the oxidase and peroxidase activities of the bound GOx and Hb, respectively. The GOx/metal/α-ZrP biocatalysts are suspended in phosphate buffer, and kinetic traces are followed as a function of time. The initial rates of the reaction are obtained from the slopes of the kinetic plots at early times, and the corresponding specific activities shown in **Figure 2.12**.

Specific activities of GOx and Hb samples are normalized with respect to that of free GOx and Hb as 100% respectively. The relative activities of the GOx/metal (brown bars) or GOx/metal/α-ZrP (blue bars) varied from 70-100% (**Figure 2.12**). Zr(IV), Cr(III), Mg(II) and Ca(II) did not have substantial effect on GOx activity, and all GOx/metal/solid assemblies had nearly same specific activities. The specific activity of GOx/Zr(IV)/ α-ZrP (6.1×10^{-3} M^{-1} s^{-1}) is essentially the same as GOx/H(I)/ α-ZrP (5.7×10^{-3} M^{-1} s^{-1}, under the same conditions). While metal ions have increased affinities and improved loadings, they did not adversely influence GOx activities.

Along these lines, specific activities of Hb/metal/✔-ZrP (green bars) and Hb/metal (black bars) are compared under the same conditions (**Figure 2.12**). Hb/Zr(IV)/ α-ZrP activity (3.6×10^{-4} M^{-1} s^{-1}) is slightly lower than that of Hb/H(I)/ α-ZrP (5.4×10^{-4} M^{-1} s^{-1}). Activities of Hb/metal/α-ZrP followed the order H(I) > Na(I) >Mg(II) > Cr(III) > Ca(II) $\simeq$ Zr(IV).

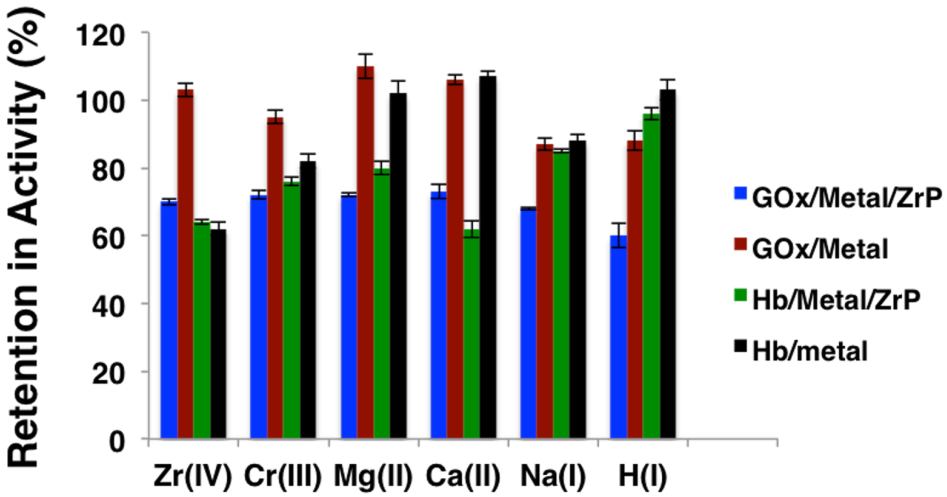

Figure 2.12. Comparison of the percent retention of enzyme activities for GOx (1 μM) bound to α-ZrP (0.2 mM), 0.1 mM metal in 10 mM Tris-HCl buffer at pH 7.0 at room temperature, and Hb (1 μM) bound to α-ZrP (0.06 mM) in 10 mM Tris-HCl buffer at pH 7.0 at room temperature. The kinetic traces of the activity assays (Absorbance v/s time) for different systems are used to determine the initial rates and specific activities.

2.5. Discussion

The role of metal ions in the binding of proteins to α-ZrP nanodiscs is tested here, and the binding resulted in protein intercalation into the galleries. The binding, morphology, structure and activities indicated that Zr(IV) and Ca(II) functioned as excellent metal glues to enhance protein binding and loading. Ca(II) increased the binding affinity of GOx but not that of Hb. These observations are consistent with the proposed ICPB mechanism for the binding of anionic proteins to anionic α-ZrP.

GOx is negatively charged at neutral pH (pI ~4),[27] and its affinity for the negatively charged α-ZrP is poor even at pH 3. According to the ICPB mechanism, sequestration of appropriate cations at the protein-solid interface facilitates binding by promoting charge neutralization at the interface. Current data show that 1 mM Zr(IV) and Ca(II) essentially increase GOx binding (20 μM GOx) to ✔-ZrP (3 mM, pH 3) from essentially zero to 90%, and enhancements depended on the protein concentration as well as the metal concentration. Increased affinity was not at the expense of activities, as indicated by the activity studies. The affinity increases depended on the type of metal ion as well as the nature of the protein. Metal ions that bind tightly to the solid as well as the protein are expected to be the best metal glues. Zeta potential studies indicated the relative affinities of the metal ions for the nanosheets followed the trend, Zr(IV) >> Cr(III) > Zn(II) > Ni(II) > Mg(II) > Ca(II) > Au(III) > Na(I) > H(I) which is related to their relative phosphohilicities. Zr(IV) is strongly oxophilic and its high affinity for the phosphate groups of α-ZrP has been already demonstrated,[28,29,30,31] and current data are consistent with these reports.

Quantitative binding of Zr(IV) to exfoliated nanosheets of α-ZrP was confirmed by the phenylphosphonic acid chelation assay. The amount of free [Zr(IV)] after equilibration with 1 mM

✔-ZrP (pH 3) was determined, after separation by centrifugation followed by chelation with phenylphosphonic acid. Zr(IV) has high formation constants with carboxylic and amine ligands,[33,42,43] and strong affinity of Zr(IV) for α-ZrP may be combined with its high affinity for the carboxylic and/or amino groups of proteins to enhance protein binding to the solid by several orders of magnitude. The high charge density, large coordination number and high phosphate affinity of Zr(IV) are responsible for its role as a metal-glue. The Zeta potential data suggest that Cr(III) is also strongly phosphophilic, next to Zr(IV), but it is surprising that Au(III) had much poorer ability to neutralize ZrP charge than anticipated.

Ca(II) was known to have a high affinity to α-ZrP over any other divalent cations,[34] but zeta potential data show that it is not as good as Zn(II), Mg(II) or Ni(II), and this deviation is due to lower pH used here (pH 3). Ca(II) also improved protein binding much better than Mg(II), and protein binding studies with Zn(II) and Ni(II) could not be carried out due to precipitation issues. Note that Ca(II) is a better binder to the COOH/NH_2 groups of proteins than Mg(II). Thus, charge is not the only criterion for predicting the binding enhancement. The ability of the metal to coordinate to the phosphate groups of the solid and/or to the carboxyl/amino groups of the proteins is also important in assessing the efficacy of a metal ion in promoting protein binding to α-ZrP.

Ca(II) promoted GOx binding to α-ZrP but not Hb, but Zr(IV) promoted binding of both proteins to α-ZrP. Thus, metal-mediated binding depended on the protein. In the case of Zr(IV), both amino and carboxylic groups are known to coordinate to the metal, and it can complex with either the COOH-rich surface of GOx or the COOH/NH_2-rich surface of Hb or to the phosphate groups of α-ZrP. Ca(II) may have higher specific affinity for GOx than Hb due to the larger number of surface COOH groups on GOx (132 per GOx dimer, 1.7 carboxylic

groups/nm^2 of protein surface) when compared to that of Hb (60 COOH groups per tetramer, 0.53 carboxylic groups/nm^2 of protein surface and 61 lysines per tetramer, 0.54 amino groups/nm^2 protein surface). The formation constants of amino or poly amino complexes of Ca(II) are small,[37] but the *log K* of poly carboxylic ligands with Ca(II) was 3-4 times higher than that with a simple acetate group.[37] So, we suspect that Ca(II) may bind better to the carboxyl-rich surfaces of GOx than amine-rich surfaces of Hb.

Mg(II) was more effective in reducing the negative charge of α-ZrP than Ca(II) (more phosphophilic) but its ability to promote GOx binding to α-ZrP was much less than that of Ca(II), and significantly less than Mg(II)-mediated binding of DNA to mica.[12] Both Mg(II) and Ca(II) complexes of phosphate and carboxylate ligands have comparable formation constants,[37] but binding of Mg(II) to proteins is weak.[44] To sum up, it is not just the charge of the cation that is important but its affinity for the functional groups decorating the protein surface as well as the phosphate groups of α-ZrP play an important role in promoting protein binding.

The average area occupied by GOx at the highest loading is 3500 Å^2 as estimated from the maximum loading of 100% (w/w). This value is comparable to the cross sectional area of GOx (diameter of ~60 Å).22 It points to a very tight packing of GOx in the galleries, and this could be one reason that the activity of GOx/Zr(IV)/ α-ZrP is lower than that of the free GOx. Strong interactions and high loading may have resulted in the formation of metal/enzyme frameworks which appeared in the TEMs to be neatly arranged. The maximal loading of Hb was much greater than GOx, 200% (w/w), and this is far greater than reported for any other protein or solid.

In general, the w/w binding capacities of a variety of solid surfaces rarely exceed 50%,[45] and one exception has been the loading of urease on a tentacle type polymer (100% w/w, enzyme to solid).[46] Compared to other supports, α-ZrP is a promising solid platform for high protein loadings, when used in conjunction with suitable metal ions. This is because of the large number of phosphate groups per unit area of α-ZrP (1 per ~25 square Å) and charge neutralization of the enzyme/solid interface may be very important requirement for high loading. Enhanced binding density is important for biocatalytic applications where maximal loading of the catalyst per unit mass of the support matrix is beneficial. In support of these inferences, α-ZrP has been reported to form multilayerd self-assembled structures.[17] Formation of long strands of GOx/Zr(IV)/ α-ZrP with near-perfect ordering of the plates is unusual and this indicates the propensity for assembly formation.

Enzyme/metal/α-ZrP materials retained significant activities, which are comparable to those of the corresponding enzyme/α-ZrP binary complexes but less than those of the free enzymes. The specific activities of GOx/Zr(IV)/ α-ZrP and Hb/Zr(IV)/ α-ZrP are 6.1 x 10^{-3} $M^{-1}s^{-1}$ and 3.6 x 10^{-4} $M^{-1}s^{-1}$, respectively, and these are comparable to those of the corresponding enzyme/α-ZrP complexes (5.2 x 10^{-3} $M^{-1}s^{-1}$ for GOx and 5.4 x 10^{-4} $M^{-1}s^{-1}$ for Hb). Zr(IV) and Cr(III) inhibited specific activities of GOx to a small extent, and this could be partly responsible for the reduction in the activities of the corresponding GOx/metal/α-ZrP materials. Activities of all GOx/metal/α-ZrP examined here are comparable to that of GOx/H(I)/ α-ZrP, while activities of Hb/metal/α-ZrP followed the trend H(I) > Na(I) > Mg(II) > Cr(III) > Ca(II) $\simeq$ Zr(IV). Higher affinities for the solid correlated with lower activities, with the exception of Hb/Na(I)/ α-ZrP. The tight packing of the proteins in the galleries, promoted by efficient charge neutralization by the added metal ions, could be one reason. Even so, the metal/enzyme/solid ternary complexes retained substantial activities, despite crowding in the galleries.

2.6. Conclusions

Metal ions, protons, counter ions, water molecules and others are to be considered in the adsorption of proteins on solid surfaces. In particular, previous studies suggested that sequestration of cations is required to neutralize excess charge that could develop at the interface when a negatively charged enzyme binds to a negatively charged solid. Sharing of ions was also suggested when anionic biomolecules such as DNA bind to anionic solids such as mica where Mg(II) played a key role in charge neutralization. The strength of interaction depended on the charge density of the biomolecule, the solid and the metal ion.[47] Here, we tested the role of specific cations in the binding of two model systems GOx and Hb. One of the most exciting observations is that the binding affinities of both proteins are increased significantly by Zr(IV), primarily due to its strong phosphophilicity for the α-ZrP surface and the carboxyl/amino surfaces of proteins. Zeta potential data show that Zr(IV) and Cr(III) are far better binders to α-ZrP than all the other metal ions tested here. Out of these two proteins, GOx is the highest negatively charged protein (charge > -80 at pH 7, pI = 4, positively charged at pH 3) which showed highest metal-enhanced binding. On the other hand, Hb showed higher binding in the absence of metal and less metal-mediated binding (pI ~ 6.7). Ca(II) promoted the binding of GOx but not Hb, because of its moderate affinity for α-ZrP but strong ability to coordinate to the carboxyl-rich GOx surface but not the amine-rich Hb surface.

The increase in the affinity cannot be attributed to simple ionic strength effects or pH changes, although these do contribute to binding enhancements. Metal ion binding to the anionic α-ZrP nanodiscs and to the enzyme surface contributes to the observed affinity increases. The ions with the highest charge, charge density, oxophilicity and phosphophilicity (Zr(IV), Ca(II), H(I)) promoted the binding the most, while no correlation was noted with ion size, hydration or charge

density. The proposition that cations may play a key role in the binding of these systems with α-ZrP is confirmed, and for a given metal, the extent of affinity increase depended directly on enzyme charge.

Consistent with this evaluation, we previously reported that when these anionic proteins are converted to the corresponding cationic derivatives by surface group modification, their binding affinities to α-ZrP was increased by orders of magnitude.[21] Thus, these two approaches are parallel, complementary and confirm the strong role of charge in the binding interactions.

High affinities are also accompanied by higher loading capacities and this aspect is promising for biocatalytic applications, and suitable cations can enhance loading as well as binding affinities without compromising activities. To the best of our knowledge, the maximum loading of 400% w/w of any protein on any solid is the highest ever reported, and nearly 400-fold increase in binding affinity of GOx is also novel. Our conclusion is that metal ions provide new avenues to enhance binding of anionic proteins to anionic solids, when there are suitable functional groups on one or both partners for anchoring the cations.

TEM images show that the structure of the solid after immobilization is also conserved, and that metal ions promote the self assembly of proteins and α-ZrP nanosheets as long strands. Proteins generally do not tend to self-assemble, unless the unfavorable protein-protein repulsions are overcome by suitable means. Metal ions of appropriate charge density and solid surfaces serve to control these interactions and form macroscopic frameworks.

In addition to the effect on the binding, the metal ions also influenced the catalytic activities of the bound enzymes. This was not anticipated. Far UV CD data showed that the CD spectra of GOx and Hb are distorted but this distortion is relieved to some extent, in the case of Cr(III), on

binding to α-ZrP (**Figure 2.11**). In the case of Zr(IV) the protein structure is distorted to a large extent but appreciable amount of activity is still retained and bound enzyme activities are comparable to those of the native enzymes. We conclude that carefully chosen cations can enhance the binding affinities of particular proteins by orders of magnitude without adversely affecting their activities, and this ability depends on their affinities for the solid as well as the proteins. These physical insights are important in the rational design of surfaces for benign, high affinity adsorption of proteins to solid surfaces.

2.7. References

1. Oohora, K.; Burazerovic, S.; Onoda, A.; Wilson, Y. M.; Ward, T. R.; Hayashi. T. Chemically Programmed Supramolecular Assembly of Hemoprotein and Streptavidin with Alternating Alignment. *Angew. Chem. Int. Ed*. **2012**, *51,* 3818 –3821.

2. Erkelenz, M.; Kuo, C. H.; Niemeyer, C. M.; DNA-Mediated Assembly of Cytochrome P450 BM3 Subdomains, *J. Am. Chem. Soc.* 2011, *133,* 16111-8.

3. Yoshimatsu, K.; Lesel, B. K.; Yonamine, Y.; Beierle, J. M.; Hoshino, Y.; Shea, K. J. Temperature-Responsive "Catch and Release" of Proteins by using Multifunctional Polymer-Based Nanoparticles. *Angew. Chem. Int. Ed*. **2012**, *51,* 2405 –2408.

4. Radford, R. J.; and Tezcan, F. A. A Superprotein Triangle Driven by Nickel(II) Coordination: Exploiting Non-Natural Metal Ligands in Protein Self-Assembly. *J. Am. Chem. Soc.* **2009**, *131*, 9136–9137.

5. Munch, H. K.; Heide, S. T.; Christensen, N. J.; Jensen, T. H.; Thulstrup, P. W.; Jensen, K. J. Controlled Self-Assembly of Re-engineered Insulin by Fe(II). *Chem. Eur. J.* **2011**, *17,* 7198 – 7204.

6. Brodin, J. D.; Ambroggio, I.; Tang, C.; Parent, K. N.; Baker, T. S.; Tezcan, F. A. Metal-directed, chemically tunable assembly of one-, two- and three-dimensional crystalline protein arrays. *Nature Chem.,* 2012, *4,* 375–382.

7. Mulchandani, A.; Rogers, K. R. *Enzyme biosensors, Part 1*, Humana Press: 1998.

8. Elnashar, M. Immobilized Molecules Using Biomaterials and Nanobiotechnology *J. Biomat. Nanobiotech.,* **2010**, *1*, 61-77.

9. Sharma, B. P.; Bailey, L. F.; Messing, R. A. Immobilized Biomaterials-Techniques and Applications. *Angew. Chem. Int. Ed.* **2003***, 21*, 837-854.

10. T. M. Chang, *Biomedical Applications of Immobilized Enzymes and Proteins*, Vol. 1, Springer: New York, **1977**.

11 . Mudhivarthi, V. K.; Bhambhani, A.; Kumar, C. V. Novel enzyme/DNA/inorganic nanomaterials: a new generation of biocatalysts. *Dalton Trans.* **2007**, 5483.

12 a. Hansma, H. G.; Laney, D. E., DNA Binding to Mica Correlates with Cationic Radius: Assay by Atomic Force Microscopy. *Biophys. J.,* **1996**, *70*, 1933-1939; b. Pastre, D.; Pie´trement, O.; Fusil, S.; Landousy, F.; Jeusset, J.; David, M. O.; Hamon, L.; Cam, E. L., and Zozime, A. Adsorption of DNA to Mica Mediated by Divalent Counter ions: A Theoretical and Experimental Study. *Biophys. J.* **2003**, *85*, 2507–2518; c. Guo, M.; Yang, W.; Coghill, L.; Campopiano, D. J.; Parkinson, J. A.; MacGillivray, R. T.; Harris, W. R.; Sadler, P. J. Synergistic anion and metal binding to the ferric ion-binding protein from Neisseria gonorrhoeae. *J. Biol. Chem.,* **2003**, *24*,

278, *2490-502*; d. Alexeev, D.; Zhu, H.;Guo, M.; Zhong, W.; Hunter, D.; Yang, W.; Campopiano, D. J.; Sadler, P., A novel protein-mineral interface, *Nature Struct. Biol.* **2003**,*10,* 297-302.

13. Kumar, C. V.; Chaudhari, A.; Proteins Immobilized at the Galleries of Layered α-Zirconium Phosphate: Structure and Activity Studies. *J. Am. Chem. Soc*. **2000**,*122*, 830-837.

14 . Duff, M. R.; Kumar, C. V. Molecular Signatures of Enzyme–Solid Interactions: Thermodynamics of Protein Binding to α-Zr(IV) Phosphate Nanoplates. *J. Phys. Chem. B*. **2009**,*113,* 15083-15089.

15. Duff, M. R.; Kumar, C. V. Protein–Solid Interactions: Important Role of Solvent, Ions, Temperature, and Buffer in Protein Binding to α-Zr(IV) Phosphate, *Langmuir* **2009**, *25*, 12635-12643.

16. Clearfield, A.; Stynes, J. A. *J.* The preparation of crystalline zirconium phosphate and some observations on its ion exchange behavior. *Inorg. Nucl. Chem*. **1964**, *26*, 117.

17 . Clearfield, A.; Smith, G. D. Crystallography and structure of alpha-zirconium bis(monohydrogen orthophosphate) monohydrate. *Inorg. Chem.* **1969**, *8,* 431-436.

18. Kaschak, D. M.; Johnson, S. A.; Hooks, D. E.; Kim,H. N.; Ward,D. M.; Mallouk, T. E. Chemistry on the Edge: A Microscopic Analysis of the Intercalation, Exfoliation, Edge Functionalization, and Monolayer Surface Tiling Reactions of α-Zirconium Phosphate. *J. Am. Chem. Soc.* **1998**, *120,* 10887-10894.

19. C. V. Kumar, A. Bhambhani, and N. Hnatiuk, *Handbook of Layered Materials*, Eds. K. Carrado, P. Dutta, and S. Auerbach, Marcel Dekker: New York (**2004**).

20. Agustin, D.; Saxena, V.; Gonza´lez, J.; David, A.; Casan,B.; Carpenter, B.; Batteas, J. D.; Colon, J. L.; Clearfield, A.; Hussain, M. D. Zirconium phosphate nano-platelets: a novel platform for drug delivery in cancer therapy. *Chem. Comm.* **2012**, *48*, 1754-1756.

21. Chowdhury, R.; Stromer, B; Pokharel, B; and Kumar, C. V., Control of Enzyme–Solid Interactions via Chemical Modification, *Langmuir* **2012**, *28,* 11881-11889.

22. Wilson, R.; Turner, A.P.F. Glucose oxidase: an ideal enzyme. *Biosensors & Bioelectronics.* **1992***, 7*, 165-185.

23. Gibson, H. Q.; Swoboda, B. E. P.; Massey, V. Kinetics and Mechanism of Action of Glucose Oxidase. *J. Biol. Chem.* **1964**, *239*, 3927.

24. Periasamy, A. P.; Chang, Y. J.; Chen, S. M. Amperometric glucose sensor based on glucose oxidase immobilized on gelatin-multiwalled carbon nanotube modified glassy carbon electrode. *Bioelectrochem.* **2011**, *80*, 114-120.

25. Katz, E.; Willner, I. A. A Biofuel Cell with Electrochemically Switchable and Tunable Power Output. *J. Am. Chem. Soc.* **2003**, *125*, 6803–6813.

26. Smith, M. J.; Beck, W. S.; Peroxidase activity of hemoglobin and its subunits: Effects thereupon of haptoglobin. *Biochim. Biophys. Acta. Protein Structure*. **1967**,*147*, 324-333.

27. Zubay, G.; *Biochemistry*, W*. C. Brown Publishing*: **1999**.

28. Grant, K. B.; Kassai, M. Major Advances in the Hydrolysis of Peptides and Proteins by Metal Ions and Complexes. *Curr. Org. Chem.* **2006***, 10*, 1035-1049.

29. Guo, M.; Yang, W.; Coghill, L.; Campopiano, D. J.; Parkinson, J. A.; MacGillivray, R. T.; Harris, W. R.; Sadler, P. J. Synergistic anion and metal binding to the ferric ion-binding protein from Neisseria gonorrhoeae. *J. Biol. Chem.,* **2003**, *24*, 278, 2490-502.

30. Hyun, P. J.; In-Ae, B.; Ho, C. S.; Preparation of Zr4+ affinity column by atom transfer radical polymerization for phosphoprotein isolation. *J. Appl. Polym. Sci.*, **2009**, *114*, 1250–1255.

31. Feng, S.; Ya, M.; Zhou, H.; Jiang, X.; Jiang, X.; Zou, H.; Cong, B. Immobilized zirconium ion affinity chromatography for specific enrichment of phosphopeptides in phosphoproteome analysis. *Mol. and Cell. Proteomics* **2007**, *6*, 1656-1666.

32. Monot, J.; Petit, M.; Lane, S. M.; Guisle, I.; Léger, J.; Tellier, C.; Talham, D. R.; and Bujoli, B. Towards Zirconium Phosphonate-Based Microarrays for Probing DNA-Protein Interactions: Critical Influence of the Location of the Probe Anchoring Groups. *J. Am. Chem. Soc*. **2008**, *130*, 6243-6251.

33. Mazur, M.; Krysin´ski, P.; Blanchard, G. J. Use of Zirconium-Phosphate-Carbonate Chemistry to Immobilize Polycyclic Aromatic Hydrocarbons on Boron-Doped Diamond. *Langmuir,* **2005**, *21,* 8802-8808.

34. Clearfield, A.; Nancollas, G. H.; Blessing, R.H.; Ion Exchange and Solvent Extraction, Marinsky, J.A. and Marcus, Y., Eds., New York: Marcel Dekker, Inc., **1973**, no. 5, pp. 11, 119

35. Toffaletti, J; Gitelman, H. J; Savory, J. Seperation and quantification of serum constituents with calcium by gel filtration. *Clin. Chem*. **1976**, *22*, 1968-1972.

36. Black, C. B.; Huang, H. W.; Cowan, J. A. Biological Coordination Chemistry of Magnesium, Sodium, and Potassium Ions. Protein and Nucleotide Binding Sites. *Coord. Chem. Rev*. **1994**, *135-136*, 165-202.

37. Daniele, P. G.; Foti, C.; Gianguzza, A.;Prenesti, E.; Sammartano, S. Weak alkali and alkaline earth metal complexes of low molecular weight ligands in aqueous solution. *Coord. Chem. Rev.*, **2008**, *252*, 1093–1107.

38. Kellwer, S. W.; Kim, H. N.; Mollouk, T. E. Layer-by-Layer Assembly of Intercalation Compounds and Heterostructures on Surfaces: Toward Molecular "Beaker" Epitaxy. *J. Am. Chem. Soc.* **1994**, *116*, 8817-8818.

39. Scatchard G. The attractions of proteins for small molecules and ions. *Annals New York Acad. Sci*. **1949**, *51*, 660-672.

40 . Bergmeyer, H. U.,Gawehn, K. and Grassl, M. (**1974**) *Methods of Enzymatic Analysis.* (Bergmeyer, H.U. ed) Volume I, Second Edition, 457-458, Academic Press, Inc., New York, NY.

41. Hsiao, H.; Uedaira. Thermal Stability of Free and Immobilized Glucose Oxidase Studied by Activity Assay and Calorimetry. *Agric. Biol. Chem.*, **1989**, *53*, 833.

42. Rothe, J.; Plaschke, M.; Denecke, M. A. Understanding Humic Acid / Zr(IV) Interaction – A Spectromicroscopy Approach. **2007**, *AIP Conf. Proc.* 882, 193-195;

43. Tshuva, E. Y.;Goldberg, I.; and Kol, M. Zirconium Complexes of Amine Bis(phenolate) Ligands as Catalysts for 1-Hexene Polymerization: Peripheral Structural Parameters Strongly Affect Reactivity. *Organometallics,* **2001**, *20,* 3017-3028.

44. Harding, M. M., The architecture of metal coordination groups in proteins. *Acta Cryst.* **2004**, *D60*, 849-859.

45. *Carrier-bound Immobilized Enzymes: Principles, Application and Design,* L. Cao, Wiley-VCH: New York (**2006**).

46. Matoba, S.; Tsuneda, S.; Saito, K.; Sugo, T. Highly Efficient Enzyme Recovery Using a Porous Membrane with Immobilized Tentacle Polymer Chains. *Nat. Biotechnol.* **1995***, 13,* 795–797.

47. Cheng, H.; Zhang, K.; Libera, J. A.; de la Cruz, M. O.; and Bedzyk, M. J. Polynucleotide Adsorption to Negatively Charged Surfaces in Divalent Salt Solutions. *Biophys. J.*, **2006**, *90*, 1164–1174.

***

3

Tuning Biological Activity of Graphene Oxide by Biophilization approaches

3.1 Abstract

Graphene oxide (GO) is being extensively investigated for enzyme and protein binding, but many enzymes bound to GO denature considerably and lose most of their activities. A simple, novel and efficient approach is described here for improving the structures and activities of enzymes bound to GO such that bound enzymes are nearly as active as those of the corresponding unbound enzymes. Our strategy is to pre-adsorb highly cationized bovine serum albumin (cBSA) to passivate GO, and cBSA/GO (bGO) served as an excellent platform for enzyme binding. The binding of met-hemoglobin, Glucose oxidase, Horseradish Peroxidase, BSA, Catalase, lysozyme and Cytochrome *c* indicated improved binding, structure retention and activities. Nearly 100% of native-like structures of all the 7 proteins/enzymes were noted at near monolayer formation of cBSA on GO (400% w/w) and all bound enzymes indicated 100% retention of their activities. A facile, benign, simple and general method has been developed for the biophilization of GO and this approach of coating with suitable protein-glues expands the utility of GO as an advanced biophilic nano material for applications in catalysis, sensing and biomedicine.

3.2. Introduction

Graphene and graphene oxide (GO) are emerging as excellent materials for practical applications due to their remarkable mechanical, electrical and optoelectronic properties.[1] A general, facile, simple approach for biophilization of GO (bGO) is reported here, and enzymes bound to bGO indicated structures/activities that are nearly the same as those of unbound enzymes. Graphene is considered as a new generation nanoelectronic material because of its high carrier mobility, room temperature quantum hall effect and others.[2] These properties ensure graphene as a promising candidate for the fabrication of advanced devices such as field effect transistors (FETs), supercapacitors, solar cells, etc.[1, 3, 4] Application of GO in biocatalysis,[5,6,7] biosensors,[8,9] bioelectronics[8] ,and biomedicine [10,11,12] is highly promising. The nanosheets of GO (surface area = 7.05 x 10^{22} $Å^2/g$)[5] are decorated with COOH, OH, epoxide groups and hydrophobic patches that enabled adsorption of biomolecules.[13, 14, 15] So far, functionalization of GO with amines,[16] proteins,[17] chemical reduction,[18] and PEGylation,[10] were used to improve the nature or affinity of GO for biomolecules.

Despite these efforts, enzyme binding to GO often results in significant loss of structure and/or function, which is not desirable. Horseradish peroxidase (HRP) and esterase bound to GO, for example, lost ~70% of their activities.[5,18] But in the case of lipase and oxalate oxidase, the activities were improved due to extensive distortion of bound protein.[18] The biomolecule-GO interactions often result in significant loss of biomolecular structure cited as a fundamental problem.[18,19] These interactions are not well-understood,[18] and reports suggest that they are primarily hydrophobic and/or electrostatic in nature.[18,19,20] Systematic manipulation of these interactions under chemical or biochemical control will be central for the rapid development of

biological applications of GO, as well as in assessing, predicting and controlling the biological toxicity of GO.

We have previously investigated the molecular details of enzyme binding to inorganic layered solids and developed specific strategies to control these interactions.[21] Highly hydrated and strongly polar or ionic surfaces provide a benign environment for favorable binding of biomolecules,[22,23] and the hydration layer on the host surface promotes the retention of bound enzyme structure and activity to a significant extent. These strategies are now being extended to control enzyme-GO interactions in a predictable manner. Our hypothesis is that the conversion of hydrophobic regions of GO into highly hydrated and hydrophilic, charged regions would support favorable interactions with biological molecules and enhance the retention of their structures and activities.

This hypothesis is tested here by adsorbing a protein glue on GO such that the glue provides a suitable, hydrated, chemically controllable surface for enzyme binding. Choice of this biophilic glue is important and while it should bind tightly to GO it also should enhance the binding of a variety of enzymes and proteins. The glue should convert the hydrophobic, unfavorable GO surface regions into a benign environment for enzyme binding. We chose chemically modified bovine serum albumin (cBSA) as an inexpensive, versatile protein-glue for these studies.

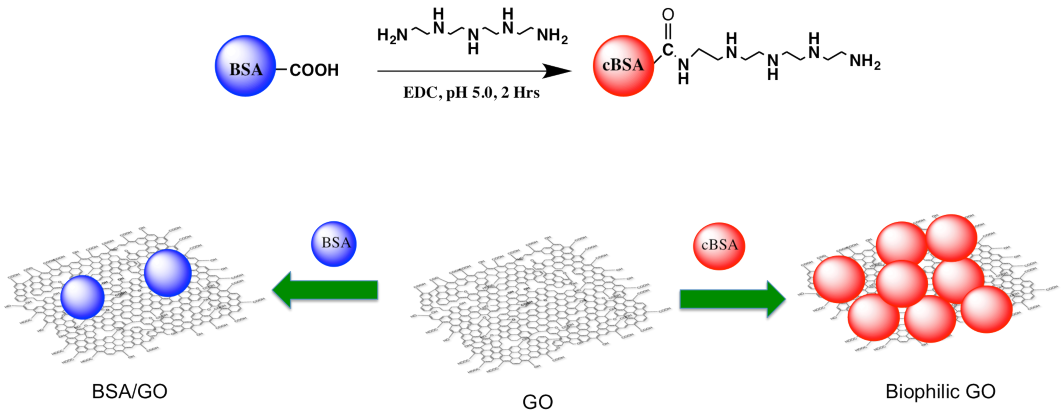

Scheme 3.1. Cationization of BSA by reacting its side chain COOH groups with tetraethylenepentamine (TEPA) via carbodiimide coupling. The resulting chemically modified BSA (cBSA) indicated 78-fold higher affinity for GO than BSA, and cBSA loaded GO (bGO) served as a benign host for enzyme binding.

Bovine serum albumin (BSA, M.wt. 64,000 Da) is an abundant, water-soluble, globular serum protein, often used to control protein adhesion to a variety of solid surfaces like glass,[24] stainless steel,[25] titanium[25] and graphene oxide.[26] We took advantage of this property of BSA to bind to variety of inorganic solids, but chemically modified its residues to control interactions with other molecules in a predictable manner. The chemistry was selected to highly cationized BSA (cBSA) such that it would bind with high affinity to negatively charged GO, on one hand, and also to enzymes and proteins, on the other hand. The high affinity binding of cBSA to negatively charged DNA (binding constant of 4.6×10^7 M^{-1}), for example, was previously demonstrated in our laboratories.[27] This combination of high affinity binding of cBSA to biomolecules and the intrinsic affinity of BSA for GO[17,26,28] suggest that cBSA might serve as an excellent protein-glue. One potential advantage with our approach is that the functionalities and charge on BSA can be tuned systematically by the modification of its side chains. For example, the COOH groups of the aspartate and glutamate side chains of BSA can be modified to the corresponding amides by carbodiimide chemistry (**Scheme 3.1**) and the net charge on the modified BSA controlled by the extent of modification. Chemical modification can potentially provide a versatile approach for the generation of protein-glues for the benign binding of a wide variety of enzymes and proteins, and it provides opportunities to fine-tune enzyme-GO interactions. Here, we show that cBSA (**Scheme 3.1**) binds avidly to GO, and the resulting cBSA-coated GO (bGO) binds met-hemoglobin (Hb), Glucose oxidase (GOx), Horseradish peroxidase (HRP), BSA, Catalase (Cat), lysozyme (Lyz) and Cytochrome *c* (Cyt *c*), which served as a representative set of proteins and enzymes. As the loading of cBSA on GO increased, the extent of bound enzyme structure retention and activities improved continuously, or exceeded those of the unbound enzymes. These data demonstrate that GO interactions with enzymes can be controlled systematically at the molecular level, for the first time, and it can be biophilized for benign adsorption of numerous enzymes and proteins.

3.3. Materials and Methods

3.3.1. Materials. Graphite flakes, Guaiacol, $KMnO_4$, Glucose oxidase (GOx, *Aspergillus niger, 90%*) and succinic anhydride were purchased from sigma Aldrich (St. Louis, MO). Peroxidase type 1 from horseradish (HRP; specific activity of 356 U/mg) and equine heart cytochrome *c* was purchased from Calzyme laboratories Inc. (San Luis Obispo, CA). Met-hemoglobin (Bovine) was obtained from MP biomedicals, LLC (Solon, OH).

3.3.2. Synthesis of Graphene Oxide. Graphene oxide was synthesized by modified Hammers method[29]. Graphite (0.5 g) was suspended in 15 mL conc. H_2SO_4 under an ice bath. 1.5 g of $KMnO_4$ added to that in portions with constant stirring. The reaction mixture was kept at 50°C and after 3 h, 35 mL distilled water was added and then stirred for 15 more minutes. Then an additional 150 mL of water were added, followed by 10 mL 30% H_2O_2 when the color changed to bright yellow and has quenched. The mixture is filtered and washed with 200 mL 10% HCl and then with water until the pH of the solution reaches 7. The oxidized graphite was sonicated for 1 h to exfoliate and centrifuged at 4000 rpm for 2 hours to remove any unexfoliated graphitic oxide. The supernatant was collected. The sonication followed by centrifugation repeated 2 more times and the stock graphene oxide solution was collected. Raman Spectroscopy XRD and AFM characterized GO. GO solution (0.7 mg/mL) in water bought in to 10 mM sodium phosphate at pH 7.0 by extensive dialysis (3 times; 4 hrs each) in an 8000 kDa semi permeable membrane. This GO solution in buffer used for 5-7 days.

3.3.3. Chemical Modification of Bovine Serum Albumin (BSA). Tetraethelenepentamine (TEPA) was dissolved in 30 mL deionized water (75 mM) and pH was adjusted to 5.0 using dil. HCl. BSA solution (0.376 mM, 10 mL) was added to the stirring TEPA solution and allowed to

equilibrate for 20 minutes. 150 mM 1-Ethyl-3-(3-dimethylaminopropyl)carbodiimide (EDC) was added to the mixture in small portions and stirred for additional 40-50 minutes. 10 mL water was added to the reaction mixture to quench the reaction. This solution was dialyzed against 10 mM Sodium Phosphate buffer at pH 7.0 to remove byproducts and excess reactants. Dialysis was done using an 8000 Da semipermeable membrane for 3 times (3 hours each). Chemical modification was confirmed by agarose gel electrophoresis and zeta potential measurement (~+4 mV; data not shown) of the modified protein. Proteins were labeled with the flurophore by mixing BSA or cBSA (40 μM; 40 mL) with 100 μL fluorescence isothocyanate (6mg/mL in DMF) for 1 hour. Unreactive FITC was removed by dialyzing (8000 Da membrane) the protein samples with 10 mM phosphate buffer at pH 7 for 3 hours.

3.3.4. cBSA binding to GO. GO and chemically modified BSA were prepared by following reported procedures[27,30] and the methods are briefly described in the supporting information (see Supporting info, methods section). Biophilic graphene oxide was prepared by controlled addition of cBSA (100 μM; 1 mL- 12 mL) to GO suspension (1 mg/mL; 25 mL) and stirred for 20 hours at room temperature in 10 mM sodium phosphate buffer at pH 7.0. The binding was monitored by zeta potential measurements and the extent of cBSA binding was tailored as needed to produce bGO samples with increasing loadings of cBSA. This protocol was followed for the preparation of bGO(-35), bGO(-22), bGO(-11) and bGO(+5) with particular concentrations of cBSA (5-65 μM).

3.3.5. Fluorescence quenching experiments. Fluorescence studies were done in a plate reader (FlexStation® 3, Molecular Devices, Sunnyvale, CA) in a standard opaque 96 well plate of 0.250 mL in volume. Fluorescence quenching of GO with FITC labeled BSA and cBSA was done. Protein samples (1 μM, 250 μL) were taken and aliquots (5-70 μL) of GO (0.7 mg/mL) were added to it and monitored FITC emission at 525 nm on excitation wavelength at 485 nm.

Inner filter effect from GO was found to be negligible throughout the measurements. The data fit into Stern-Volmer equation and plotted here. But best fit observed for modified Stern-Volmer equation,[31]

$$\frac{F_0}{F_0 - F} = \frac{1}{f_a K_a [Q]} + \frac{1}{f_a}$$ --------- (equation 3.1),

where [Q] = concentration of the quencher; F_0 = Fluorescence intensity when [Q] = 0; F = Fluorescence intensity at given [Q]; K_a = Bimolecular quenching constant, and f_a = fraction of the initial fluorescence accessible to the quencher.

3.3.6. Binding Experiments. Solutions of protein and graphene oxide (0.6 mg/mL) samples were equilibrated for around 1 hour, mixed well and centrifuged at 12,000 rpm for 10 minutes to separate the free protein from the bound. In Hb binding experiment, for example, 333 μL GO (0.6 mg/mL) and 500 μL Hb (120 μM) mixed and made up to 1 mL using 10 mM phosphate buffer at pH 7.0. Final concentration of Hb, Cyt *c* nad GOx used in each samples was 60, 60 and 5 μM respectively. The free protein concentration was calculated spectrophotometrically. The concentration of bound protein calculated from the data and plotted. A detailed binding isotherm for Cyt *c* binding to GO, bGO(-35), and bGO(+5) were carried out in 10 mM sodium phosphate buffer at pH 7.0 and compared the results. Cyt *c* was varied (0-70 μM) and same concentrations of bGOs (0.2 mg/mL) were used. The concentration of the bound protein was calculated as mentioned above. Binding constant of cBSA modification to GO was calculated using Langmuir-Freundlich (LF) equation .

$$\frac{Q}{Q_m} = \frac{K_b C^{1/n}}{1 + K_b C^{1/n}}$$ ----(equation 3.2)[32]

where Q is the amount of protein adsorbed per gram of GO, Q_m is the saturated adsorption, K is the LF binding constant, C is the equilibrium concentration of cBSA (μM) and c is the heterogeneity index.

3.3.7. Zeta Potential measurements. Zeta potential measurements were performed using laser Doppler velocimetry method in a Zeta Potential Analyzer (ZetaPLus, SR-516 type electrode, Brookhaven, Holtsville, NY). Sample suspensions were prepared in 10 mM sodium phosphate buffer at pH 7.0. GO or bGO suspensions (0.65 mg/mL) were equilibrated with protein solutions for 1 hour at room temperature prior to the measurements. Zeta potentials were measured in a 4 mL polystyrene cuvette and 3 runs were performed for each sample. Smoluchowski fit (provided by the manufacturer) for corresponding electrophoretic motilities of the samples were used to calculate zeta potential responses.

3.3.8. AFM Studies. Atomic Force Microscopy (AFM) of the samples was performed using a Bruker Dimension Icon (Santa Barbara, CA). Sample suspensions were sonicated for 20 minutes before AFM studies. The samples for AFM were prepared by the following method. First a small droplet (25 μL) of the sample suspension was put on a freshly cleaved mica sheet attached to a brass stub, left for 2h in a desiccator to remove the solvent slowly.

3.3.9. Powder X-Ray Diffraction Studies. Protein/GO suspensions with maximum loading of the protein in 0.6 mg/mL GO in 10 mM phosphate buffer at pH 7.0 were drop-casted on glass slides and air dried (3-4 days). The powder X-ray diffraction studies were performed using Rigaku Ultima IV diffractometer (Woodlands, TX) with CuKα (λ = 0.15406 nm) radiation. Beam voltage and beam current of 40 kV and 44 mA were used, respectively. A two-theta range of 0.5

– 35 º was used with a continuous scan rate of 2.0 º/min. The interlayer spacing of graphite powder, GO and GO/protein complexes were measured from the 00*l* *reflections (l*= 1, 2, 3 etc.,).

3.3.10. Circular Dichroism. The CD spectra was recorded on a Jasco J-710 CD spectrometer (Easton, MD) for proteins before and after binding with GO or bGO (0.04 mg/mL) using 0.05 cm path length quartz cuvette from 260 – 190 nm. Sensitivity of 20 mdeg, bandwidth 1.0 nm, response time 4 s, resolution 0.5 nm, speed 50 nm/min and average of 3 scans were recorded. The CD spectra was corrected by subtracting the buffer signal, and the data has been normalized as ellipticity per micro molar enzyme per unit path length. Structure retention of the conjugates was compared with that of free enzymes taking intensity at 222 nm as a standard. Signal intensity at 222 nm from cBSA was subtracted from the samples containing that in excess. The α -helicity of the proteins was using the following relationship

$$\alpha - \text{helicity} = \frac{\text{M x } \Theta_{222}}{\text{C x } N} \quad \text{--- (equation 3.3),}$$

where M is the molecular weight of the protein, θ_{222} is the ellipticity of the protein concentration C and N is the number of amino acids in the protein. Percentage α -helicity was calculated by comparing it with that of free proteins.

3.3.11. Enzyme Activity Studies. Molecular Devices flex station plate reader was used for kinetic studies. Activities were measured by suitable modification of published protocols[33, 34] and activities of the bound proteins have been compared with untreated enzymes, under similar conditions of buffer, temperature, pH and ionic strength. The GO/Enzyme and bGO/Enzyme complexes were suspended in 10 mM phosphate buffer pH 7.0. Enzyme assay vary with proteins, for example peroxidase activity of heme containing enzymes and oxidase activity of GOx were used. Kinetic data were plotted using Kaleida Graph (version 4.1.3), and the initial data points were used to calculate the initial velocities and specific activities.

3.3.12. Raman Spectroscopy. A Renishaw Smith inVia Raman/IR microprobe (Gloucestershire, UK) was used with a 633 nm wavelength for the Raman spectroscopy of GO (0.65 mg/mL), bGO(-35) and GOx/bGO(-35) suspensions, and ten scan were averaged for better signal to noise ratio.

3.4. Results

A novel biophilization approach for the high affinity, favorable, benign binding of enzymes and proteins to GO is reported here. These investigations are described below.

3.4.1. Chemical modification of BSA and its interaction with GO. Our strategy has been to find a protein 'glue' such that it binds to GO on one hand, and also binds to the enzymes of interest, on the other hand. We chose to chemically modify BSA (cBSA) to produce a number of different derivatives, and cBSA was produced by coupling the carboxylic acid groups on the glutamic and aspartic acid side chains of BSA with tetraethylenepentamine (TEPA), via the standard carbodiimide coupling chemistry (**Scheme 3.1**, top).

Production of BSA-TEPA was monitored by agarose gel electrophoresis and the charge on cBSA was determined to be +24, as estimated from the migration in the agarose gel (**Figure 3.1.A**) by comparing the migration distances of BSA and cBSA. Considering the charge on BSA to be -18[35] we estimate the charge on the cBSA to be +24. The circular dichroism (CD) spectra of cBSA indicated significant (~75%) retention of its native-like structure (**Figure 3.1.B**).

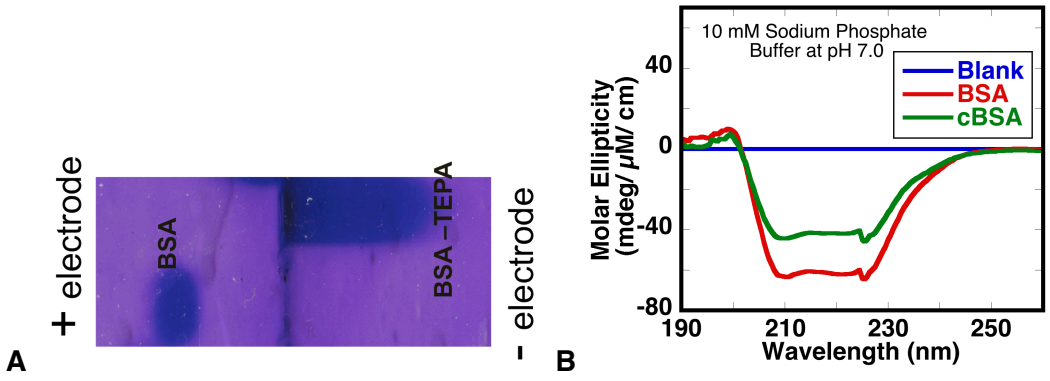

Figure 3.1. **A.** Agarose gel electrophoresis of BSA-TEPA (cBSA) (top lane), compared with native BSA (bottom) at pH 7.0. Modification of carboxylic acid side chains with TEPA flipped the charge of BSA and cBSA moved to the negative electrode, when an electric field was applied. Based on the migration distance in the electric field the average charge of cBSA found to be +24 at pH 7.0. **B)** CD spectra of cBSA (green) in comparison with BSA shows that the chemical modification has not substantially affected the secondary structure of the protein.

3.4.2. cBSA Binding studies with GO. Binding was quantified by fluorescence quenching experiments, where we exploited the fact that GO quenches the fluorescence of a number of dyes.[10, 36] For example, we labeled cBSA with fluorescein isothiocyanate (FITC), purified the cBSA-FITC conjugate by dialysis, and tested binding to GO by fluorescence spectroscopy.

The gradual addition of GO suspensions to cBSA-FITC quenched fluorescence rapidly (1 μM protein, **Figure 3.2.A and B**), and in control experiments, where BSA-FITC was used instead of cBSA-FITC under otherwise identical conditions, fluorescence was quenched very poorly (**Figure 3.2.C and D**). Thus, cBSA-FITC binds to GO with greater affinity than BSA-FITC. The quenching data were fitted to equation 3.1, and the corresponding Stern Volmer constant for association (K_a) has been found to be 228 mL/mg of GO or 1.64×10^4 M^{-1} where the molar mass of a C6 unit was used for GO concentration estimates. Similar analysis of the quenching of BSA-FITC fluorescence by GO (**Figure 3.2.D**) indicated K_a value of $2.1 \pm 0.4 \times 10^2$ M^{-1}, and by comparing the two quenching constants, cBSA-FITC appears to bind nearly 78-fold stronger than BSA-FITC.

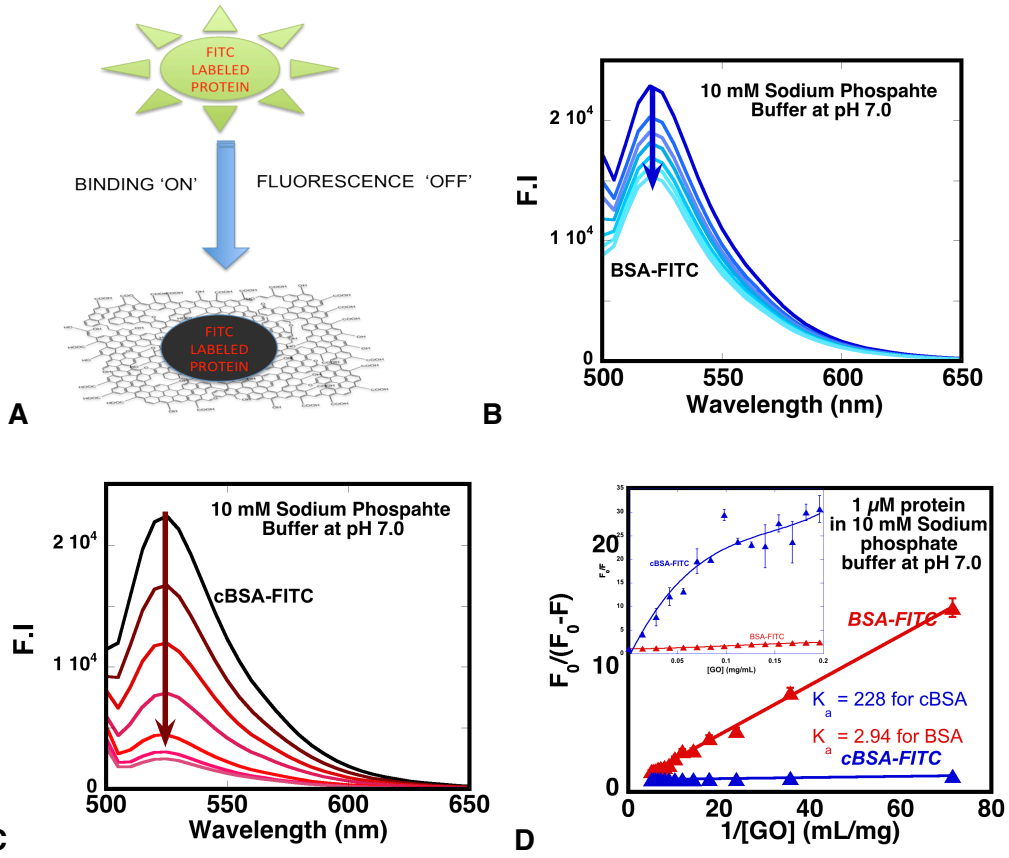

Figure 3.2. A. Quenching of cBSA-FITC fluorescence by GO. Fluorescence Spectra show the quenching of fluorescence of cBSA-FITC **(B)** and BSA-FITC **(C**) by GO. Clearly, quenching is very prominent in case of chemically modified BSA. **D**. Modified Stern-Volmer plots (equation 3.1) for the quenching of cBSA-FITC (blue lines) and BSA-FITC (red lines) by GO. The inset shows the corresponding Stern-Volmer plots.

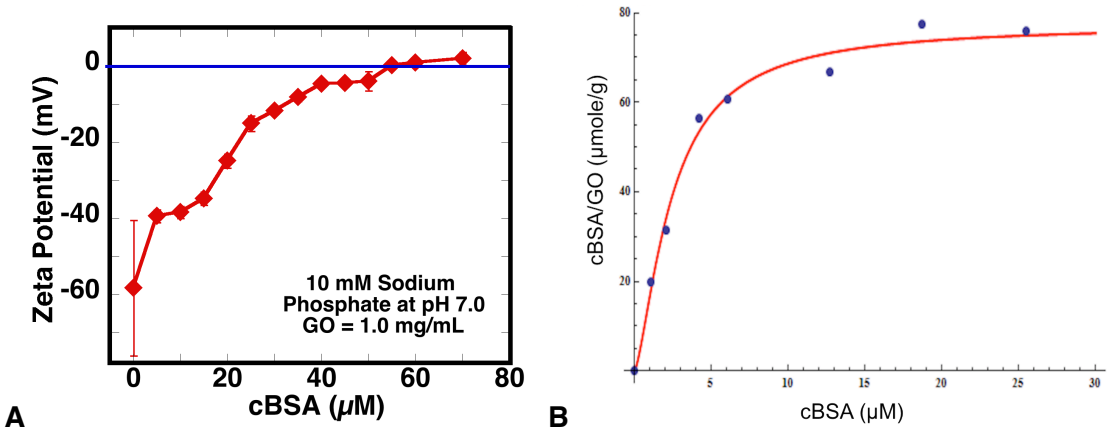

Figure 3.3. A. Zeta potential titrations of GO (1 mg/ml) with increasing concentrations of cBSA. The data points are averages of three measurements, and in some cases, the error bars are too small to be visible. **B**. Langmuir–Freundlich Isotherm of cBSA binding to GO. Binding parameters were calculated by non-linear fit (R^2=0.997) of the isotherms following equation 3.2.

The binding of cBSA (+24) to GO was also confirmed by zeta potential titrations (**Figure 3.3.A**), where aliquots of cBSA (0-65 μM) were added to GO suspensions (1 mg/ml, phosphate buffer at pH 7.0). GO charge increased progressively from -61 to +5 mV as a function of increasing concentrations of cBSA. Corresponding control experiments by replacing cBSA with BSA show only minor changes in GO charge (**Figure 3.4**).

In another set of experiments, we examined the binding directly by centrifugation studies, where mixtures of cBSA and GO were equilibrated for 30 minutes and centrifuged to separate the bound protein from the unbound. This data was then plotted to construct the corresponding binding isotherms (**Figure 3.3.B**) and analyzed using Langmuir-Freundlich (LF) isotherm (equation 3.2).[31] The analysis indicated a binding constant (K_b) of 2.73 x 10^5 M^{-1} and heterogeneity index (n) of 0.67 for cBSA, from the non-linear regression analysis of the binding isotherm (**Figure 3.3.B**). Thus, three different approaches were used to examine the binding of cBSA to GO. Encouraged by these results, we examined the binding of a small set of proteins and enzymes to cBSA/GO as a function of cBSA loading.

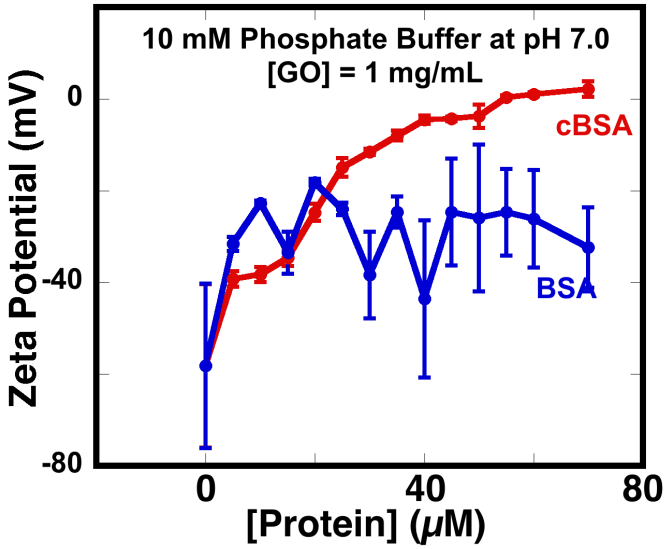

Figure 3.4. Comparison of change in zeta potential on binding BSA and cBSA to GO. Zeta potential of the system gradually changes from -60 mV to +5 mV upon addition of cBSA (red). Addition of BSA caused change in zeta potential to – 30 mV but large error in the measurement was noted that might be due to the heterogeneity of the system.

3.4.3. Biophilization of GO: We prepared GO (1 mg/mL) with increasing loadings of cBSA (0, 4, 35, 45 and 65 μM, bound per mg of GO) which resulted in discrete bGO samples, and the zeta potentials of these samples were -60, -35, -22, -11 and +5 mV, respectively. These are labeled as GO, bGO(-35), bGO(-22), bGO(-11) and bGO(+5) for future reference. Initially, the binding of Cyt *c* these bGO samples was examined systematically and then the binding of a small set of proteins and enzymes has been evaluated.

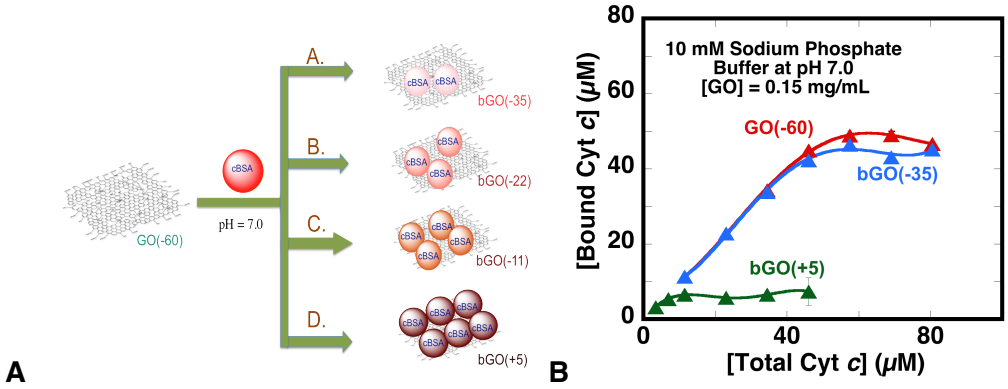

Scheme 3.2.A. Biophilization of GO with increasing loadings of cBSA (A through D, 0, 4, 35, 45 and 65 μM, bound per mg of GO) gave rise to four different bGO samples with decreasing negative charge or increasing positive charge (given in parenthesis). **B.** Binding of Cyt *c* to GO(-60) (red line), bGO-35(blue) and bGO(+5) (green) as a function of increasing concentrations of Cyt *c*.

3.4.4. Cyt *c* binding to bGO. Cyt *c* was chosen as a good model system to control its binding behavior with GO, as this protein was known to show higher electrochemical redox activity on GO.[37] The binding affinities of Cyt *c* with GO and bGO samples were determined by centrifugation studies. Mixtures of GO or bGO (0.15 mg/ml) and increasing concentrations of Cyt *c* (0-80 μM) were equilibrated for 30 minutes, followed by centrifugation to separate the bound Cyt *c* from the unbound protein. Binding isotherms were constructed from these data

(**Scheme 3.2.B**) and analyzed by the LF model ($R^2 > 0.98$) Cyt *c* had high affinity towards the negatively charged GO ($K_b = 7.0 \times 10^4\ M^{-1}$) and bGO(-35) and binding saturated at 45-50 μM Cyt *c* while its binding to bGO(+5) has been considerably poor($K_b = 3.5 \times 10^3\ M^{-1}$). Clearly, protein binding was influenced by the net charge on bGO or GO, and hence, we tested binding as a function of the isoelectric point of the protein.

3.4.5. Binding as a function of protein isoelectric point: Often it is presumed that protein binding is dominated by electrostatic interactions, and we tested this premise by examining the binding of a few proteins with GO and its derivatives. The binding of GOx, Hb and Cyt *c* (pI; 4.5, 6.8 and 10 with net charge at pH 7.0 as -65, -1, +7, respectively)[38,39,40] was examined by using GO, bGO(-35) and bGO(+5), and evaluated how the charge on the adsorbent influences protein binding (**Figure 3.5.A**). The maximal loadings of the three proteins (% w/w) were obtained by equilibration of the adsorbent with excess protein, separation of the unbound protein and quantifying the amount of protein bound to the adsorbent. The % maximal loadings were plotted (Y-axis) as a function of adsorbent charge (X-axis) as well as the pI values of the protein (Z-axis). At first glance, binding seemed to correlate with favorable electrostatic interactions but there are some interesting trends that did not obey this expectation. That is, proteins with a net positive charge should consistently show higher affinities with strongly negatively charged GO, while proteins with net negative charge are expected to show poor binding. The loadings varied from 88% to a high value of 453% (w/w). The data clearly showed that protein binding is not entirely driven by electrostatic interactions, as discussed later.

3.4.6. Zeta Potential Titrations: To gain insight into the binding mechanism, we examined the net charge on the nanosheets as the protein binding progressed by zeta potential titrations (**Figure 3.5.B**). The zeta potential of GO(-60), for example, decreased steadily as a function of

increasing concentrations of Cyt *c* (0-115 μM, red curve) and reached a plateau at -6 mV, but the binding did not reverse the net charge on the nanosheets or even completely neutralize it, despite the net positive charge on Cyt *c*. Binding of Cyt *c* to bGO(-35) followed similar trend (blue line) but binding saturated at around the same Cyt *c* concentration as with GO, and zeta potential also reached a plateau at -6 mV, the same as in the case of GO/Cyt *c*. This is surprising. On the other hand, Cyt *c* binding to bGO(+5) (green line) indicated essentially minor changes in the zeta potential, even though there has been considerable loading of Cyt *c* to these nanosheets (**Figure 3.5.A**).

Binding of GOx and Hb also affected the surface potential of GO or bGO surfaces (**Figure 3.6**) and in general, when the loading of the protein was higher, modulation of zeta potential has been higher. The binding of the proteins to these nanosheets could occur at the edges or on their surfaces, and these two binding modes can be distinguished by powder XRD and AFM studies, as described below.

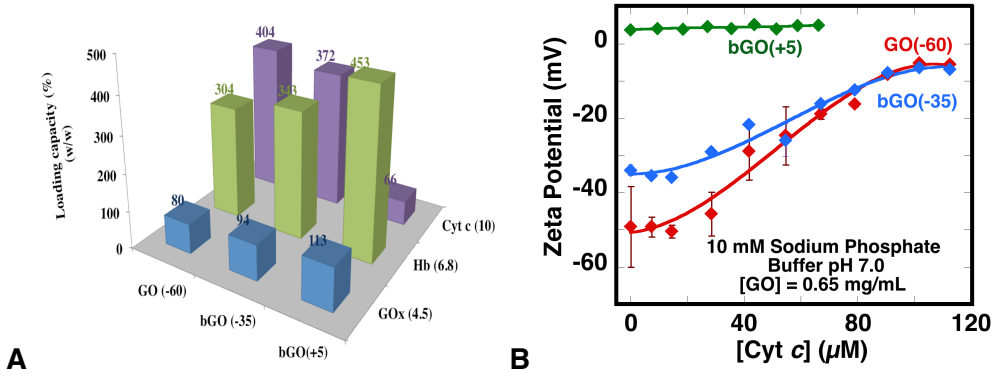

Figure 3.5. A. Maximal loadings (% w/w) of GOx, Hb and Cyt *c* to GO(-60), bGO(-35), bGO(+5), at pH 7, are shown. The data is arranged with increasing pI of the protein on X-axis and increasing charge of the adsorbent on the Z-axis. All measurements were averages of three trials and in some cases, the error bars are too small to be visible. **B.** Zeta potential as a function of Cyt *c* loading on bGO. Protein binding increased the zeta potential in all cases.

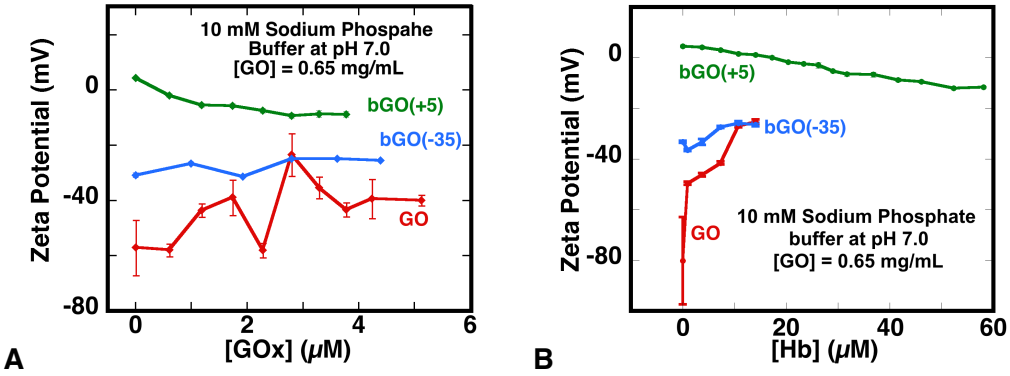

Figure 3.6. Zeta potential titration data for **(A)** GOx and **(B)** Hb, binding with different bGO samples. Change in zeta potential was proportional to extent of binding in each case. For example Hb interacts well with GO and GOx is not (red lines), therefore a shift in zeta potential is prominent in the former case than in later.

3.4.7. Powder XRD and AFM studies: Powder XRD data was collected after drop-casting a sample of the protein/bGO suspension on glass cover slips and allowing to air-dry them. Protein binding on the nanosheets should expand the interlayer distances of GO from 7.4 Å to appropriate values that correspond to the respective diameters of bGO/protein intercalation products after restacking of the protein embedded GO layers (**Figure 3.7.A**). The powder XRD diffractograms of GO and bGO(+5) showed distinct peaks at 7.4 and 51 Å, respectively, while bGO(-35) did not show any discernable peaks. Binding of GOx, Hb and Cyt c to bGO(-35) indicated clear peaks with d-spacings of 97, 58, and 37 Å, respectively (**Figure 3.7.B and C**).

Control experiments with films in the absence of bGO(-35) showed no XRD signals in the region of interest (**Figure 3.7.A**). The d-spacings of the protein/bGO(+5) samples clearly show the binding of the proteins on the basal plane of GO before they restack up on drying, but binding at the edges could not be ruled out. Therefore, AFM studies were done to examine the extent of binding on the surface vs edges of the nanosheets.

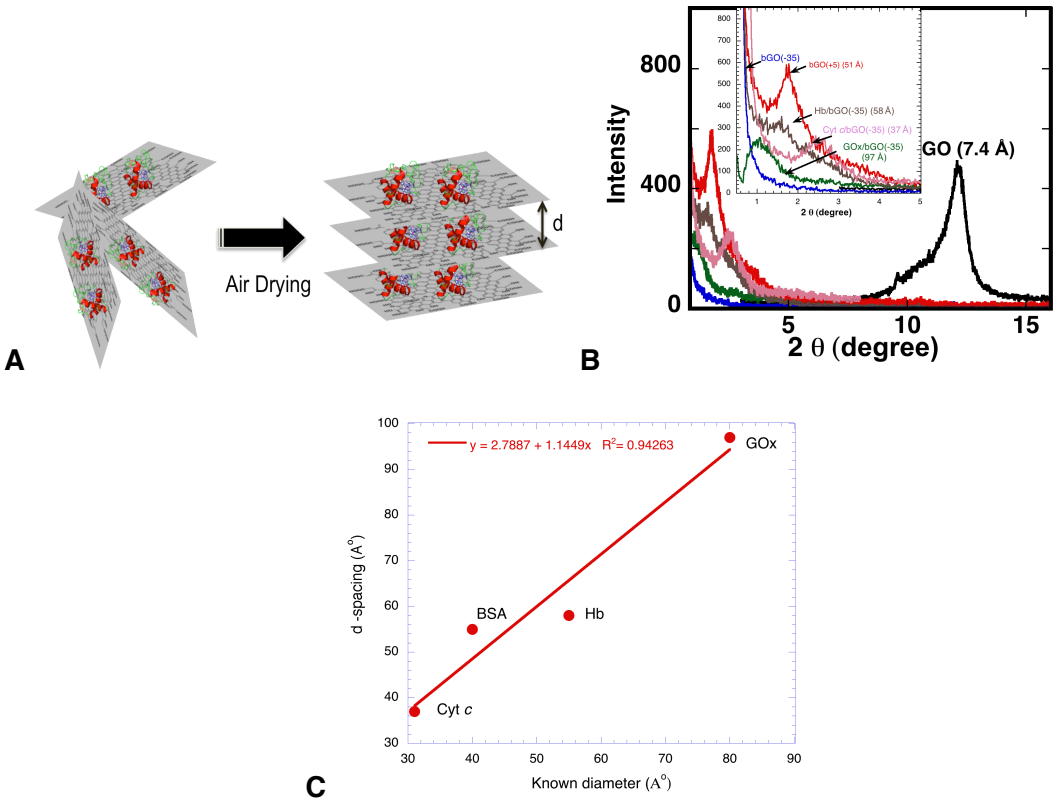

Figure 3.7. A. Protein bound, exfoliated GO sheets in solution (left), which are reassembled to a layered structure (right) upon air-drying the suspension on a glass slide. **B**. Powder XRD data of protein/bGO(-35) films are shown. **C.** The d-spacings correlated with known diameters of the corresponding proteins.

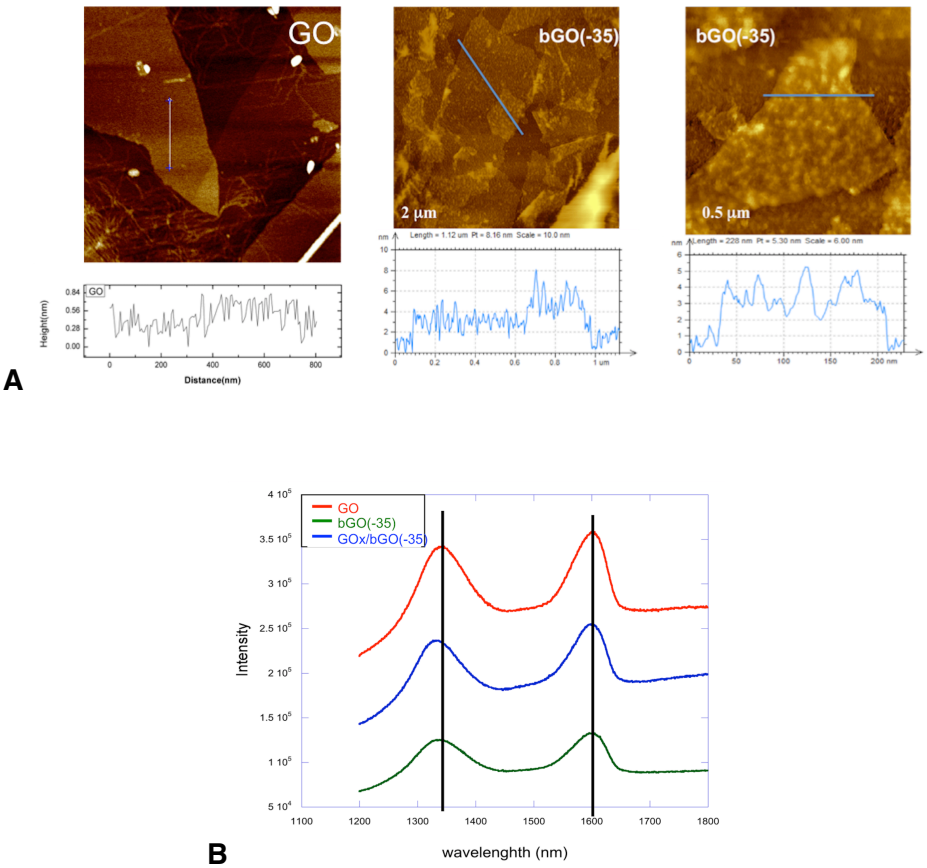

Figure 3.8. AFM images showing decoration of cBSA on GO surface. Height profile analysis on bare GO sheets indicates a uniform surface. But bGO(-35) surface showed an uneven surface with 3-4 nm height, corresponding to the size of cBSA bound to GO. **B.** Raman spectra of bare GO (red), cBSA modified GO (green) and GOx bound BGO(-35) (blue). Both D (~1350) band and G (~1590 cm^{-1}) band for graphene oxide was appeared at expected positions. Peak positions were remaining unchanged after protein modifications indicate that electronic environment of GO is preserved.

The AFM images were collected after mounting the samples on a freshly cleaved mica substrate and the corresponding images are shown. Surface topography of the bare and biophillic graphitic oxide (GO and bGO(-35)) samples were shown in **Figure 3.8.A**. Atomic force micrography of the bare GO sample which presents a planar lamellar structure with distinct edges in accordance with the surface topography of the bare GO nanosheets (**Figure 3.9.A (i))**. **Figure 3.9.A** (**ii-iv**) are the surface topographies of bGO(-35) samples measured by atomic force microscope at three different magnifications. All of these images suggest the structural characteristic of a GO surface is maintained after protein loading. **Figure 3.9.A** (ii-iv) shows the protein deposition on the surface of GO. Moreover, a close look at **Figure 3.9.A** (iv) depicts a uniform deposition of proteins on the nanosheets (**Figure 3.8**) (i) is the AFM image of a bare GO sample, GO samples have the planar lamellar surface structure with sharp edges presenting a polygonal morphology of the nanosheets. **Figure 3.9.A** (ii-iv) is the AFM image of a bGO (-35) sample in water where GO sheets are covered with small dot like formations representing the cBSA adsorption. In **Figure 3.9.A** (iv), it is clearly visible that planar GO nanosheets are almost uniformly covered with the protein. The line scans of the micrographs indicated 3-4 nm height for cBSA bound to GO and bGO(-35) (**Figure 3.8**), which is comparable to the XRD data (51 Å).

Likewise, Cyt *c*, Hb and GOx bound to GO or bGO was characterized by AFM (**Figure 3.9.B**). Evidently, proteins decorated the sheets and the lamellar nature of the staring bGO has been preserved. Proteins appeared as small islands on the nanosheets rather than a uniform deposits. Interestingly, AFM height measurements for GO/GOx showed the peak height increment of 85 Å over the bGO surfaces which supported the d-spacings estimated by powder XRD experiments in representative samples. The AFM image clearly shows the proteins are deposited in form of islands at regions on the surface. The height profile measured by the AFM

peaks at these precise locations, therefore the peak height in the height profile line scan acquired from the AFM is the correct parameters to describe the protein deposition on GO surface. The Raman spectrum shown in **Figure 3.8.B** indicates a red shift of the D-band by 10 cm^{-1}, and is indicative of interaction of the c-BSA with the edge and steps present on the GO surface. Covalent modification of the GO surface with BSA has shown red shifts of both the D and G band by 50 cm^{-1}.[41]

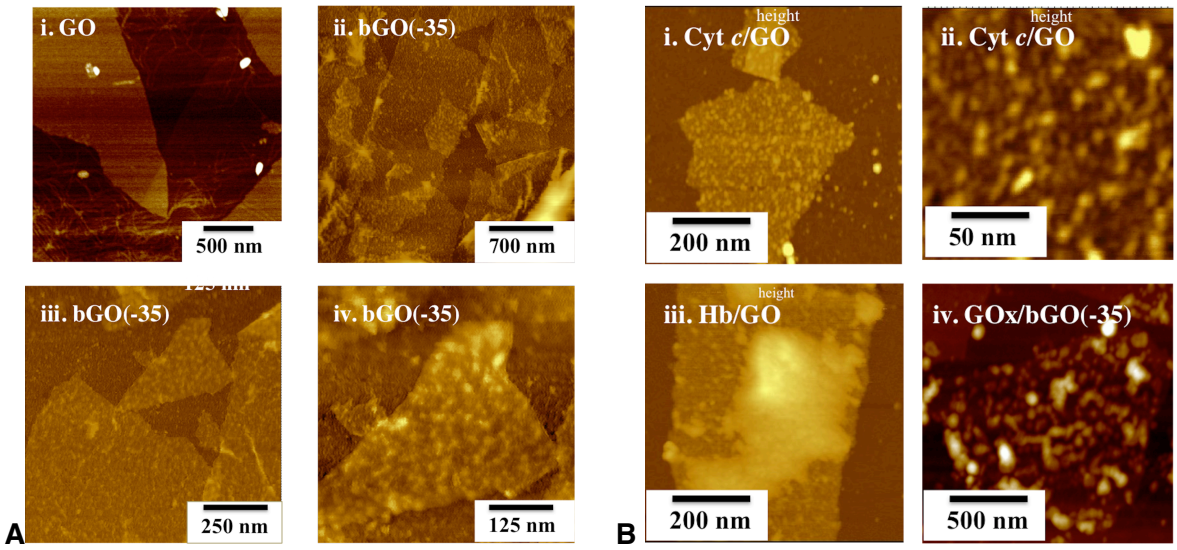

Figure 3.9. A. AFM images of GO and bGO(-35) at different magnifications. cBSA decoration increased the plate thickness. **B**. Binding of Cyt c and Hb to GO and the binding of GOx to bGO(-35) is clearly demonstrated in these images.

3.4.8. Structure and Activity Studies of the Bound Proteins. Thus, far we have shown that the GO layers can be loaded with cBSA, and the loadings of both GOx and Hb improved with cBSA, but it is also important to evaluate the extent of native-like structures of the bound proteins. Circular dichroism (CD) studies were done to examine the secondary structures of the bound proteins. The CD signal intensity at 222 nm of the bound protein is compared with that of the corresponding unbound protein (**Figure 3.10**). Generally as the underlying cBSA concentration increased, the bound protein structure improved, and resembled that of the unbound protein.

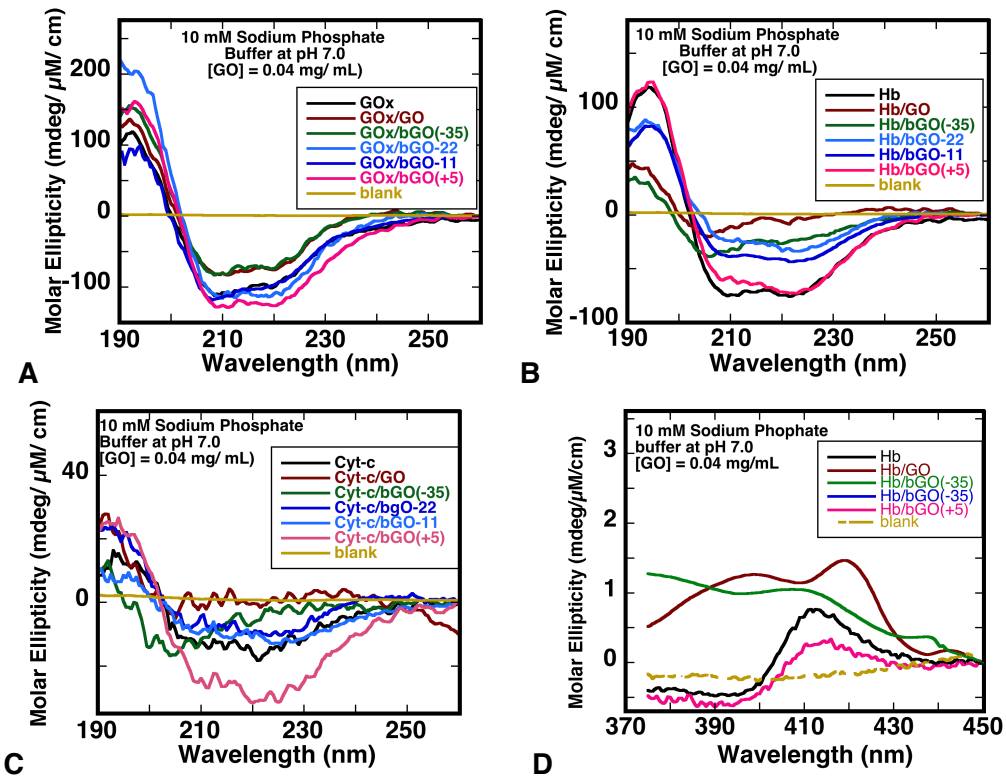

Figure 3.10. Comparison of CD spectra of bGO charge ladders/Enzyme assemblies with free enzyme. Figure **A**, **B** and **C** shows far UV CD spectra for GOx, Hb and Cyt *c* respectively. **D** shows the change in heme environment of Hb/bGO derivatives. Söret band CD of Hb indicates the disturbance of Heme environment in Hb/GO and Hb/bGO(-35) cases worth noted.

The extent of retention of the structure of the bound protein (%) was calculated by comparing the intensity of the CD band of the unbound protein at 222 nm with that of the bound protein at the same wavelength (**Figure 3.11.A**). The % structure retention was plotted as a function of cBSA loading or charge, which are measures of the extent of modification of the GO surface. When Cyt *c* and Hb are bound to bare GO, they lost almost 90% of their CD signals (blue and red lines) but as the cBSA loadings increased, the proteins began to recover their CD signals. On the other hand, GOx retained most of its structure on bare GO (22% loss) but also improved with cBSA loading (green line). In general, increased loading of cBSA, improved bound protein structure.

In another study, we examined activities of bound enzyme, as a function of increasing cBSA loadings (**Figure 3.11.B)**. The activities of Cyt *c*, GOx, and Hb bound to GO, bGO(-35) and bGO(+5) were recorded by recording the initial rates and specific activities have been calculated from this data (10 mM sodium phosphate buffer at pH 7.0). Interestingly, the peroxidase-like activity of Cyt *c* (6.4×10^{-4} $M^{-1}s^{-1}$) was enhanced ~15-fold (9.19×10^{-3} $M^{-1}s^{-1}$) on binding to GO (black bars) and activities reached that of the unbound Cyt *c* upon binding to bGO(-35) or bGO(+5). Specific activities of unbound Hb (2.93×10^{-3} $M^{-1}s^{-1}$) and GOx (5.31×10^{-3} $M^{-1}s^{-1}$) decreased on binding to GO to 50 and 80%, respectively (black bars). However, their binding to bGO(-35) improved the activities (red bars) and on binding to bGO(+5) the activities were nearly the same as those of the corresponding unbound enzymes (green bars). In the case of bGO(+5), the bound enzyme activities were nearly matched to those of the unbound enzymes and proteins. Therefore, except with Cyt *c*, both Hb and GOx indicated improved activities with cBSA loadings.

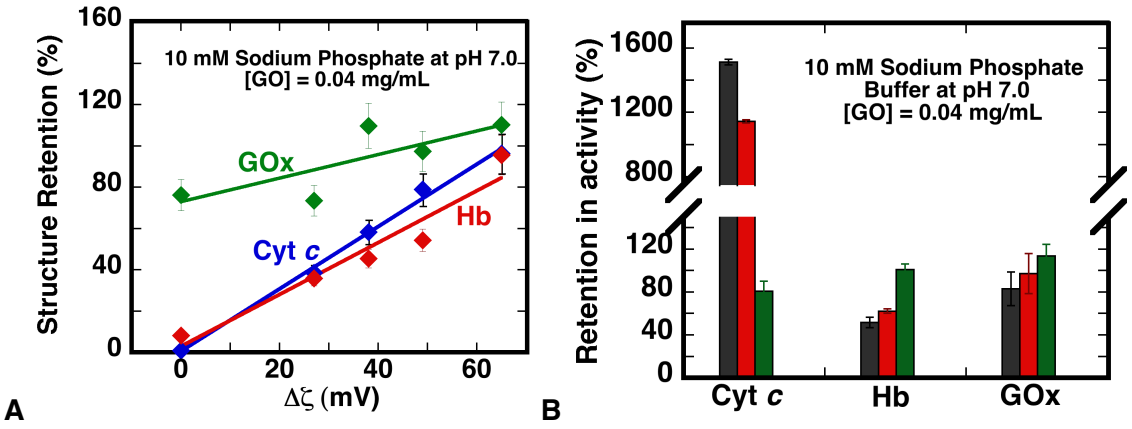

Figure 3.11.A. Plot showing protein structure retention (%) as a function of charge/extent of biophilization (Δζ). Approximate concentration of cBSA used for biophilization of GO (1 mg/mL) shown on the top X-axis. **B**. Retention in enzymatic activity with increasing loadings of cBSA. Cyt *c* showed exceptionally high activities at GO and bGO(-35).

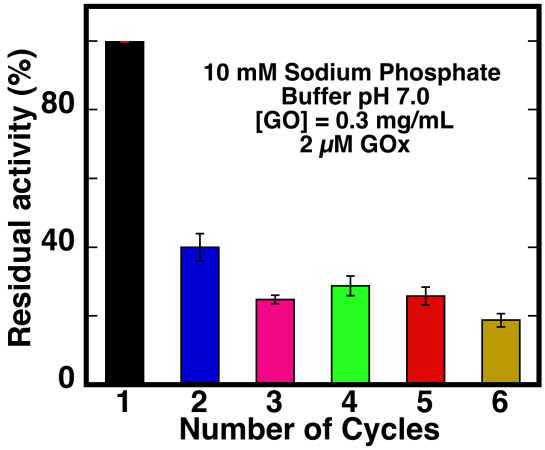

Figure 3.12. Enzyme recyclability study of GOx/bGO(+5) activity. The enzyme composite was recovered after each cycle by centrifugation followed by washing. Residual activity was calculated by taking specific activity at first cycle (red line) as 100%.

3.4.9. Extension to binding of other proteins and enzymes. To test if cBSA would passivate GO for enzyme binding or biophilization of its surface, we examined an additional set of proteins and enzymes (BSA, catalase (Cat), HRP and lysozyme (Lyz)). Solutions of these proteins were equilibrated with GO or bGO(+5), bound proteins were separated from the unbound proteins, and the CD spectra of the bound proteins have been recorded. The extent of structure retention was estimated as before (**Figure 3.13. A-D**) and the extent of structure retention of all the 7 proteins is compared (**Figure 3.13. E**). The blue bars correspond to the % retention of the CD intensities of proteins bound to GO, and most of these proteins lost a significant portion of their native-like structures. On the other hand, red bars represent the extent of structure retention for proteins bound to bGO(+5), and these samples indicated extensive retention of their structures, close to those of the unbound proteins, 100%.

These data clearly show that the adsorption of most enzymes on GO lose their native like structures, while they retain most of their native-like structures on adsorption onto bGO(+5). Thus, GO can be converted into a more biologically compatible material by simple adsorption of cBSA, and this discovery expands the utility of bGO for a variety of new and exciting biological applications.

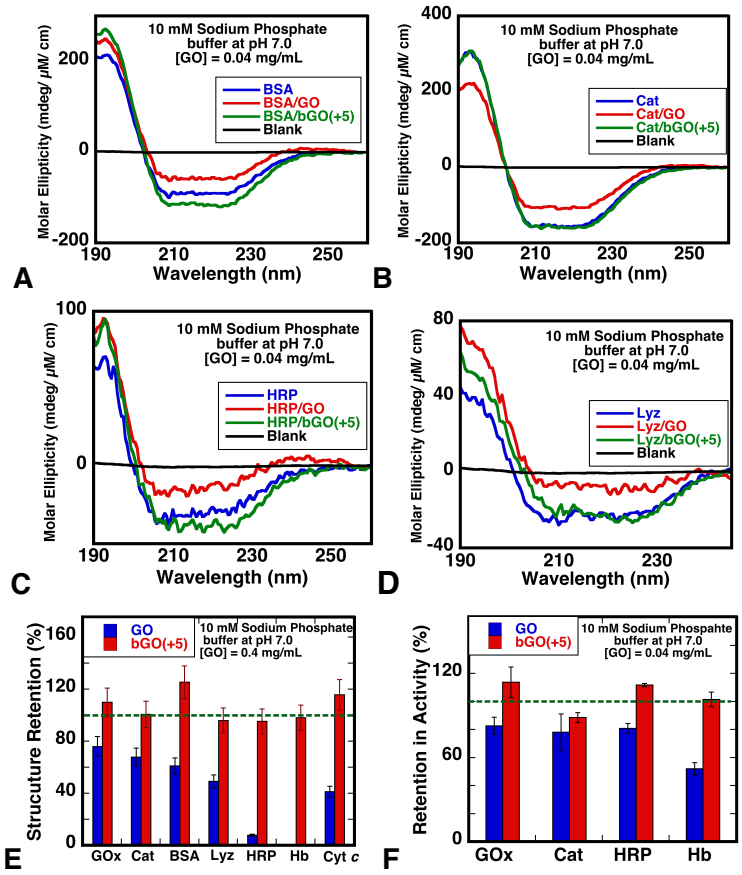

Figure 3.13 .Far UV CD Spectra of **A**. BSA **B**. Catalase **C**. HRP and **D**. Lysozyme at free state (blue), bound to GO (red) and bound to bGO (green). Improved structure retention (**E**) and activity retention (**F**) on bGO(+5) (red bars) in comparison to GO (blue bars) for different enzymes, which are arranged in the order of increasing pI.

3.5. Discussion

Protein-GO interactions are driven by several factors which include, but not limited to, electrostatic, hydrophobic, hydrophilic, and dipolar interactions. Thus, control of this BioNano interface is challenging because of the complexity of these systems. Graphene oxide is attractive to biologists as a platform for biomolecular immobilization. Even though a large number of functional groups and large surface area of GO favors effective binding of proteins, hydrophobic nature of the surface is not benign to many proteins.[17] Therefore, converting GO into a biocompatible material is both challenging and rewarding. Our attempt in this report was to control the surface characteristics of GO in systematic manner so that the structure and function of bound biomolecules can be improved to those of the corresponding unbound biomolecules.

Our hypothesis is that adsorption of a chemically modified protein would serve as a glue to bind GO on one hand and also provide favorable interactions for the benign binding of a variety of biomolecules on its surface. We have chosen BSA for this purpose due to its affinity for a variety of inorganic surfaces, including GO, and its ability to readily denature and cover available surface area. BSA also has several acid and amine functions which can be chemically modified to further control their interactions with both GO as well as the enzymes that are to be adsorbed on GO. Therefore, chemically modified BSA can serve as an excellent 'glue' for effective, high affinity, benign binding of proteins and enzymes to GO. Previously, unmodified BSA was used to coat GO for binding of a number of inorganic nanoparticles and limited applicability for enzyme and protein binding.[28] But the utility of the unmodified BSA is severely limited, it is negatively charged at neutral pH, and it has poor affinity for anionic GO at neutral

pH. Hence, we chose chemical modification of BSA which provided greater control over its properties and facilitated the development of a protein-glue for the biophilization of GO.

There are two major parts to this investigation, one the characterization of the adsorption of the chemically modified BSA to GO, and the other testing the protein and enzyme binding properties of cBSA/GO as a function of cBSA loading. Since GO is known to quench the fluorescence of a number of fluorophores,[20,35] we labeled cBSA with FITC and measured its binding to GO in fluorescence studies. The Stern-Volmer plots indicated an upward curvature due to static quenching resulting from the binding of the cBSA-FITC to GO (**Figure 3.2.A** inset), and data analysis using reported methods indicated that cBSA-FITC bind to GO 78-fold greater than BSA-FITC. In another comparison, the direct binding of green fluorescent protein to GO indicating a Stern-Volmer constant[20] of 13.2 μg^{-1} (9.5 x 10^2 M^{-1}) In comparison our affinity constants of 1.67 x 10^4 M^{-1} for cBSA-FITC is much larger. Hence, chemical modification enhanced the affinity for GO, and cBSA has a high affinity for GO.

cBSA binding to GO is also verified by an independent approach, where the net charge of GO was monitored in the presence of increasing concentrations of cBSA. Zeta potential measurements are widely used in graphene and GO research,[42, 43, 44] to demonstrate pH dependency of suspensions and to validate surface modifications.[45] Our previous work on protein binding to α-zirconium phosphate nanolayers demonstrated this utility.[46] Since cBSA is strongly positively charged and GO is strongly negatively charged, their binding should reduce net charge on GO, and zeta potential provided a simple method to monitor these interactions at the nano-bio interface. The zeta potential of GO increased from -60 to +5 mV by the addition of increasing concentrations of cBSA (0-70 μM, **Figure 3.4**) but addition of BSA to GO, under the same conditions, the charge did not change significantly.

Binding constant obtained for cBSA from the LF fit was about 10 times higher than apparent Stern-Volmer constant (K_a) calculated from fluorescence titrations. This may be due to the non-uniform binding of cBSA to GO such that some regions of GO are distinct from the other regions. This explanation was supported by the heterogeneity index 0.67 deduced from the LF fit. Non-linear fit to the Stern-Volmer curve also indicated such heterogeneity where the fluorophore is not accessible to quenching by GO, meaning that there are some cBSA binding events that are not observed in the fluorescence titration.

Protein binding to GO is expected to be controlled by several factors, which include electrostatic and hydrophobic interactions, as well as specific interactions with carboxyl, and hydroxyl surface groups of GO.[19] But, the adsorption of a near-monolayer of cBSA on GO (please see below) changes the nature of these interactions. To compare and contrast these interactions, we examined the binding affinities of three proteins on three different versions, namely GO, bGO(-35) and bGO(+5). Among all the 9 distinct data points shown in **Figure 3.5.A,** the highest loading of 450% (w/w) was observed for Hb with bGO(+5), where both binding partners are only weakly charged. Therefore, we conclude that electrostatic interactions could be important but not the dominant factors in the interactions with bGO.

The next highest loading of 400% (w/w) was observed with Cyt *c* and GO, and this is consistent with a high positive charge on Cyt *c* (+7)[39] and strong negative charge on GO, and loading dropped to 370% with bGO(-35) and then drastically reduced to 66% with bGO(+5). This outcome is clearly not due to the simple attenuation of electrostatic interactions but rather due to weakening of the hydrophobic interactions where the cBSA competed for binding to hydrophobic sites on GO and converted them into more hydrophilic sites. This argument was

supported by the fact that the extent of structure retention of bound Cyt *c* increased from 0% to 100% when GO was biophilized with cBSA.

Another evidence for the weak contributions of electrostatic interactions to protein binding was noted with GOx. GOx is strongly negatively charged, with a charge of -65 mV at pH 7.0, and it showed poor loading on GO(-60) and bGO(-35), but it showed only minor improvements for binding to the most positively charged bGO(+5) (88% to 113%). Taken together, this data clearly show that binding to GO is not dominated by electrostatic interactions. Since, H-bonding and salt bridges also play vital role in protein-protein interactions adsorbed proteins might make more H-bonds and/or salt bridges with bGO. Hydrophobic interactions may play a major role and they can result in the loss of bound protein structures. However, the adsorption of a sacrificial protein such as chemically modified BSA can effectively block these sites and provide favorable interactions for binding a number of different proteins and enzymes to the BSA-modified GO.

The average thickness of the cBSA layer on GO surface of bGO(+5) was calculated from the maximum loadings of cBSA, the d-spacings noted in the powder XRD data, the average diameter of BSA, and the known surface area of GO (7.05×10^{22} Å^2/g).[5] The average area of cross-section of cBSA was estimated to be 2.23×10^{22} Å^2/g (using the measured d-spacing of 55 Å radius from the XRD data, **Figure 3.7.B**), and the area occupied by a monolayer of cBSA at the maximal loading of (400%, w/w) turned out to be $8.92. \times 10^{22}$ Å^2/g, slightly larger than the total available surface area. Thus, a near monolayer of cBSA is formed at this high loading, which is corroborated by AFM height analysis (**Figure 3.8**). Similar analysis of other proteins bound to GO indicated monolayer to double-layer formation. We expect this surface to be more

compatible with proteins and enzymes due to the variety of amino acid side chains present in the cBSA layer.

A comparative study of equilibrium binding isotherms and zeta potential titrations in specific cases gives an insight to the nature of protein-bGO interactions. Comparison of zeta potential data with binding data showed that system strives to achieve electrostatic neutrality as the protein binding saturates but electrostatic interactions do not appear to dominate the binding. Because, the maximal loading of GOx to GO (88%) was improved only marginally with bGO(+5) (113%) even though GOx is strongly negatively charged (-69). When negatively charged GO interacts with negatively charge GOx, no change in zeta potential was observed even at 80% loading **(Figure 3.6.A**). Hb which is nearly neutral at pH 7, on the other hand, showed a maximum loading of 300% on GO, but its loading steadily improved to 450% with bGO(+5), These observations implied that the contributions of non-electrostatic interactions also contribute to the overall binding phenomena.

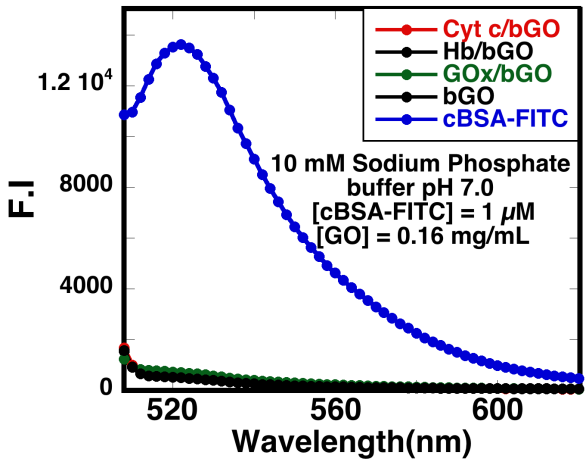

Figure 3.14. Experiment showing the irreversibility of biophilization by ruling out the possibility of displacement of cBSA from GO surface after protein binding. Florescence spectra of BSA-TEPA-FITC shown in blue, which is quenched by addition of GO (0.16 mg/mL; black line.). Absence of increase in fluorescence intensity by the addition of GOx (6 μM), Hb (20 μM) or Cyt *c* (25 μM) rules out the possibility of any flurophore displacement mechanism.

Proteins with higher affinity to an immobilized surface can replace the ones with lower affinities from a given solid surface, which is known as Vroman effect.[47, 48] Thus, in the current case the underlying cBSA layer may be displaced by the added enzymes, and we tested this possibility in fluorescence labeling studies. Displacement of fluorescently labeled cBSA (cBSA-FITC) from GO surface, if any, was followed (**Figure 3.14**), and there was no displacement of the underlying cBSA-FITC by Hb, Cyt *c* or GOx. Thus, cBSA is not being displaced or released into the solution by other proteins, but it could be serving as a glue for benign binding to GO.

The above conclusion was supported by the structural studies of the bound proteins and enzymes bound to GO. Conservation of protein structure is vital for its specific biological function(s). Protein conformational changes are often encountered on binding to a solid surface and they are attributed to the opposing contributions of the surface energy of the sold and the free energy of denaturation ($\Delta G_{D\text{-}N}$) of the protein. Specifically, proteins with low denaturation free energies (less positive values) unfolded or denatured while consuming surface energy of the solid surface. The surface free energy of GO was estimated to be around 62.1 mJ/m^2.[49] Proteins with poor stabilities or those that can interact with the hydrophobic regions of GO tend to lose their structure more readily,[20] as illustrated by HRP/GO.[18]

In the current studies, the Cyt *c* bound to bare GO, for example, lost almost all of its CD signal at 222 nm but gained its CD signal with increased cBSA loading and recovered fully on bGO(+5). The UV CD data show that all three proteins attained nearly 100% retention of their native-like structures as the cBSA loading is increased, which is novel and advantageous. Consistent with these data, the Soret CD of Hb/GO and Hb/bGO (**Figure 3.10.D**) indicated that heme environment is disturbed on binding to GO but heme environment relaxed to its native like structure on binding to bGO(+5). As the cBSA loading increased, thus, the bound protein

structures improved across the board. The activities of the bound enzymes depended on the extents of their structure retention on GO, with one exception. Cyt c/GO showed exceptionally high activity, 15-fold greater than Cyt *c* (**Figure 3.11.A**) despite the fact that it lots most of its structure. Such denaturation and exposure of the heme from Cyt c on GO was cited to be responsible for enhanced electrochemical signals of Cyt c.[50] We did not observe similar enhancements in the activities for Hb or GOx, which also contain hydrophobic prosthetic groups, and therefore it is not a general phenomenon. As the cBSA loading improved, the activities of bound Cyt c diminished while those of Hb and GOx improved steadily, and activities reached nearly 100% of their original values on bGO(+5).

To further test the above hypothesis that increases cBSA loading had a positive influence on the bound enzyme/protein structure, we plotted percent activities as function of their corresponding percent helicity, for four proteins bound to GO at increasing loadings of cBSA (**Figure 3.15**). The plot implies that enzymes/proteins bound to hydrophobic regions of the GO sheets tend to deform their secondary structures and lower activities. As these regions are increasingly covered by cBSA, which functioned as a sacrificial protein layer, the fraction of active enzyme/protein increases proportionately. Protein molecules bound to more hydrophilic regions of the modified GO, or bGO, could be responsible for improved activities. Thus, it is likely that binding to the cBSA layer promotes the native-like structure and activity of the bound proteins. The effect of biophilization on loading of these proteins is showed in supporting information Table S1. Protein loading has been improved after biophilization in most of the cases. Thus, the reported modification of GO with cBSA is a step forward for the development of functionally active graphene-biomaterials with superior properties when compared to untreated GO.

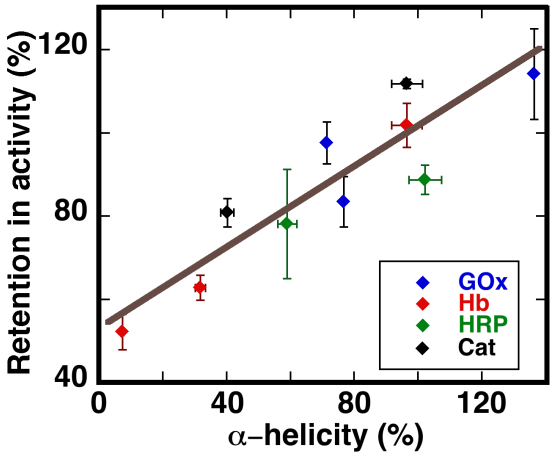

Figure 3.15. Correlation of activity retention with α-helicity (%) of four distinct proteins bound to GO loaded with increased concentrations of cBSA. The linear relationship between structure and activity confirms that improved structure translated to improved activities.

3.6. Conclusions

Non-covalent modification of GO with a systematic manipulation of the bio-nano interface for the benign and superior binding of a number of proteins and enzymes is reported here. This approach should be viable and extendable for the preparation of any protein/GO nanomaterials or to other solid surfaces. The data suggest that electrostatic interactions are important for the enzyme binding on GO and bGO but other interactions also play a very significant role, perhaps a stronger role. The sacrificial cBSA on GO provides a protein-compatible surface for improved activity and structure retention. These insights are important for further manipulation and control of the nano-bio Interface for a variety of applications, without compromising the loading capacity, structure or activities.

3.7. References

1. El-Kady, M. F.; Strong, V.; Dubin, S.; Kaner, R. B.: Laser Scribing of High-Performance and Flexible Graphene-Based Electrochemical Capacitors. *Science* **2012**, *335*, 1326-1330.

2. Katsnelson, M. I.: Graphene: carbon in two dimensions. *Mater. Today* **2007**, *10*, 20-27.

3. Novoselov, K. S.; Geim, A. K.; Morozov, S. V.; Jiang, D.; Zhang, Y.; Dubonos, S. V.; Grigorieva, I. V.; Firsov, A. A.: Electric Field Effect in Atomically Thin Carbon Films. *Science* **2004**, *306*, 666-669.

4. Guo, Y.; Wu, B.; Liu, H.; Ma, Y.; Yang, Y.; Zheng, J.; Yu, G.; Liu, Y.: Electrical Assembly and Reduction of Graphene Oxide in a Single Solution Step for Use in Flexible Sensors. *Adv. Mater.* **2011**, *23*, 4626-4630.

5. Zhang, J.; Zhang, F.; Yang, H.; Huang, X.; Liu, H.; Zhang, J.; Guo, S.: Graphene Oxide as a Matrix for Enzyme Immobilization. *Langmuir* **2010**, *26*, 6083-6085.

6. Huang, C.; Bai, H.; Li, C.; Shi, G.: A graphene oxide/hemoglobin composite hydrogel for enzymatic catalysis in organic solvents. *Chem. Commun.* **2011**, *47*, 4962-4964.

7. Jin, L.; Yang, K.; Yao, K.; Zhang, S.; Tao, H.; Lee, S.-T.; Liu, Z.; Peng, R.: Functionalized Graphene Oxide in Enzyme Engineering: A Selective Modulator for Enzyme Activity and Thermostability. *ACS Nano* **2012**, *6*, 4864-4875.

8. Kuila, T.; Bose, S.; Khanra, P.; Mishra, A. K.; Kim, N. H.; Lee, J. H.: Recent advances in graphene-based biosensors. *Biosens. Bioelectron.* **2011**, *26*, 4637-4648.

9. Cheng, R.; Liu, Y.; Ou, S.; Pan, Y.; Zhang, S.; Chen, H.; Dai, L.; Qu, J.: Optical Turn-On Sensor Based on Graphene Oxide for Selective Detection of d-Glucosamine. *Anal. Chem.* **2012**, *84*, 5641-5644.

10. Shen, H.; Liu, M.; He, H.; Zhang, L.; Huang, J.; Chong, Y.; Dai, J.; Zhang, Z.: PEGylated Graphene Oxide-Mediated Protein Delivery for Cell Function Regulation. *J. Appl. Mater. Interfaces* **2012**, *4*, 6317-6323.

11. Yang, K.; Feng, L.; Shi, X.; Liu, Z.: Nano-graphene in biomedicine: theranostic applications. *Chem. Soc. Rev.* **2013**, *42*, 530-547.

12. Chung, C.; Kim, Y.-K.; Shin, D.; Ryoo, S.-R.; Hong, B. H.; Min, D.-H.: Biomedical Applications of Graphene and Graphene Oxide. *Acc. Chem. Res.* **2013**, *46*, 2211-2224.

13. Shen, J.; Yan, B.; Shi, M.; Ma, H.; Li, N.; Ye, M.: Synthesis of graphene oxide-based biocomposites through diimide-activated amidation. *J. Colloid Interface Sci.* **2011**, *356*, 543-549.

14. Wang, Y.; Li, Z.; Wang, J.; Li, J.; Lin, Y.: Graphene and graphene oxide: biofunctionalization and applications in biotechnology. *Trends Biotechnol.* **2011**, *29*, 205-212.

15. Georgakilas, V.; Otyepka, M.; Bourlinos, A. B.; Chandra, V.; Kim, N.; Kemp, K. C.; Hobza, P.; Zboril, R.; Kim, K. S.: Functionalization of Graphene: Covalent and Non-Covalent Approaches, Derivatives and Applications. *Chem. Rev.* **2012**, *112*, 6156-6214.

16. Pavlidis, I.; Vorhaben, T.; Gournis, D.; Papadopoulos, G.; Bornscheuer, U.; Stamatis, H.: Regulation of catalytic behaviour of hydrolases through interactions with functionalized carbon-based nanomaterials. *J. Nanopart. Res.* **2012**, *14*, 1-10.

17. Mu, Q.; Su, G.; Li, L.; Gilbertson, B. O.; Yu, L. H.; Zhang, Q.; Sun, Y.-P.; Yan, B.: Size-Dependent Cell Uptake of Protein-Coated Graphene Oxide Nanosheets. *J. Appl. Mater. Interfaces* **2012**, *4*, 2259-2266.

18. Zhang, Y.; Zhang, J.; Huang, X.; Zhou, X.; Wu, H.; Guo, S.: Assembly of Graphene Oxide–Enzyme Conjugates through Hydrophobic Interaction. *Small* **2012**, *8*, 154-159.

19. Zhang, Y.; Wu, C.; Guo, S.; Zhang, J.: Interactions of graphene and graphene oxide with proteins and peptides. In *Nanotechnology Reviews*, 2013; Vol. 2; pp 27.

20. Chou, S. S.; De, M.; Luo, J.; Rotello, V. M.; Huang, J.; Dravid, V. P.: Nanoscale Graphene Oxide (nGO) as Artificial Receptors: Implications for Biomolecular Interactions and Sensing. *J. Am. Chem. Soc.* **2012**, *134*, 16725-16733.

21 . Duff, M. R.; Kumar, C. V.: Molecular Signatures of Enzyme–Solid Interactions: Thermodynamics of Protein Binding to α-Zr(IV) Phosphate Nanoplates. *The Journal of Physical Chemistry B* **2009**, *113*, 15083-15089.

22. Kumar, C. V.; Chaudhari, A.: Proteins Immobilized at the Galleries of Layered α-Zirconium Phosphate: Structure and Activity Studies. *J. Am. Chem. Soc.* **2000**, *122*, 830-837.

23. Duff, M. R.; Kumar, C. V.: Protein–Solid Interactions: Important Role of Solvent, Ions, Temperature, and Buffer in Protein Binding to α-Zr(IV) Phosphate. *Langmuir* **2009**, *25*, 12635-12643.

24. Maalej, N.; Albrecht, R.; Loscalzo, J.; Folts, J. D.: The potent platelet inhibitory effects of S-nitrosated albumin coating of artificial surfaces. *Journal of the American College of Cardiology* **1999**, *33*, 1408-1414.

25. Smith, R.; Mosesson, M. W.; Daniels, A. U.; Gartner, T. k.: Adhesion of microvascular endothelial cells to metallic implant surfaces. *Journal of Materials Science: Materials in Medicine* **2000**, *11*, 279-285.

26. Kim, K. S.; Um, Y. M.; Jang, J.-r.; Choe, W.-S.; Yoo, P. J.: Highly Sensitive Reduced Graphene Oxide Impedance Sensor Harnessing π-Stacking Interaction Mediated Direct Deposition of Protein Probes. *J. Appl. Mater. Interfaces* **2013**, *5*, 3591-3598.

27 . Kumar, C. V.; Duff, M. R.: DNA-Based Supramolecular Artificial Light Harvesting Complexes. *J. Am. Chem. Soc.* **2009**, *131*, 16024-16026.

28. Liu, J.; Fu, S.; Yuan, B.; Li, Y.; Deng, Z.: Toward a Universal “Adhesive Nanosheet” for the Assembly of Multiple Nanoparticles Based on a Protein-Induced Reduction/Decoration of Graphene Oxide. *J. Am. Chem. Soc.* **2010**, *132*, 7279-7281.

29 Hummers, W. S.; Offeman, R. E.: Preparation of Graphitic Oxide. *J. Am. Chem. Soc.* **1958**, *80*, 1339-1339.

30. Hummers, W. S.; Offeman, R. E.: Preparation of Graphitic Oxide. *J. Am. Chem. Soc.* **1958**, *80*, 1339-1339.

31 . Lakowicz, J.: *Principles of Fluorescence Spectroscopy*; Kluwer Academic/Plenum Publishers: New York, Boston, Dordrecht, London, Moscow, 1999.

32. Kim, J. H., Yoon, J. H.: Protein Adsorption on Polymer Particles. In *Encyclopedia of Surface and Colloid Science*; Marcel Dekker, Inc.: New York, 2002; pp 4373-4381.

33. Pütter, J.: Peroxidases. In *Methods of Enzymatic Analysis (Second Edition)*; Hans, U. B., Ed.; Academic Press, 1974; pp 685-690.

34. Gibson, Q. H.; Swoboda, B. E. P.; Massey, V.: Kinetics and Mechanism of Action of Glucose Oxidase. *J. Biol. Chem.* **1964**, *239*, 3927-3934.

35. Fologea, D.; Ledden, B.; McNabb, D. S.; Li, J.: Electrical characterization of protein molecules by a solid-state nanopore. *Appl. Phys. Lett.* **2007**, *91*, 053901-3.

36. Swathi, R. S.; Sebastian, K. L.: Long range resonance energy transfer from a dye molecule to graphene has (distance)[sup -4] dependence. *J. Chem. Phys* **2009**, *130*, 086101-3.

37. Zuo, X.; He, S.; Li, D.; Peng, C.; Huang, Q.; Song, S.; Fan, C.: Graphene Oxide-Facilitated Electron Transfer of Metalloproteins at Electrode Surfaces. *Langmuir* **2009**, *26*, 1936-1939.

38. Hodak, J.; Etchenique, R.; Calvo, E. J.; Singhal, K.; Bartlett, P. N.: Layer-by-Layer Self-Assembly of Glucose Oxidase with a Poly(allylamine)ferrocene Redox Mediator. *Langmuir* **1997**, *13*, 2708-2716.

39. Gary-Bobo, C. M.; Solomon, A. K.: Properties of Hemoglobin Solutions in Red Cells. *The Journal of General Physiology* **1968**, *52*, 825-853.

40. Koppenol, W. H.; Rush, J. D.; Mills, J. D.; Margoliash, E.: The dipole moment of cytochrome c. *Molecular Biology and Evolution* **1991**, *8*, 545-558.

41. Shen, J.; Shi, M.; Yan, B.; Ma, H.; Li, N.; Hu, Y.; Ye, M.: Covalent attaching protein to graphene oxide via diimide-activated amidation. *Colloids Surf., B* **2010**, *81*, 434-438.

42. Park, J. S.; Cho, S. M.; Kim, W.-J.; Park, J.; Yoo, P. J.: Fabrication of Graphene Thin Films Based on Layer-by-Layer Self-Assembly of Functionalized Graphene Nanosheets. *J. Appl. Mater. Interfaces* **2011**, *3*, 360-368.

43. Li, D.; Muller, M. B.; Gilje, S.; Kaner, R. B.; Wallace, G. G.: Processable aqueous dispersions of graphene nanosheets. *Nat Nano* **2008**, *3*, 101-105.

44. Vickery, J. L.; Patil, A. J.; Mann, S.: Fabrication of Graphene–Polymer Nanocomposites With Higher-Order Three-Dimensional Architectures. *Adv. Mater.* **2009**, *21*, 2180-2184.

45. Zhu, Y.; Cai, W.; Piner, R. D.; Velamakanni, A.; Ruoff, R. S.: Transparent self-assembled films of reduced graphene oxide platelets. *Appl. Phys. Lett.* **2009**, *95*, 103104-3.

46. Pattammattel, A.; Deshapriya, I. K.; Chowdhury, R.; Kumar, C. V.: Metal-Enzyme Frameworks: Role of Metal Ions in Promoting Enzyme Self-Assembly on α-Zirconium(IV) Phosphate Nanoplates. *Langmuir* **2013**, *29*, 2971-2981.

47. Vroman, L.; Adams, A.; Fischer, G.; Munoz, P.: Interaction of high molecular weight kininogen, factor XII, and fibrinogen in plasma at interfaces. *Blood* **1980**, *55*, 156-159.

48. Ortega-Vinuesa, J. L.; Hidalgo-Álvarez, R.: Sequential adsorption of F(ab′)2 and BSA on negatively and positively charged polystyrene latexes. *Biotechnol. Bioeng.* **1995**, *47*, 633-639.

49. Diederix, R. E. M.; Ubbink, M.; Canters, G. W.: Effect of the Protein Matrix of Cytochrome c in Suppressing the Inherent Peroxidase Activity of Its Heme Prosthetic Group. *ChemBioChem* **2002**, *3*, 110-112.

50. Wang, S.; Zhang, Y.; Abidi, N.; Cabrales, L.: Wettability and Surface Free Energy of Graphene Films. *Langmuir* **2009**, *25*, 11078-11081.

***

4

Biological Relevance of Oxidative Debris Present in as-prepared Graphene Oxide

4.1. Abstract

The influence of oxidative debris (OD) present in as-prepared graphene oxide (GO) suspensions on proteins and its toxicity to human embryonic kidney cells (HEK-293T) are reported here. The OD was removed by repeated washing with aqueous ammonia to produce the corresponding base-washed GO (bwGO). The loading (w/w) of bovine serum albumin (BSA) was increased by 85% after base wash, whereas the loading of hemoglobin (Hb) and lysozyme (Lyz), respectively, was decreased by 160% and 100%. The secondary structures of 13 different proteins bound to bwGO were compared with the corresponding proteins bound to GO using UV circular dichroism spectroscopy. There was a consistent loss of protein secondary structure with bwGO when compared with proteins bound to GO, but no correlation between either the isoelectric point or hydrophobicity of the protein. All enzymes bound to bwGO and GO indicated significant activities, and a strong correlation between the enzymatic activity and the extent of structure retention was noted, regardless of the presence or absence of OD. At low loadings (<100 μg/mL) both GO and bwGO showed excellent cell viability but substantial cytotoxicity (~40% cell death) was observed at high loadings (>100 μg/mL). In control studies, OD by itself did not alter the growth rate even after a 48-h incubation. Thus, the presence of OD in GO played a very important role in controlling the chemical and biological nature of the

protein-GO interface and the presence of OD in GO improved its biological compatibility when compared to bwGO.

4.2. Introduction

The role of oxidative debris (OD) present in graphene oxide (GO) in influencing its interactions with a small set of biological samples such as proteins and cells are examined here. Interactions of proteins with graphene oxide (GO) are a subject of great interest for their potential applications in biology.[1] A clear understanding of the behavior and the effect of GO on biomolecules is essential for building functional, catalytic, sensing, medical, and artificial bio-systems using GO. Interactions of proteins with certain (nano)materials are well-studied, which allows one to predict their affinity, structure, and stability.[2] However, GO is a highly heterogeneous surface with oxygenated functional groups such as hydroxyls, carboxyls and epoxides that are randomly distributed in a hydrophobic 2D carbon basal plane, along with peripheral carboxylate functions at the edges of the sheets (**Scheme 4.1**). The heterogeneity of GO surface makes it more challenging to predict the behavior of biomolecules at its interface.[3]

Structural denaturation of proteins at GO, because of unfavorable interactions with hydrophobic protein interior, adversely affects the protein function.[4] Thus, several surface passivation approaches were established to mask unfavorable hydrophobic interactions [5] to prevent protein denaturation. Modulation in enzyme properties such as, decrease or increase in enzymatic activity,[4,5,6] and complete inhibition[7] on binding of enzymes to GO was illustarted before. The conformation and orientation of protein surface around the active site play a major role in determining the modulation of enzymatic activities.[7] Chemical functionalization, [8] reduction, and passivation with proteins[9, 10] or polymers,[11] can successfully passify GO surface and stabilize certain proteins and enzymes. Reports suggest that the extent of hydrophobicity plays a major role in retaining protein structure and thereby their function.[5]

Recent advances in structural studies of GO have identified the presence of small, highly oxidized polycyclic aromatic moieties called oxidative debris (OD) in GO suspensions.[12] In addition, decrease in conductivity,[13] increase in fluorescence,[16] increase in electrochemistry[14] and decrease in interactions of GO with small molecules[15] are due to the presence of OD. Treating GO with aqueous base solutions separates this debris (**Scheme 4.1**), and resulting debris-free GO (bwGO) has several desirable properties.[16] Thus, an interesting question arises as to how and to what extent OD disturbs biological properties of GO? To date, no such investigation has been carried out to investigate the role of OD in controlling the interactions of GO with biological molecules. Biological applications of GO are currently actively pursued.[1, 17] Therefore, it is critical to analyze the nature of bio-GO interface in the absence of OD. Moreover, the structure of bwGO is closer to graphene than to GO and, therefore, it is important to examine the influence OD present in GO on its interactions with proteins, enzymes and other biomolecules.

Here, we report the role of OD at GO interface in controlling the properties of a set of 13 different proteins with increasing isoelectric points (pH where the net charge on the protein is zero, pI), molecular weight, and the number of surface arginines (SI, Table S1). Our results suggest that OD plays a major role in controlling the protein binding affinities, as well as the retention of structure/enzymatic activities. Binding interactions of proteins with GO and bwGO, structure retention and enzymatic activities were analyzed using multiple spectroscopic methods (**Scheme 4.1**). Furthermore, cytotoxicity of GO, bwGO as well as OD and differences in their toxicities are examined here. Our current study gives an insight into the fundamental understanding of bio-GO interactions at molecular level such as the role of surface functionalities and their nature in determining the affinity, protein secondary structure, and

enzymatic activities. This information would be valuable for the rational control of protein behavior at different surfaces using molecular level information of the interface.

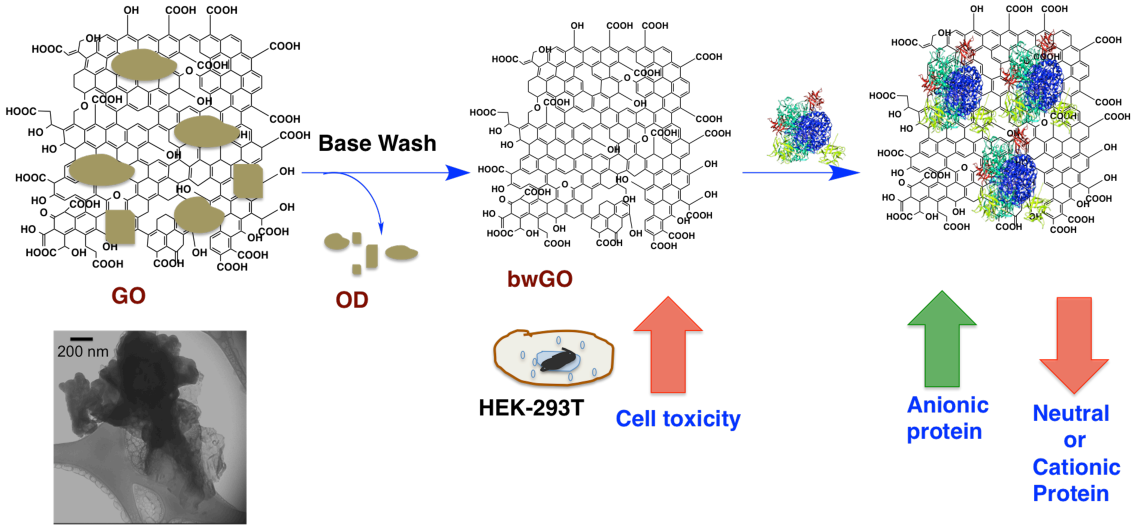

Scheme 4.1. Oxidative debris (OD) was removed from graphene oxide (GO), by washing with aqueous ammonia, and the influence of OD on enzyme-GO interface has been examined. OD protects the bound enzymes from structure/activity loss and decreases cytotoxicity.

4.3. Materials and Methods

4.3.1. Materials. Graphite flakes, guaiacol, KMnO4, Glucose oxidase (GOx, Aspergillus niger), lysozyme (egg white), human serum albumin (HSA), RNase A, betalactoglobulin (BLG), Ovalbumin (egg white) and myoglobin (bovine) were purchased from Sigma Aldrich (St. Louis, MO). Horseradish Peroxidase (HRP) and cytochrome c (equine heart) were obtained from Calzyme laboratories Inc. (San Luis Obispo, CA). Pepsin A, Catalase and Trypsin (Bovine) were bought from Worthington Biomedical Corporation (Lakewood, NJ). (Met-hemoglobin (Bovine) was purchased from MP biomedicals, LLC (Solon, OH). The human embryonic kidney (HEK 293T) cells were purchased from American Type Culture Collection (ATCC, Manassas, VA) and the growth media components viz. Dulbecco's Modified Eagle Media (DMEM) and Fetal Bovine Serum (FBS) were purchased from Gibco ® respectively. The metabolic activity of HEK 293T cells was analyzed with the Cell Counting Kit (CCK-8^{TM}) purchased from Dojindo Molecular Technologies Inc.

4.3.2. Preparation of GO and bwGO. GO was prepared by modified Hummers method as reported elsewhere.[18] bwGO was prepared by washing GO suspension with aqueous ammonia.[16] The base wash procedure with ammonia compared to conc. NaOH has practical advantage in obtaining pure OD without any solid NaCl (product of neutralization of NaOH with HCl). Briefly, GO solution (2 mg/mL, 100 mL) was stirred with 40 mL aq. NH_3 at 100^{o}C until the solution was separated in to two different phases (~3 h). bwGO was separated from OD by repeated centrifugation and was neutralized by repeated washing with water (3-5 times) and re-suspended in 10 mM sodium phosphate buffer (pH 7.0). OD was obtained from the aqueous ammina layer after evaporating the base at 100 °C.

4.3.3. Fluorescence quenching experiments. FlexStation® (Molecular Devices, Sunnyvale, CA) was used for this experiment in a standard opaque 96 well plate with 0.250 mL volume in each well. BSA was labeled with fluorescein isothiocyanate (FITC) for this experiment, with the assumption that the quenching efficiency of bwGO and GO is near identical. BSA-FITC (1 μM) was titrated against different concentrations of GO (0.8 mg/mL) or bwGO (0.8 mg/mL). FITC emission at 525 nm upon excitation at 485 nm was used to tabulate the quenching data. The data fit into modified Stern-Volmer equation, as reported before (equation 1),[10]

$$F0/(F0-F)=1/(f_a K_a [Q])+1/f_a \quad \text{----- (equation 1),}$$

where [Q] = quencher concentration; F_0 = Fluorescence intensity when [Q] = 0; F = Fluorescence intensity at given [Q]; K_a = Bimolecular quenching constant, and f_a = fraction of the initial fluorescence accessible to the quencher.

4.3.4. Protein binding studies. Stock solutions of proteins (hemoglobin or lysozyme) were prepared in 10 mM phosphate buffer pH 7.0. To determine the concentration, absorbance was measured at 406 nm for hemoglobin and 280 nm for lysozyme. For hemoglobin, a set of solutions with a concentration range of 5, 10, 15, 20, 25, and 30 µM were prepared in phosphate buffer pH 7.0 with 0.2 mg/mL GO and 0.2 mg/mL bwGO. For lysozyme, six solutions of concentrations 10, 20, 30, 40, 50, and 60 µM were prepared, equilibrated with same GO and bwGO concentrations (0.2 mg/mL). All solutions were allowed to sit for 1 h for complete equilibration. The solutions were centrifuged for 20 min at 12,000 rpm to aspirate free proteins. Absorbance measurements were taken for the supernatant liquid at the same wavelengths previously used to determine the concentration of free protein in the solutions. The adsorption isotherms were analyzed using Langmuir adsorption model, using the following equation2,[19] to obtain the binding affinity and theoretical adsorption maxima,

$Q = (K Q(sat))/([1+K])$ ------ (Equation 2)

where K = dissociation constant (in μM), Q = binding density at equilibrium (in μmol/mg), C_e = protein concentration (in μM) and Q_{sat} = saturation binding point.

4.3.5. Circular Dichroism Studies. Far UV CD spectra (260 – 190 nm) of protein solutions were recorded on a Jasco J-710 CD spectrometer (Easton, MD) before and after binding to GO or bwGO (0.20 mg/mL) using a 0.05 cm path length quartz cuvette. Protein to GO or bwGO ratio was kept same in all the samples as 50% (w/w) for fair comparison between proteins. All the spectra presented here were corrected for background signal from the buffer and normalized to 1 μM concentration of the protein. Relative structure retention of the conjugates was compared using ellipticity at 222 nm of the unbound protein as standard.

4.3.6. Activity Studies. Solutions of hemoglobin (Hb, 8 µM), myoglobin, (Mb, 12 µM), catalase (Cat, 0.8 μM) and glucose oxidase (GOx, 4 μM) was equilibrated with GO or bwGO (0.2 mg/mL) in pH 7.0 phosphate buffer at 25 ^{o}C, prior to activity assays. Peroxidase-like activity[20] of Hb and Mb was performed to compare the activity of proteins bound to GO or bwGO. For the activity assay, 1 µM hemoglobin, 2.5 mM guaiacol, and 4 mM H_2O_2 were reacted in pH 7.0 phosphate buffer and the activity was monitored by absorbance measurement of guaiacol dimer formation at 470 nm. Similarly, for myoglobin solutions, 1.5 µM myoglobin, 2.5 mM guaiacol, and 4 mM H_2O_2 were reacted in pH 7.0 phosphate buffer and the activity was determined. For each of catalase solutions, 0.1 µM catalase and 20 mM H_2O_2 were reacted in pH 7.0 phosphate buffer and the activity was determined by following decomposition of H_2O_2 monitored by absorption measurement at 240 nm.[21] GOx was assayed for its oxidase activity to glucose using a bienzyme assay coupled with horseradish peroxidase using known protocols.[22]

4.3.7. Cytotoxicity assay. The cytocompatibility of OD, GO, and bwGO was investigated by co-incubating them with human embryonic kidney (HEK 293T) cells, one of the well-characterized and widely used human cell lines available. The standard growth conditions of 37°C, 5% CO_2 and 95% relative humidity (RH) were maintained throughout the experiment and the intracellular metabolic rate was determined using CCK-8 kit as described elsewhere. [23, 24]

Briefly, 0.5 x 10^5 cells were seeded in each well of a 24 well plate in 500 μl of complete growth media [Dulbecco's The suspensions were further diluted with cell culture media and quickly vortexed before they were introduced to the adherent cells at a concentration range of 10, 25, 50, 75, 100, 250 and 500 μg/mL. During the co-incubation phase, the cell morphology was constantly monitored using light microscopy. The intracellular metabolic rate was assessed after 24 h of co-incubation period by using CCK-8 kit that contains a tetrazolium salt, WST-8, which got reduced by dehydrogenase activity of live cells to generate a yellow-colored formazan dye. The amount of the formazan dye thus generated, was quantified spectrophotometrically at 450nm and directly proportional to the number of living cells. Appropriate negative controls, where the CCK-8 kit reagent (50 μl per well) was substituted with equal volume of PBS, were used for each concentration of GO, bwGO and OD whereas the positive control consisted of 50 μl of WST-8 solution added to the pristine cells grown in 500 μL of growth media.

4.4. Results

The presence of OD has been shown to have a role in determining the chemical biological properties of GO. The interactions of OD-free GO, bwGO, are significantly different from that of GO, which influenced the structural and functional properties of a wide range of proteins bound to it. The cell toxicity levels of bwGO and OD are compared with that of GO, and an increase in toxicity after the removal of OD is noted. Detailed descriptions of our results follow.

4.4.1. Preparation and characterization of bwGO. The as-prepared GO[18] was subjected to repeated washing with aqueous ammonia, washed with deionized water to remove the base, and characterized the resulting bwGO as well as the oxidative debris by fluorescence spectroscopy (**Figure 4.1.A and B**), and Raman spectroscopy (**Figure 4.1.C**). The quantity of OD accounted for ~30% (w/w) in a 100 mL, 1 mg/mL GO suspension. While the bwGO and GO showed no fluorescence upon excitation at 350 nm, OD indicated broad emission centered around 440 nm,[16] which is consistent with the presence of polycyclic aromatic debris in OD.

The Raman spectra of GO and bwGO are essentially the same with D band at 1350 cm^{-1} and G band centered around 1600 cm^{-1} (**Figure 4.1.C**), as reported in the literature.[14] These identical Raman signals before and after base-wash indicated that there have been no additional defect sites introduced in bwGO upon the base wash. No significant change in I_D/I_G ratio**.**

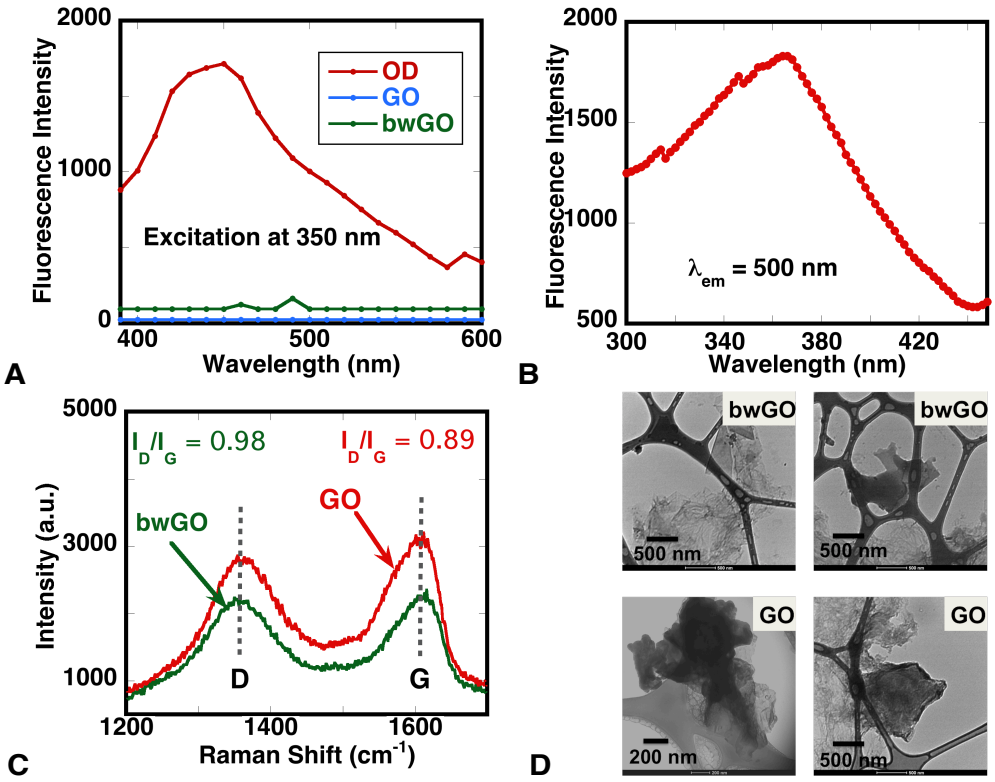

Figure 4.1. A. Fluorescence spectra of OD (50 μg/mL), GO (150 μg/mL) and bwGO (150 μg/mL) in 10 mM sodium phosphate buffer at pH 7.0. OD shows a characteristic peak at 450 nm (excitation at 350 nm) whereas GO and bwGO showed no noticeable peaks at the same region, proves the separation step. **B.** Excitation spectra of OD (200 μg/mL) show emission maxima around 350 nm, with emission monitored at 500 nm. **C.** Raman spectra of GO and bwGO show no significant change in position or intensity of D and G bands. This proves that no additional defects were introduced to the graphitic plane by base wash. **D.** TEM images of GO and bwGO show similar morphology.

4.4.2. Protein binding studies. We examined the interactions of a few proteins such as bovine serum albumin (BSA, pI 4.2), met-hemoglobin (Hb, 7.0), lysozyme (Lyz, pI=12) and ten other proteins in binding studies with GO and bwGO.

We labeled BSA with fluorescein-isothiocyanate (FITC) and examined its binding to GO in quenching studies. GO quenches BSA-FITC fluorescence and binding has been monitored as a function of increasing concentrations of GO, at fixed BSA-FITC concentration.[10] The quenching data have been analyzed by reported methods (**Figure 4.2**) to estimate the binding affinities (Ka).

Equation 1 was used to fit the quenching data where [Q] = quencher concentration (GO/bwGO); F_0 = Fluorescence intensity in the absence of quencher; F = Fluorescence intensity at given [Q]; K_a = Bimolecular affinity constant, and f_a = fraction of the initial fluorescence. Thus, from the slope ($1/K_af_a$) and y-intercept ($1/f_a$) of the fitted line, K_a was calculated. The quenching constants were compared with the assumption that both bwGO and GO quench the fluorescence to the same extent, and Ka for GO 5.7 (±0.8) x 10^3 mL/mg and 6.8 (±1.2) x 10^3 mL/mg. Clearly, the affinity of BSA increased when OD has been removed.

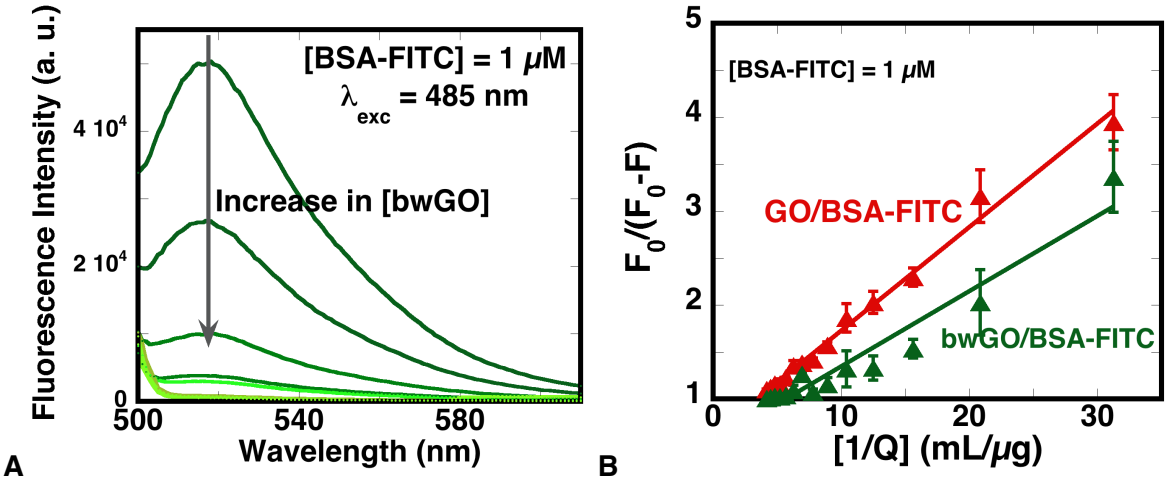

Figure 4.2. Quenching of fluorescence of FITC labeled BSA (BSA-FITC) by the addition of GO or bwGO due to binding to the nanosheets **A.** Fluorescence spectra of BSA-FITC in the presence of increasing concentrations of bwGO upon excitation at 485 nm. **B.** Stern-Volmer fit for the quenching of BSA-FITC emission by GO (red line) or bwGO (green line). The corresponding affinity constants are 5.7 (±0.8) x 10^3 mL/mg and 6.8 (±1.2) x 10^3 mL/mg for GO and bwGO, respectively.

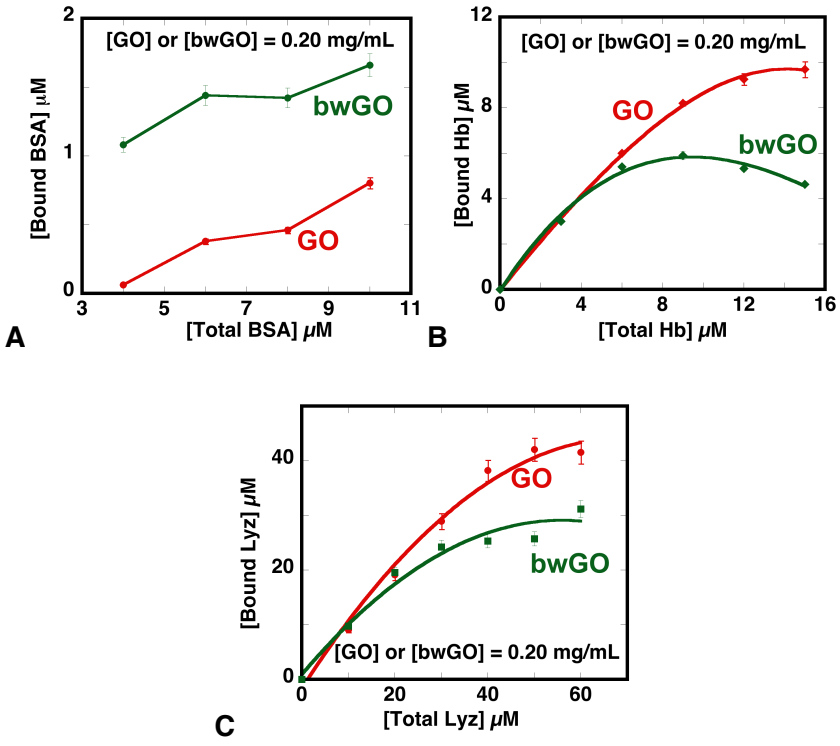

Figure 4.3. Binding isotherms of **(A)** BSA, **(B)** Hb and **(C)** Lyz with GO (0.20 mg/ml) and bwGO (0.20 mg/ml) in phosphate buffer, pH 7.0. Affinities increased from BSA to Hb to Lyz, which corresponded to increase in net charge on the protein.

Binding of proteins to GO and bwGO was also investigated in equilibrium binding studies, where the samples were equilibrated with protein solutions, and unbound protein has been separated by centrifugation. Unbound protein concentration was determined by its absorbance at 280 nm for BSA and Lysozyme, while absorbance at 406 nm has been monitored for hemoglobin samples. These adsorption isotherms are shown in **Figure 4.3**.

The affinity of BSA increased after the base wash (**Figure 4.3.A**, green line), which is in good agreement with the above fluorescence studies. In the cases of both Hb and Lyz, the binding to bwGO was similar to that of GO (**Figure 4.3.B** and **C**, red lines for GO and blue lines for bwGO) at low protein concentrations of 5-10 μM for Hb and 10-20 μM for Lyz. But at higher protein concentrations (>10 and >20 for Hb and Lyz, respectively), protein loading on bwGO was less than that of GO, under the same conditions. Maximum loading (w/w) of BSA was increased after base-wash by 85%, that of Hb decreased by 160% and that of Lyz decreased by 100%. The binding of GOx to GO was negligible at low protein concentrations, while bwGO showed a maximal loading of 64% (**Figure 4.4**), and in case of GO it decreased to 52%.

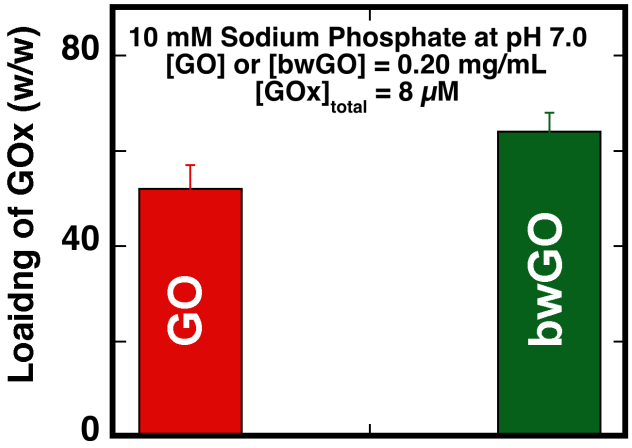

Figure 4.4. Loading efficiency (%) of GOx/bwGO (red) and GOx/bwGO (green) shows increased binding of GOx to bwGO.

Langmuir model of Hb and Lyz adsorption to the nanosheets showed clear differences in binding affinities after base wash (Table 1). The Ka for Hb to GO was 1.9 (± 0.6) x 10^7 M^{-1}, whereas the affinity decreased substantially for bwGO (3.6 (± 2.1) x 10^6 M^{-1}). Lyz showed strong adsorption to GO with Ka of 8.1 (± 3.5) x 10^7 M^{-1}, and it decreased to 2.8 (± 0.8) x 10^7 M^{-1} for bwGO. The decrease in affinity is also reflected in the adsorption parameter, Qsat, which represents the theoretical maximum for monolayer formation of the protein (in μmol) per solid (in mg). As expected, Hb and Lyz showed significant drop in maximal loadings (2-3 fold), which suggests weaker adsorption of proteins to bwGO.

Table 4.1. Parameters obtained by the analysis of the binding isotherms using the Langmuir adsorption isotherm (equation 2)[19]

System	K_a (M^{-1})	Maximal Loading, Q_{sat} (μmol/mg)	R^2
Hb /GO	1.9 (± 0.6) x 10^7	124 (± 26)	0.99
Hb/bwGO	3.6 (± 2.1) x 10^6	38 (± 8)	0.94
Lyz/GO	8.1 (± 3.5) x 10^7	530 (± 152)	0.98
Lyz/bwGO	2.8 (± 0.8) x 10^7	219 (± 26)	0.97

4.4.3. Zeta Potential Titrations. To further characterize the changes in bio-nano interactions, the zeta potential titrations of proteins with GO and bwGO were carried out (**Figure 4.5**). The zeta potential of bwGO decreased from -33 mV (no protein added) to -18 mV when Hb concentration was increased from 0 to 22 μM while that of GO increased from -35 to -12 mV over the same protein concentration range. This shows the reduced binding affinity of Hb to bwGO, supporting the adsorption studies. In contrast to Hb, Lyz showed essentially the same changes with GO and bwGO when its concentration has been increased from 0 to 20 μM.

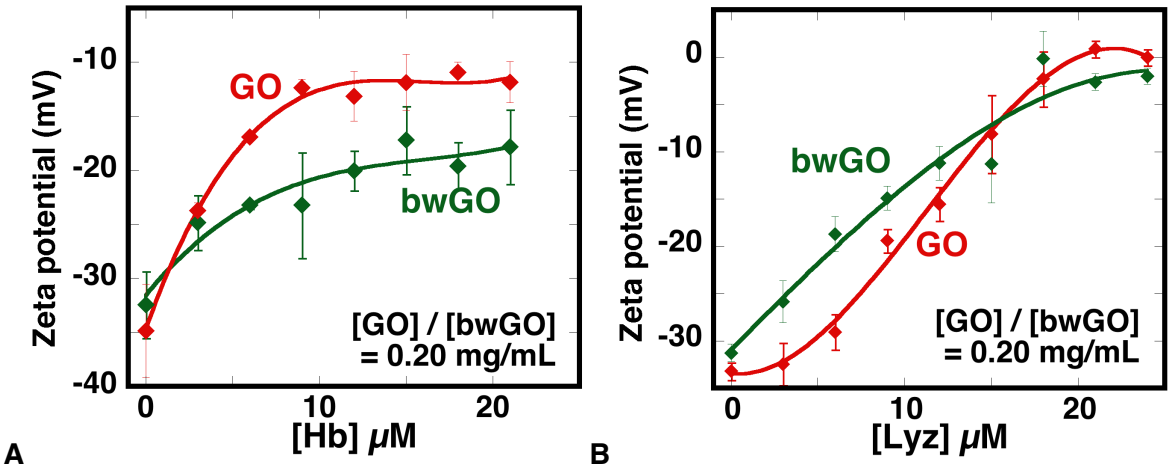

Figure 4.5. Zeta potential titrations of Hb **(A)**, and Lyz **(B)** showed gradual charge neutralization during protein adsorption to GO and bwGO

4.4.4. Protein structure retention and circular dichroism studies. Nano-bio interactions influence bound protein structure, where strong interactions might distort or denature the protein. The extent of secondary structure retention was analyzed by examining the far–UV circular dichroism (CD) spectra of the bound protein. The extent of structure retention is approximated as the ratio of the ellipticity of the bound protein (E_{bound}) to that of the unbound protein ($E_{unbound}$), both measured at 222 nm, where the 222 nm minimum corresponds to the alpha helical content of the protein is estimated as RE@222 = (E_{bound} / $E_{unbound}$). The protein loading was kept at 50% (w/w) where all the proteins showed significant adhesion to the sheets and spectra have been recorded using very short path length cuvettes (0.05 cm). The spectra were corrected for scattering, as reported earlier.[10,25]

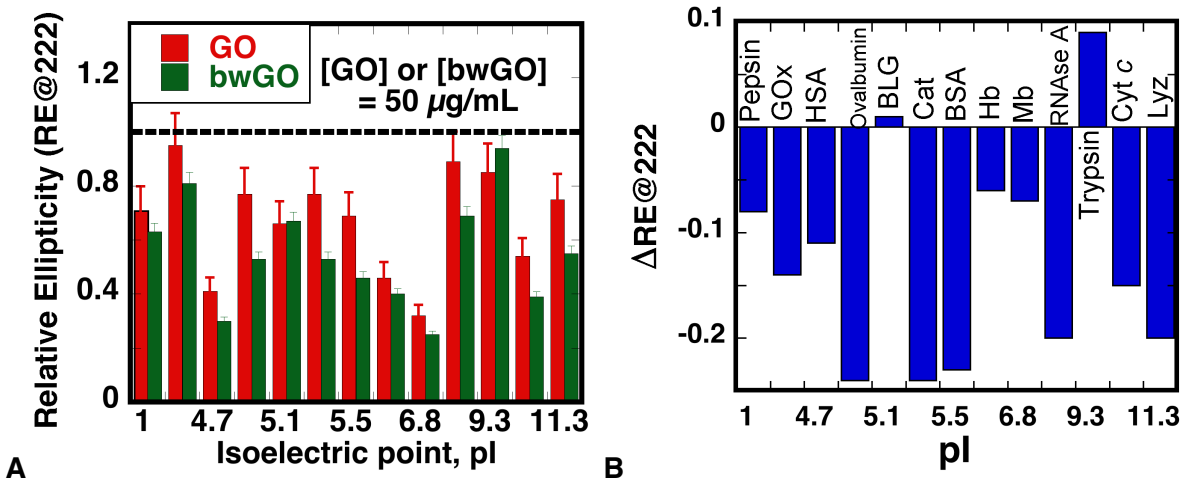

Figure 4.6. A. Plot of the ratios of ellipticities (RE@222) of bound proteins at 222 nm to that of the corresponding unbound protein as a function of protein pI values. Red bars correspond to those bound to GO and green bars correspond to those bound to bwGO. The ratio of 1.0 was taken for that of the unbound protein. **B.** Plot of ΔRE@222 as function of pI, where ΔRE@222= (RE@222 of protein bound to bwGO – RE@222 of the same protein bound to GO).

The ratio of ellipticities at 222 nm of GO-bound protein to that of the unbound protein (RE@222) followed the order GOx (4.6) > RNase (9.3) ≥ Trypsin (9.3) ≥ Ovalbumin (4.9) = Catalase (5.4) > Lyz (11.3) > Pepsin A (1.0) ≥ BSA (5.5) ≥ BLG (5.1) > Cyt *c* (10) > Hb (6.8) > HAS (4.7) > Mb (6.8) (**Figure 4.6.A**). In the case of bwGO, the trend was Trypsin > GOx > RNase ≥ BLG ≥ Pepsin A > Lyz ≥ Ovalbumin = Catalase > BSA > Hb ≥ Cyt *c* > HSA > Mb, but in almost all cases, the extent of structure retention was lower with bwGO than with GO.

A plot of the relative loss of structure when the protein is bound to GO vs bwGO was generated (**Figure 4.6.B**) where the relative loss (ΔRE@222) is defined as RE@222 of a protein bound to bwGO minus the RE@222 of the same protein bound to GO. A positive value of this parameter indicates gain in protein secondary structure while a negative value corresponds to further loss in structure due to base-wash. The data show that maximal loss in structure occurred when the pI of the protein is close to neutral value, or when the protein has ~ -15 charge. This consistent loss in secondary structure could result in decreased enzymatic activities for the bound enzymes, and hence activities of enzymes bound to bwGO were determined and compared with those bound to GO.

4.4.5. Enzymatic activities. The peroxidase like activity of Hb and Mb, oxidase activity of GOx and reductase activity of Cat were assayed before and after binding to GO as well as bwGO, and the data have been compared to deduce the influence of base-wash on the bound enzyme activities. The percent activities of samples bound to GO or bwGO with respect to those of the corresponding unbound proteins (100%) are shown in **Figure 4.7.A**.

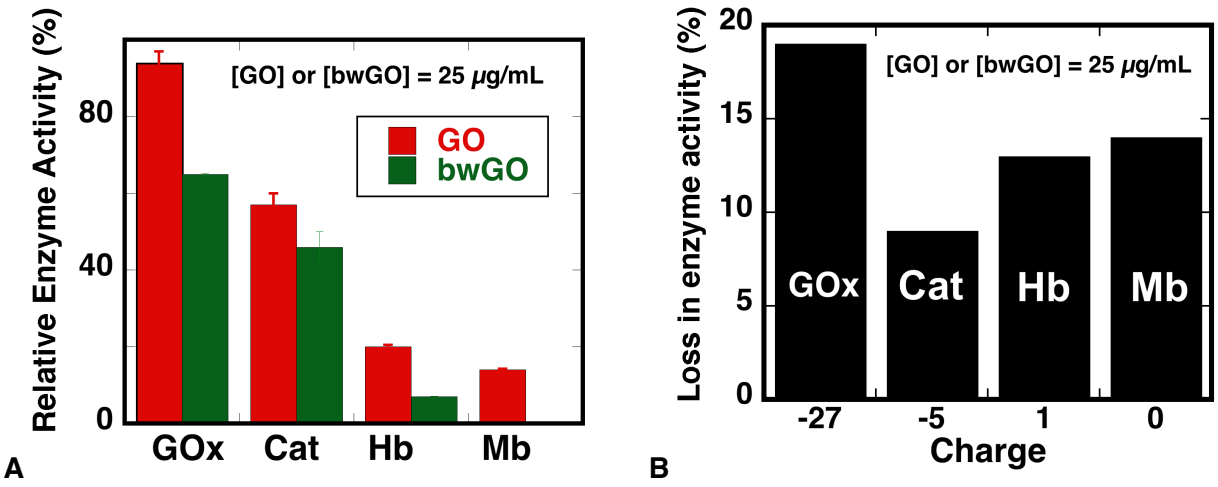

Figure 4.7. A. Relative enzymatic activities of GO/enzyme (red bars), and bwGO/enzyme (green bars). **B.** Plot of activity loss enzymes bound to bwGO vs enzyme charge, which shows lack of correlation between activity loss and enzyme charge.

Oxidase activity of GO/GOx was essentially the same (94%) as that of the pristine GOx, but significant reduction has been noted (65%) in case of bwGO/GOx. Peroxidase-like activity of Hb was only 20% upon binding to GO and it reduced further to 5% on binding to bwGO. Similarly, GO/Mb showed only 14% activity and no measurable activity has been noted for bwGO/Mb. In case of Cat, the activity was reduced to ~60% on binding to GO while the activity of bwGO/Cat has been decreased to 45%.

A plot of loss in activity vs enzyme charge (**Figure 4.7.B**) indicated a poor correlation with charge, which suggests that electrostatic interactions do not control the enzyme activity at this interface. To further test these conclusions, we have examined the influence of these materials on cell growth or cell viability using HEK 293T cells.

4.4.6. Cell toxicity studies. The cytocompatibility of GO, bwGO and OD with HEK 293T cells up to 24 h of co-incubation was evaluated, the data was obtained by (i) measuring intracellular metabolism indicated by spectrophotometric measurement of dehydrogenase activity within the cell and (ii) by observing the extracellular morphology using light microscopy and they showed no appreciable change in cell metabolism with respect to controls. After co-incubation for 24 h, the cells revealed a clear dose-dependent decrease in cell metabolism beyond 75 μg/mL (**Figure 4.8**). At higher loadings, bwGO was slightly more toxic than GO, within our experimental errors but both solids were toxic to the cells.

The above intracellular metabolism results were substantiated by light microscopy images taken at 24 h and 36 h of co-incubation, which revealed significantly stressed cell morphology at the GO and bwGO concentrations beyond 75 μg/mL. Interestingly, at greater than 75 μg/mL, bwGO turned out to be slightly more cytotoxic than GO.

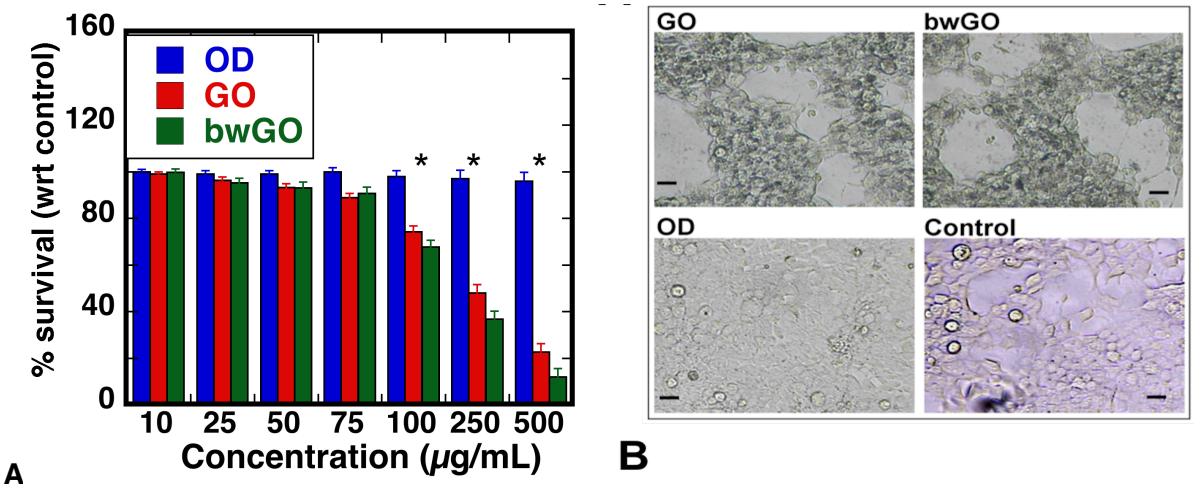

Figure 4.8. Cytotoxicity assays of GO, bwGO and OD when co-incubated with HEK 293T cells for 24 h. **(A)** Survival of the cells in comparison to the control shows that the dose-dependent toxicity of bwGO is higher than that of GO, and OD has no toxic effect. **(B)** Optical microscopy images of HEK 293T cells co-incubated with 500 μg/mL of GO (top, left), bwGO top, right), OD bottom, left) and Control HEK 293 T (bottom, right) for 36 h. Clearly, the cell morphology is affected by the presence of GO and bwGO (500 μg/mL), whereas OD did not affect cell growth. The difference in cell toxicity induced by GO and bwGO was calculated using two-tailed unpaired student's *t* test, found to be statistically significant at concentrations above 75 μg/mL (*$\rho < 0.05$).

We also examined the cells exposed to OD isolated from washing GO, but no morphological or metabolic differences could be observed between cells incubated with OD and control HEK 293T cells. The results obtained from CCK-8 kit, for monitoring intracellular dehydrogenase activity and light microscopy for assessing the cell morphology correlated consistently throughout the trials.

To further investigate the influence of OD on these cells, they were detached and transferred to a six-well plate and monitored for an additional 48 h (this is beyond the first 36 h of co-incubation). By this time cells exposed to the higher doses of GO and bwGO started to die, whereas the control cells and cells exposed to OD were still metabolically active. No appreciable difference in the rate of cell division, morphology or cellular metabolism was observed between OD co-incubated and control cells.

In summary, the binding affinities of several proteins have decreased, and their structure retention and enzymatic activities (when relevant) have also been decreased when the OD has been removed from the GO suspensions. Thus, OD appears to play an important role in shielding these bio-macromolecules from any adverse interactions of the underlying graphitic surface. When the surface is coated with low loadings of BSA (400% (w/w)), the activities of both Hb and Mb have recovered and even exceeded those adsorbed onto GO. Cytotoxicity studies show that these materials are toxic to HEK 293T cells at high concentrations (>75 μg/ml) and long exposure times (>24 h).

4.5. Discussion

Biohybrid materials that are made of biomolecules and carbon based nanomaterials (such as carbon nanotubes and GO) are thought to offer superior (or improved) biocompatibility, sustainability and biodegradability over inorganic (nano)materials.[17, 26] GO, a water dispersible graphene derivative, is one of the promising candidates for rapidly growing biomaterials research.[1] Recently, the presence of oxidative debris within GO suspensions was detected,[12] which showed significant influence on the material properties of GO.[16, 15, 27, 28] However, the effect of OD on protein-GO interactions has not been evaluated yet. Here, we have studied the effect of OD in controlling the bound protein characteristics as well as the role of OD in its cytotoxicity to HEK 293T cell lines.

Adsorption of proteins to both GO and bwGO are marginally different when evaluated against a small set of 13 proteins whose pI values ranged from 4 to 12. The maximum loading observed for Hb (pI 6.8) with GO was 320% (w/w), and this translates into an average of ~ 1.3 layers of Hb on the nanosheets, if we assume that the protein occupies the entire surface (7.05 x 10^{-22} $Å^2$/g) and that the diameter the protein is unchanged upon binding to the nanosheets. Along these lines, Hb binding to bwGO saturated around an average of 0.7 layers, much less than that observed with GO. This decrease in the coverage could be due to at least two possible factors, 1) decrease in intrinsic affinity of Hb to bwGO, or 2) loss in the secondary structure of bound Hb such that it occupies a larger area on the nanosheets. In support of the former, the Hb binding affinity of Hb decreased 10-fold, from GO to bwGO. On the other hand, the CD data analysis indicated only 10% loss in the CD band intensities for Hb bound to bwGO when compared to that bound to GO. Therefore, the decrease in the maximum loading of Hb is more likely due to reduced affinity.

Similar analysis of the CD data of Lyz (ΔRE@222 = -18%), GOx (ΔRE@222 = -14%) and BSA (ΔRE@222 = -23%) also indicates that protein denaturation is not directly controlling the loading maxima. Therefore, the changes in interactions at bwGO vs GO could be responsible for the differences in affinities.

The function of biohybrids can be quite sensitive to the conformation of the bound protein.[29, 30] Current studies involving 13 different proteins revealed that there has been a small but consistent increased loss in protein structure with bwGO when compared to the proteins bound to GO. To further understand the basis for increased protein structure loss on bwGO, we examined if there is any correlation between structure loss and protein charge or the hydropathy index of the protein. The average hydropathy index[31] was calculated using Expasy Protparam tool and it indicated the order Cyt c > RNase A > Catalase > BSA = Lyz > HSA = Mb > GOx > BLG > Trypsin > Ovalbumin > Hb > Pepsin A, but this trend has no correlation with the observed trends in RE@222 or ΔRE@222 of these proteins bound to bwGO.

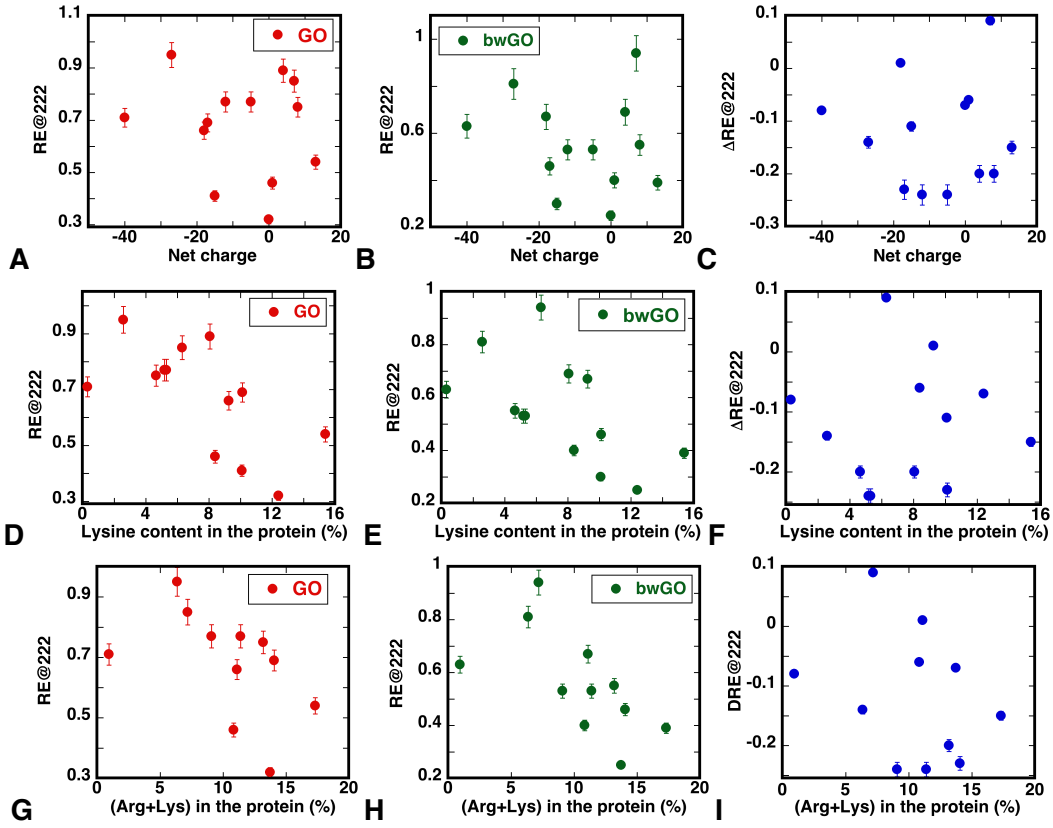

Figure 4.9. Net charge of the protein at pH 7.0 is not correlated with relative loss of ellipticity at 222 nm (RE@222), after binding to GO **(A)** and bwGO **(B).** The differences in ellipticity retention of bwGO to GO (ΔRE@222) is shown in **(C).** Lysine content in the protein (%) vs RE@222 observed after binding to GO **(D)** and bwGO **(E). (F)** ΔRE@222 as a function of lysines. Sum of lysines and arginines in the protein as a function of RE@222 after binding to GO **(G)** and bwGO **(H). (I)** ΔRE@222 vs total number of arginines and lysines combined. No noticeable trend is shown in all cases.

The relative loss of ellipticity at 222 nm (ΔRE@222), which is a measure of the percent structure retention when compared to that of the unbound protein, did not correlate with net charge on the protein (**Figure 4.9.A-C**), or the lysine content of the protein (**Figure 4.9.D-F**) or the sum of the number of lysine and arginine residues present in the protein (**Figure 4.9.G-I**).

On the other hand, the differences in the extents of structure loss when proteins bind to bwGO vs GO (ΔRE@222), however, depended on the percentage arginine content of the protein as well as the aliphatic index of the protein (**Figure 4.10.B**). Twelve proteins containing Arg contents of 0-7% showed strong correlation with the extent of structure loss (**Figure 4.10.A**), irrespective of their net charge. This strong trend shows the critical role of Arg residues in the interactions with bwGO. Arg was suggested to interact strongly with GO because of its ability to form hydrogen bonds as well as its charge and hydration status.[32,33,34] Lyz with 8% Arg content deviated significantly from the plot and could be due to its unusually high thermodynamic stability.[35] In a recent study, strong interaction of lysozyme, an arg rich protein, with carbon nanotubes (CNT) was demonstrated,[36] and the binding free energy (ΔG_{bind}) between strongly interacting Args in Lyz with CNT was -5.9 kcal/mol, higher than that of lysine (-3.5 kcal/mol).[37]

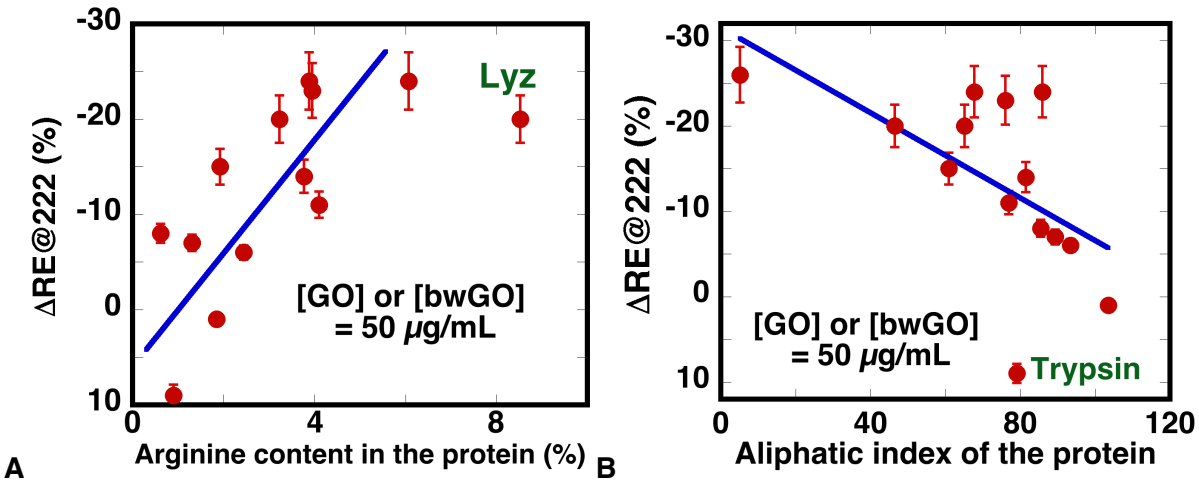

Figure 4.10. A. Correlation of the differential loss of ellipticities of GO and bwGO (ΔRE@222) with the protein arginine content. **B.** Plot of ΔRE@222 vs average volume occupied by aliphatic side chains of the protein, which was calculated using Expasy Protparam using the structures from the PDB.

Interaction of nanosurface with the amino acid side chains after base wash would influence the conformation bound proteins to GO.[5] The possible role of hydrophobic residues in distorting the structure of the bound protein (between bwGO and GO) is examined in **Figure 4.10.B**. The plot of extent of relative structure loss (ΔRE@222) as a function of the average aliphatic index showed a strong correlation. Aliphatic index is the volume occupied by the side chains of aliphatic amino acids (alanine, valine, isoleucine, and leucine) of the protein. There has been a greater retention of protein secondary structure with increasing aliphatic index. Base washing had less and less influence as the aliphatic index increased. That is, more hydrophobic proteins did not distinguish between bwGO and GO while less hydrophobic proteins are more sensitive to exposure to the hydrophobic surfaces of bwGO. Thus, the role of OD in these interactions depends also on the aliphatic index of the protein. In addition, the interaction of bwGO with biomolecules is primarily hydrophobic, along with weak electrostatic interactions with surface functional groups.

Enzymatic activities of the proteins after bound to GO and bwGO was another tool used to compare the effect of OD at this interface. In support with our secondary structure studies, proteins showed decrease in activities when bound to bwGO vs GO **Figure 4.7.A**. Peroxidase like activity of Hb and Mb, Reductase activity of Cat and, Oxidase activity of GOx composites were decreased at both interfaces and no correlation with charge was noted. Thus hydrophobic interaction resulted in structure denaturation resulted in loss in activity. Here, as a result of unfavorable surface interactions with bwGO, most of the enzymes under the study loss its activity which showed strong correlation with loss in structure.

Further insight into the protein-GO interactions was evident when relative activities of the bound proteins are compared with their corresponding extents of secondary structure retention.

Here we observed a linear relation with secondary structure and enzymatic activity for different proteins (Hb, Mb, Cat and GOx, **Figure 4.11**). Evidently, structural denaturation is the primary reason for decrease in activity of the proteins as the debris has been removed. This might seem trivial as structure retention is essential for activities but it has been noted that GO inhibited the activity of chymotrypsin[38] whereas it increased the activity of oxalate oxidase, esterase[5] and cytochrome *c.*[10]

Since loss in activity is highly undesirable, we tested if the hydrophobic surfaces of bwGO could be passified by the adsorption of cationized BSA prior to enzyme loading.[10] BSA was chemically modified with the polyamine, tetraethelenepentamine (TEPA), resulted in a charge reversal from -20 to +23, confirmed by agarose gel electrophoresis. The bwGO surface (0.2mg/mL) was passivated using cationized BSA (400% w/w) and, Hb (8 μM), Mb (12 μM), Cat (0.8 μM) and GOx (4μM) were loaded prior to the activity assays. Activities of the above enzymes bound to cationized BSA-loaded bwGO (bio-bwGO) is compared with bwGO, under similar binding conditions, is given in **Figure 4.11.B**. Surprisingly, the activities of Hb and Mb bound to bio-bwGO exhibited substantial improvement (**Figure 4.11.B**, blue bars) while that of Cat showed no change. Thus, the novel biofunctionalization strategy[10] can be successfully used to passify bwGO as well.

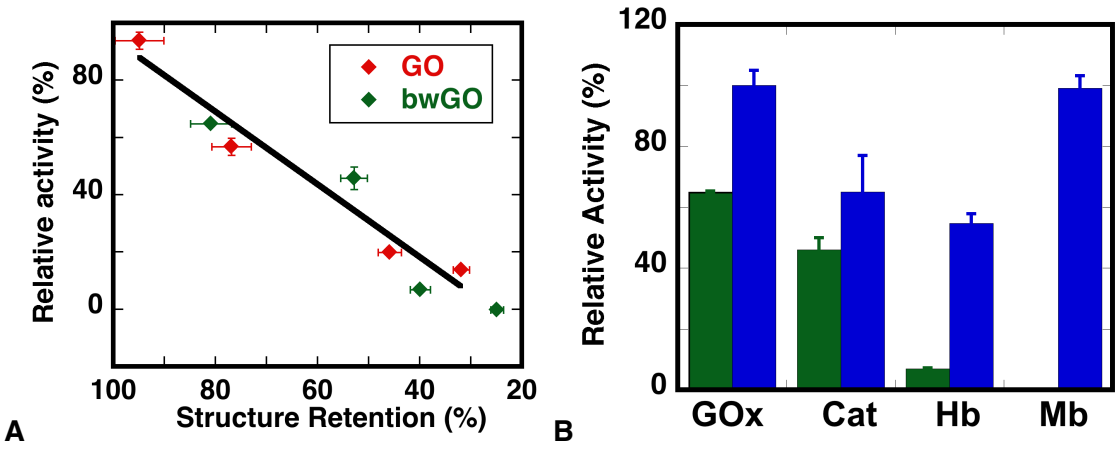

Figure 4.11. **A.** Strong correlation of relative activities of GOx, Cat, Hb and Mb bound to GO or to bwGO with the extents of their corresponding secondary structure retention. **B.** Blue bars correspond to bwGO samples that were biophilized with cationized BSA (bio-bwGO/enzyme) before enzyme loading.

Finally, the cell survival studies show that OD affects the interaction of GO with 293T cells. Incubation for 24 h, both GO and bwGO showed appreciable cytotoxicity above 75 μg/mL concentration (**Figure 4.8**). The dose dependent cytotoxicity of GO beyond 75 μg/mL concentration is in agreement with the previously published results.[23] However, to our knowledge, there is no study that reported the biocompatibility of bwGO with human cell lines. Chemically reduced GO, in comparison to GO or bwGO, was much more toxic.[39] There has been no toxicity for OD, even at very high doses (500 μg/mL), which indicates that any toxic effect of GO is intrinsic to it and not due to OD.

4.6. Conclusions

The oxidative debris, a by-product of graphene oxide synthesis by any oxidation method[40] was illustrated to affect various mechanical, and optical properties of GO at various levels. This debris can be separated from GO by washing with any base and the resulted sheets are called base washed GO (bwGO). Our current study focused on the role of OD in governing the behaviour of proteins at GO surfaces. Analysis with 13 different proteins of variable molecular and biological properties revealed that the interactions are more specific to the protein used. Arginine and aliphatic residues of the proteins controlled the mode of interactions at GO and bwGO surfaces, indicating the role of hydrogen bonding, electrostatic and hydrophobic interactions at this interface. The mode of interactions played a major role in determining the protein secondary structure and thereby dictating the enzymatic activities, which is crucial for GO based bio-devices. The present study makes some progress in the fundamental understanding of protein behaviour at graphitic surfaces and the importance of OD in interpreting protein-GO interactions.

4.7. References

1. Chung, C.; Kim, Y. K.; Shin, D.; Ryoo, S. R.; Hong, B. H.; and Min, D. H.; Biomedical Applications of Graphene and Graphene Oxide, *Acc. Chem. Res.*, **2013**, *46*, 2211-2224.

2. Deshapriya, I. K.; and Kumar, C.V., Nanobio interfaces: charge control of enzyme/inorganic interfaces for advanced biocatalysis, *Langmuir*, **2013**, *29*, 14001-14016.

3. Huang, R.; Carney, R. P.; Ikuma, K.; Stellacci, F. and Lau, B. L. T., Effects of surface compositional and structural heterogeneity on nanoparticle–protein interactions: different protein configurations, *ACS Nano*, **2014**, *8*, 5402-5412.

4. Zhang, Y.; Wu, C.; Guo, S.; and Zhang, J., Interactions of graphene and graphene oxide with proteins and peptides, *Nanotechnol. Rev.*, 2013, vol. 2, p. 27.

5. Zhang, Y.; Zhang, J.; Huang, X., Zhou, X.; Wu, H. and Guo, S., Assembly of graphene oxide–enzyme conjugates through hydrophobic interaction, *Small*, **2012**, *8*, 154-159.

6. Zhang, J.; Zhang, F.; Yang, H.; Huang, X.; Liu, H.; Zhang, J.; and Guo, S., Graphene oxide as a matrix for enzyme immobilization, *Langmuir*, **2010**, *26*, 6083-6085.

7. Chou, S. S.; De, M.; Luo, J.; Rotello, V. M.; Huang, J.; and Dravid, V. P., Nanoscale graphene oxide (nGO) as artificial receptors: implications for biomolecular interactions and sensing, *J. Am. Chem. Soc.*, **2012**, *134*, 16725-16733.

8. Pavlidis, I.; Vorhaben, T.; Gournis, D.; Papadopoulos, G.; Bornscheuer, U.; and Stamatis, H., Regulation of catalytic behaviour of hydrolases through interactions with functionalized carbon-based nanomaterials, *J. Nanopart. Res.*, **2012**, *14*, 1-10.

9. Mu, Q.; Su, G.; Li, L.; Gilbertson, B. O.; Yu, L. H.; Zhang, Q.; Sun Y. P.; and Yan, B., Size-dependent cell uptake of protein-coated graphene oxide nanosheets, *J. Appl. Mater. Interfaces*, **2012**, *4*, 2259-2266.

10. Pattammattel, A.; Puglia, M.; Chakraborty, S.; Deshapriya, I. K.; Dutta, P. K.; and Kumar, C. V.; Tuning the activities and structures of enzymes bound to graphene oxide with a protein glue, *Langmuir*, **2013**, *29*, 15643-15654.

11. Jin, L.; Yang, K.; Yao, K.; Zhang, S.; Tao, H.; Lee, S. T.; Liu, Z.; and Peng, R., Functionalized graphene oxide in enzyme engineering: a selective modulator for enzyme activity and thermostability, *ACS Nano*, **2012**, *6*, 4864-4875.

12. Rourke, J. P.; Pandey, P. A.; Moore, J. J.; Bates, M.; Kinloch, I. A.; Young, R. J.; and Wilson, N. R.; The real graphene oxide revealed: stripping the oxidative debris from the graphene-like sheets, *Angew. Chem. Int. Ed.*, **2011**, *50*, 3173-3177.

13. Diederix, R. E. M.; Ubbink, M.; and Canters, G. W., Effect of the protein matrix of cytochrome c in suppressing the inherent peroxidase activity of its heme prosthetic group, *ChemBioChem*, **2002**, *3*, 110-112.

14. Bonanni, A.; Ambrosi, A.; Chua, C. K.; and Pumera, M., Oxidation debris in graphene oxide is responsible for its inherent electroactivity, *ACS Nano*, **2014**, *8*, 4197-4204.

15. Coluci, V. R.; Martinez, D. S. T.; Honório, J. G.; de Faria, A. F.; Morales, D. A.; Skaf, M. S.; Alves, O. L.; and G. A., Umbuzeiro, Noncovalent interaction with graphene oxide: the crucial role of oxidative debris, *J. Phys. Chem. C*, **2014**, *118*, 2187-2193.

16. Thomas, H. R.; Valles, C.; Young, R. J.; Kinloch, I. A.; Wilson, N. R.; and Rourke, J. P., Identifying the fluorescence of graphene oxide, *J. Mater. Chem. C*, **2013**, *1*, 338-342.

17. Yang, K.; Feng, L.; Shi, X.; and Liu, Z., Nano-graphene in biomedicine: theranostic applications, *Chem. Soc. Rev.*, **2013**, *42*, 530-547.

18. Hummers, W. S.; and Offeman, R. E., Preparation of graphitic oxide, *J. Am. Chem. Soc.*, **1958**, *80*, 1339-1339.

19. Du, P.; Zhao, J.; Mashayekhi, H.; Xing, B. Adsorption of bovine serum albumin and lysozyme on functionalized carbon nanotubes, *J. Phys. Chem. C,* **2014,** *118*, 22249-22257.

20. Pütter, J., Peroxidases. In *Methods of Enzymatic Analysis (Second Edition)*; Hans, U. B., Ed.; Academic Press, 1974; pp 685-690.

21. Beers, R. F.; Sizer, I. W. *J.* A spectrophotometric method for measuring the breakdown of hydrogen peroxide by catalase, *Bio. Chem.* **1952**, *195*, 133-140.

22. Gibson, Q. H.; Swoboda, B. E. P.; Massey, V.: Kinetics and Mechanism of Action of Glucose Oxidase. *J. Biol. Chem.* **1964**, *239*, 3927-3934.

23. Liu, Y.; Luo, Y.; Wu, J.; Wang, Y.; Yang, X.; Yang, R.; Wang, B.; Yang, J.; Zhang, N.: Graphene oxide can induce in vitro and in vivo mutagenesis. *Sci. Rep.* **2013**, *3*.

24. Chang, Y.; Yang, S.-T.; Liu, J.-H.; Dong, E.; Wang, Y.; Cao, A.; Liu, Y.; Wang, H.: In vitro toxicity evaluation of graphene oxide on A549 cells. *Toxicol. Lett.* **2011**, *200*, 201-210.

25. Kumar, C. V.; Chaudhari, A.: Proteins Immobilized at the Galleries of Layered α-Zirconium Phosphate: Structure and Activity Studies. *J. Am. Chem. Soc.* **2000**, *122*, 830-837.

26. Titirici, M.-M.; White, R. J.; Brun, N.; Budarin, V. L.; Su, D. S.; del Monte, F.; Clark, J. H.; MacLachlan, M. J.: Sustainable carbon materials. *Chem. Soc. Rev.,* **2015**, *44*, 250-290.

27. M. R. Eftink and C. A. Ghiron, Fluorescence quenching studies with proteins, *Anal. Biochem.*, **1981**, *114*, 199-227.

28. López-Díaz, D.; Mercedes Velázquez, M.; Blanco de La Torre, S.; Pérez-Pisonero, A.; Trujillano, R.; Fierro, J. L. G.; Claramunt, S.; and Cirera, A., The role of oxidative debris on graphene oxide films, *ChemPhysChem*, **2013**, *14*, 4002-4009.

29. Ding, Z.; Ma, H.; and Chen, Y., The role of oxidative debris on graphene oxide films, *RSC Adv.,* **2014**, *4*, 55290-55295.

30. Zeng, Q.; Cheng, J.; Tang, L.; Liu, X.; Liu, Y.; Li, J.; and Jiang, J., Self-Assembled Graphene–Enzyme Hierarchical Nanostructures for Electrochemical Biosensing, *Adv. Funct. Mater.*, **2010**, *20*, 3366-3372.

31. Kyte, J.; Doolittle, R. F.: A simple method for displaying the hydropathic character of a protein. *J. Mol. Biol.* **1982**, *157*, 105-132.

32. Jain, P.; Soshee, A.; Narayanan, S. S.; Sharma, J.; Girard, C.; Dujardin, E.; Nizak, C.: Selection of Arginine-Rich Anti-Gold Antibodies Engineered for Plasmonic Colloid Self-Assembly. *J. Phys. Chem. C,* **2014**, *118*, 14502-14510.

33. Sultan, A. M.; Hughes, Z. E.; Walsh, T. R.: Binding Affinities of Amino Acid Analogues at the Charged Aqueous Titania Interface: Implications for Titania-Binding Peptides. *Langmuir,* **2014**, *30*, 13321-13329.

34. Ahn, H.; Kim, T.; Choi, H.; Yoon, C.; Um, K.; Nam, J.; Ahn, K. H.; and Lee, K., Gelation of graphene oxides induced by different types of amino acids, *Carbon*, **2014**, 71, 229-237.

35. Ahmad, F.; and Bigelow, C. C., Estimation of the free energy of stabilization of ribonuclease A, lysozyme, alpha-lactalbumin, and myoglobin, *J. Biol. Chem.*, **1982**, 257, 12935-12938.

36. Wu, E.; Coppens, M.-O.; Garde, S., Role of Arginine in Mediating Protein–Carbon Nanotube Interactions. *Langmuir,* **2015,** *31*, 1683-1692.

37. Calvaresi, M.; Hoefinger, S.; Zerbetto, F., Probing the Structure of Lysozyme–Carbon-Nanotube Hybrids with Molecular Dynamics. *Chemistry – A European Journal* **2012,** *18*, 4308-4313.

38. De, M.; Chou, S. S.; and Dravid, V. P., Graphene oxide as an enzyme inhibitor: modulation of activity of α-chymotrypsin, *J. Am. Chem. Soc.*, **2011**, *133*, 17524-17527.

39. Bianco, A., Graphene: safe or toxic? The two faces of the medal, *Angew. Chem. Int. Ed.*, **2013**, *52*, 4986-4997.

40. Rodriguez-Pastor, I.; Ramos-Fernandez, G.; Varela-Rizo, H.; Terrones, M.; and Martin-Gullon, I., Towards the understanding of the graphene oxide structure: How to control the formation of humic-and fulvic-like oxidized debris, *Carbon*, **2015**, *84*, 299-309.

***

Biographene: Direct Exfoliation of Graphite to Pristine Graphene using Proteins

5.1. Abstract

A high yielding aqueous phase exfoliation of graphite crystals to high quality graphene using edible proteins and kitchen chemistry is reported here. Bovine serum albumin (BSA), β-lactoglobulin, Ovalbumin, Lysozyme and Hemoglobin were used to exfoliate graphite and the exfoliation efficiency depended on the sign and magnitude of the surface charge the protein. BSA, which showed maximum exfoliation rate facilitated graphite exfoliation in water, at room temperature, by turbulence/shear force generated in an ordinary kitchen blender at rates exceeding 4 mg mL^{-1} h^{-1}. Raman spectroscopic analysis and TEM indicated the presence of 3-5 layer, unoxidized graphene with ~0.5 μm size sheets. When the dispersions were loaded on a cellulose paper (650 μg cm^{-2}), the film conductivity was measured to be 32000 S m^{-1}, which is much higher than graphene/polymer composites. Our method yielded ~7 mg mL^{-1}, stable, pristine graphene dispersions from cheap and sustainable resources and common apparatus which was stable under wide ranges of pH (3.0-11) and temperature (5.0-50°C), and in fetal serum for more than a month. Current approach gave higher rates of biofunctionalized graphene (biographene) with a controllable

surface charge, in better yields than other methods. These findings might lead to large scale production of graphene for biological applications.

5.2. Introduction

A facile route for the large scale production of water dispersible, few layer graphene (FLG) by shear exfoliation of graphite using inexpensive, edible proteins is reported. Applications of graphene in the biomedical and healthcare sectors require hydrophilic and biocompatible graphene derivatives.[1] Graphene oxide (GO) is often used as a precursor of graphene, but its potential is limited by oxidative defects and toxic metallic impurities introduced during the synthesis and exfoliation process.[2] Although, the successful exfoliation of graphite to pristine graphene using organic solvents,[3,4] ionic liquids[5,6] or surfactants[7] has been reported, the biocompatibility of the resulting product, quality, expense, and environmental impact of the production methods still remain unaddressed.[8]

Ultrasonication was used to exfoliate graphene with biological agents such as bovine serum albumin (BSA).[9,10,11] These proteins are suggested to adsorb to graphite platelets and facilitate delamination upon ultrasonication.[9,10,11] The adsorbed protein might inhibit restacking of the graphene sheets and could contribute to nanoplate stability.[11] However, sonication was suggested to introduce oxidative defects (O - 10-25%),[12] scalability of this process is particularly challenging and only low exfoliation rates have been reported (< 1 mg $mL^{-1}h^{-1}$).[13]

Recently, shear force/turbulence methods were used in a kitchen blender for the mechanical exfoliation of graphite at rapid exfoliation rates.[13,14,15] This method offers low oxidative damage (O > 5%)[15] when compared to the sonication method (O - 10-25%).[12] This approach was mainly used with organic solvents, N-methyl pyrolidine (NMP),[13] Dimethyl formamide (DMF),[15] and some surfactants.[14] The shear produced and the turbulent flow exceeds the critical Reynold's number required for delamination (10^4),[15] and even a simple kitchen blender was shown to be a feasible apparatus for graphene production.[14,15]

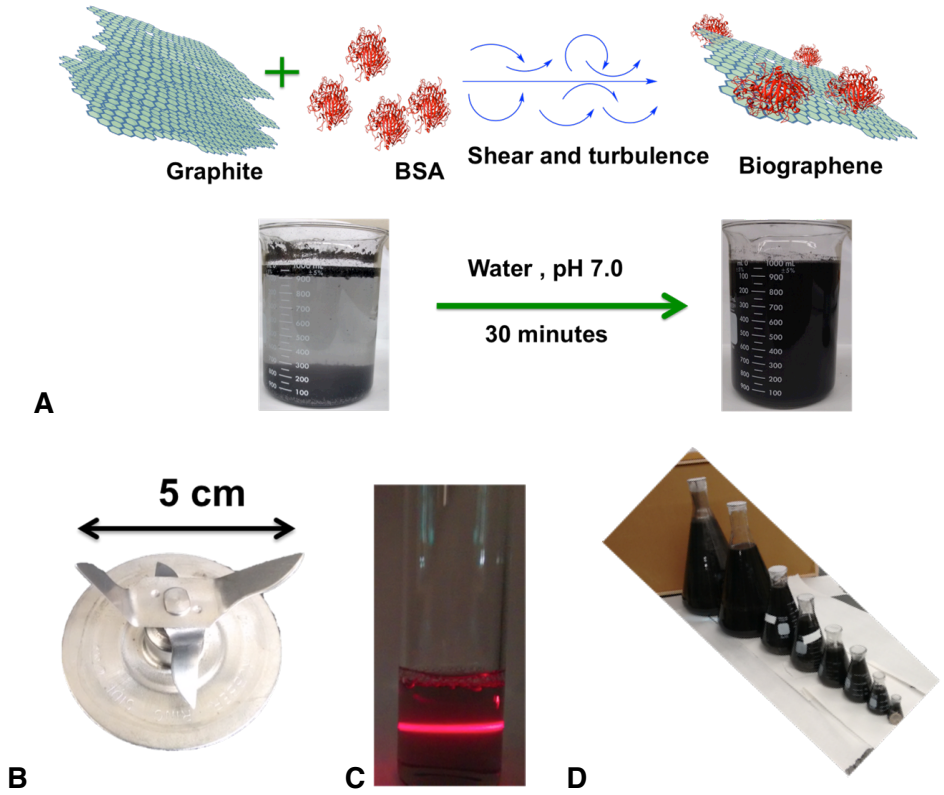

Scheme 5.1. A. Shear exfoliation of graphite using bovine serum albumin (BSA) in water at pH 7.0. **B**. Type of blades used to generate the turbulence and shear. **C.** Visualization of graphene formation by laser light scattering. **D**. Scalability of the method is demonstrated where the largest conical flask is 8 L.

Herein, we report shear-exfoliation of graphite in a kitchen blender with edible proteins to produce high concentrations of nearly defect-free graphene aqueous dispersions in less than an hour (**Scheme 5.1**). By combining the advantages of the protein's characteristics as an exfoliating/stabilizing agent for graphene and the feasibility of the shear exfoliation, high quality graphene is produced rapidly. The proteins we tested for exfoliation efficiency includes, bovine serum albumin (BSA), β-lactoglobulin, ovalbumin, lysozyme and hemoglobin, which are inexpensive, edible proteins, and they are either waste products form the meat industry or from egg and milk.[16] The surface charge of the protein played a critical role in the exfoliation and stabilization of graphene dispersions. Our protein based shear/turbulence exfoliation is favorable over sonication or organic solvent methods in terms of yield, quality and water dispersion properties. Our results are described below.

5.3. Materials and Methods

5.3.1. Materials. Graphite crystals (~150 μm), Lysozyme (egg white), β-lactoglobulin (Bovine milk), Trypsin (Bovine) and Ovalbumin (egg white) were obtained from Sigma Aldrich (St. Louis, MO). BSA and Hemoglobin was purchased from Equitech-Bio Inc. (Kerrville, TX). All the proteins were used without further purification. Oster® Kitchen 10 speed blender was purchased from a local shop.

5.3.2. Exfoliation of Graphite. All the exfoliation experiments were performed by adding calculated amounts of graphite, BSA, DI water in the kitchen blender at required blade speed. Aliquots (1 mL) of the mixture were taken every 5 minutes to quantify the progress of exfoliation. Samples were centrifuged at 1500 rpm for 45 minutes to separate unexfoliated graphite particles, and the amount of graphene in the supernatant was measured using extinction at 660 nm, using the calculated extinction coefficient of 398 mL mg^{-1} m^{-1} (**Figure 5.1**). The extinction coefficient of graphene is highly dependent of the size, number of layers and functionalization present. This extinction coefficient was close to that of polysaccharide modified graphene.[26] Rate of exfoliation at different conditions of concentrations, blade speed, pH and volume were calculated by following the exfoliation for first 20 minutes. All the experiments are performed in three trials, except for the optimization of the volume

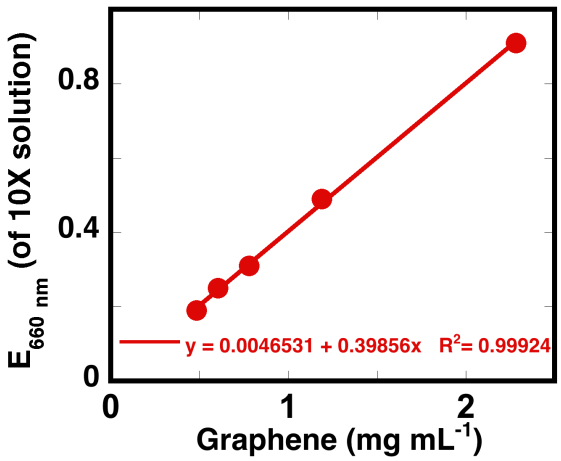

Figure 5.1. The calibration plot used to calculate the extinction coefficient (660 nm) of the biofunctionalized graphene at pH 7.0 in deionized water. All measurements are performed in triplicates and the error bars are smaller to be visible.

5.3.3. Raman Spectroscopy. Raman spectra were recorded using a 514 nm laser in Renishaw system 2000 microscope at 1 μm spatial resolution. The microscope was calibrated using typical Raman shift of Si-wafer sample at 521 cm^{-1}. Graphene samples were concentrated using centrifugation to 1 mg mL^{-1} and were dried on a Si/SiO_2 glass with ~1 cm spot size. We observed sample destruction at 100% focused laser, probably due to the protein, so the beam was off focused by 50% during the measurement. The statistical analysis of number of layers ($<N_G>$) from different Raman spectra was calculated using the following equation,

$$< N_G > = 10^{0.84M+0.45M^2}, \qquad M = \frac{I_{G'ene}(\omega=\omega_{p,G'ite})/I_{G'ene}(\omega=\omega_{s,G'ite})}{I_{G'}(\omega=\omega_{p,G'ite})/I_{G'}(\omega=\omega_{s,G'ite})} \qquad (5.1)$$

where ω_p is the 2D peak intensity and ω_s is intensity of the shoulder ($\omega_s = \omega_p$–30 cm^{-1}). The lateral size <L> of the graphene sheets was calculated using the following empirical relation

$$< L > = \frac{k}{(I_D/I_G)_{G'ene} - (I_D/I_G)_{G'ite}} \qquad (5.2)$$

where k = 0.17-experimentally calculated by comparing Raman intensities with microscopy data, and I_D/I_G is the ratio of D and G band intensities[13]

5.3.4. Microscopy studies. TEM studies were done in a FEI Tecnai T12 using 100 kV accelerating voltage. Graphene samples (20 μg mL^{-1}) were drop casted on a Cu-grid and dried under vacuum, prior to the imaging. SEM images of graphite and graphene coated paper were taken in a JEOL FESM 6335 using 5 kV accelerating voltage. Samples were coated with Au-Pd in Edwards E306A Coating System and directly taken for imaging.

5.3.5. Conductivity Measurements. Graphene suspension (4 mg mL^{-1}) was simply coated on a standard printer paper and air dried to prepare conductive graphene papers. About 200 mg of graphene was adsorbed onto a 22 cm x 14 cm size paper to give 650 μg cm^{-2} loading. Sheet conductivity of the paper was measured using a 4-probe measurement in a Keithley

2420 Sourcemeter®, after making the contacts with Cu-tape. The I-V curve directly obtained from the instrument was used to find the resistance and the sheet resistance was calculated using the following formula,[22] where *R* is the resistance, *ρ* is the resistivity, *L* is the length, *W* is the width and *t* is the film thickness measured from SEM image.

$$R = \rho \frac{L}{Wt} \quad (5.3)$$

5.3.6. Zeta Potential Measurements. Aqueous graphene dispersions (1.6 mL, 0.6 mg mL^{-1}) with known pH were analyzed using the Brookhaven Zeta Plus zeta potential analyzer (Holtsville, NY). The samples were analyzed for electrophoretic mobility using laser Doppler velocimetry and, Smoluchowski fit was used to calculate the zeta potential.

5.4. Results

A facile method for producing unoxidized, pristine graphene under biologically benign conditions is essential for widespread biomedical applications of graphene. Rate of exfoliation, scalability, high quality, controlled functionalization, size and large flake size are highly desired. Rapid production of biofunctionalized, micron size, and defect free, few layer graphene (FLG) is reported here. Further, we have systematically examined particular experimental variables on the exfoliation process. Our data show that protein charge, both magnitude and sign, are critical for efficient exfoliation of graphite. The samples are extensively characterized and have record high conductance and stability in aqueous media.

5.4.1. Graphite exfoliation with protein solutions. A suspension of graphite crystals ([Graphite] = 100 mg mL^{-1}) in 200 mL deionized (DI) water at pH 7.0 containing the protein (3.0 mg mL^{-1}) was subjected to shear in a kitchen blender for 30 minutes. Samples were taken every five minutes to examine the rate of exfoliation and blending was stopped to avoid overheating (< 30°C). The extinction at 660 nm (E_{660}) of the suspension was used to quantify the graphene concentrations, after removing the unexfoliated graphite separated by centrifugation at 1500 rpm for 45 minutes. The extinction coefficient of BSA modified graphene was 398 mL mg^{-1} m^{-1} which was calculated using the calibration plot (**Figure 5.1**).

5.4.2. Effect of the nature of the protein on exfoliation. The proteins used in this study to exfoliate graphite were cheap and found in food sources to ensure the biocompatibility of the produced graphene. BSA (bovine serum), β-lactoglobulin (bovine milk), Lysozyme (egg white), Ovalbumin (egg white), and Hemoglobin (bovine blood) were used to prove the hypothesis that proteins are effective tools for biological production of graphene in water. Four of these five proteins exfoliated graphite, but the exfoliation efficiency strongly depended on protein charge with BSA giving the highest efficiency (**Figure 5.2**). Graphene

production is directly correlated with the extent of negative charge of the protein used. Therefore, we choose BSA as the model system and systematically evaluated how particular experimental parameters influence the exfoliation rate.

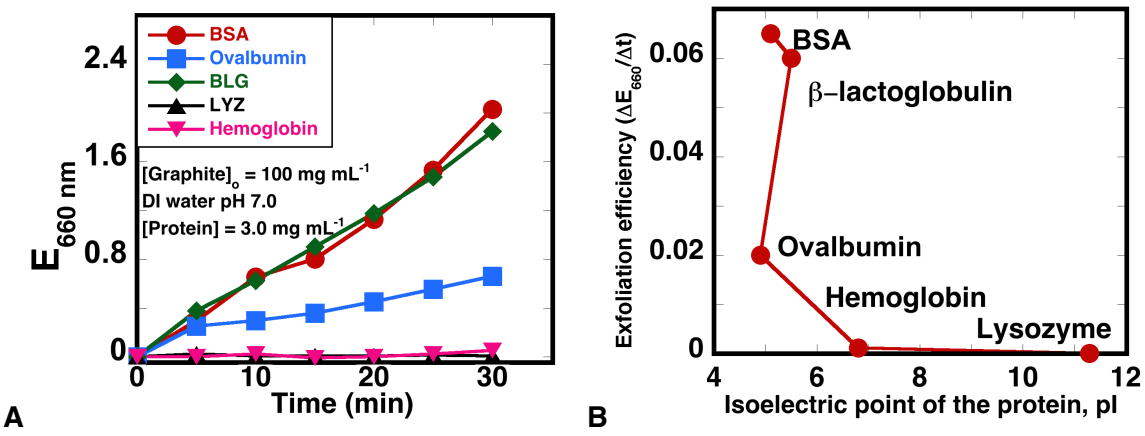

Figure 5.2. Plot showing the efficiency of proteins to exfoliate graphite at neutral pH is correlated with the isoelectric points (pI) of the proteins. **B.** Kinetic plot showing the progress of exfoliation over time using different proteins as stabilizing agents in water.

5.4.3. BSA concentration dependence. The rate of graphene production (mg h^{-1}), at constant blade speed of 17 krpm, is plotted against $[BSA]_o$ in **Figure 5.3.A**. As the $[BSA]_o$ increased from 0.50 mg mL^{-1} to 3.0 mg mL^{-1} and an increase in rate was observed from 400 to 725 mg h^{-1} which corresponds to ~4 mg mL^{-1} h^{-1} rate of exfoliation. Above 3.0 mg mL^{-1} [BSA], no significant increase in exfoliation rate was observed and this concentration was used to optimize the graphite concentration for exfoliation.

5.4.4. Effect of Graphite concentration. The graphite concentration was suggested to affect graphene production rate, due to collisions between the crystallites which can assist in exfoliation. Experiments, therefore, were conducted using 20, 40, 60, 80 and 100 mg mL^{-1} $[Graphite]_o$ and fixed $[BSA]_o$ (3.0 mg mL^{-1}) in 200 mL DI water at pH 7.0. Exfoliation rate at 17 krpm blade speed was linearly correlated with exfoliation rate as shown in **Figure 5.3.B**. The slope of the line displays an increase in the production rate by 6.8 mg h^{-1} per mg mL^{-1} of graphite. Since protein binding to the solid was essential for exfoliation, next we examined the effect of graphite to BSA concentration ratio (mass/mass) on the exfoliation rate.

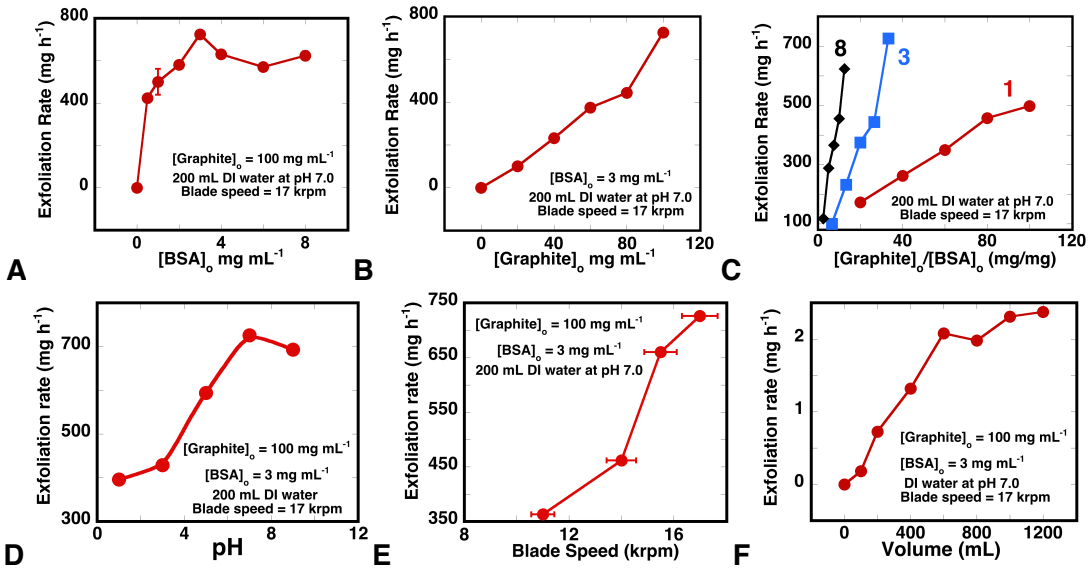

Figure 5.3. Rate of graphene exfoliation as a function of: **A**. BSA concentration **B**. Graphite concentration **C**. Graphite to BSA concentration ratio. 1, 3 and 8 represents the $[BSA]_o$ in mg mL^{-1}. **D.** Function of pH **E**. Function of blade speed and **F.** function of volume of the suspension. Some error bars are too small to be visible.

5.4.5. Effect of graphite to BSA ratio. The effect of graphite to BSA ratio on exfoliation rate was studied by measuring the exfoliation rate at 15 different ratios of graphite to BSA, ranging from 0 to 100. Surprisingly, the ratio of BSA to graphite did not influence the exfoliation rate, but rather depends on initial concentrations ($[BSA]_o$ and $[Graphite]_o$) in the solution (**Figure 5.3.C**). At lower $[BSA]_o$ (1.0 mg mL^{-1}), the exfoliation rate sharply increased from 170 to 500 mg h^{-1} as the $[Graphite]_o$ was increased from 20 to 100 mg mL^{-1} (**Figure 5.3.B**, red lines). The highest exfoliation rate was observed at graphite to BSA ratio of ~33 (mg/mg) at $[Graphite]_o$ of 3.0 mg mL^{-1} (blue lines) , where the $[Graphite]_o$ was 100 mg mL^{-1}. For the next set of the experiments, we increased the $[BSA]_o$ to 8.0 mg mL^{-1} and further increase has been observed (black lines). Next, we studied the effect of pH in exfoliation rate.

5.4.6. Effect of pH. Since the graphene stacking may be inhibited by excess charge on the platelets, we tested the influence of protein charge on exfoliation rate. One simple way to control protein charge is via pH, and we have examined the exfoliation rate at pHs 1.0, 3.0, 5.0, 7.0 and 9.0 at fixed concentration of BSA (3.0 mg mL^{-1}) and graphite (100 mg mL^{-1}), at constant volume (200 mL) and constant blade speed (17 krpm). As shown in **Figure 5.3.D**, exfoliation rate is strongly dependent on pH, and neutral or alkaline pHs or most favorable. Exfoliation rate increased from 375 mg h^{-1} to 725 mg h^{-1} as pH changed from 3.0 to 7.0. We suspect that increased negative charge on BSA (pI is 5.3) increases the exfoliation rate. Next, we examined the effect of blade speed on exfoliation because increased speed increases the shear forces on the crystallites.

5.4.7. Effect of Blade speed. Since exfoliation is due to the shear produced in the blender, we examined how the blade speed is related to generating the critical shear force (Reynolds number - 10^4) required for exfoliation. The systematic increase in blade speed from 11 to 17 krpm, limited range in a kitchen blender, showed increased exfoliation rate from 375 mg h^{-1}

to 725 mg h^{-1} (**Figure 5.3.E**). A linear fit of the plot suggests 65 mg h^{-1} per krpm increase blade speed, which is significant. Further increase in speed is limited by the available options in a kitchen blender. In addition to the blade speed, the volume of the suspension also contributes to the shear rate, which is examined next.

5.4.8. Effect of Volume. The change in volume of the exfoliation addresses two potentially important questions: 1) Is the method scalable by increasing the suspension volume and, 2) how the shear rate is influenced by the volume. The data show that as the volume increased from 100 to 1200 mL, the production rate increased monotonously (**Figure 5.3.F**). At a maximum volume possible in a common kitchen blender (1.2 L), a high rate of 2.4 g h^{-1} was observed. This demonstrates the possibility for gram-scale production of graphene by this approach. The increase in volume, however, resulted in decreasing the effective exfoliation rate from 3.7 mg mL^{-1} h^{-1} (at 200 mL) to 2.0 mg mL^{-1} h^{-1}, at the maximum volume of 1200 mL. This can be seen as a consequence of the decrease in effective shear rate because of the increase in volume.[14]

5.4.9. Characterization of graphene suspensions

The quality of graphene produced is analyzed using Raman spectroscopy, Transmission electron microscopy (TEM), Scanning electron microscopy (SEM) and Colloidal stability studies.

5.4.10. Raman Spectroscopy. Raman spectroscopy has been extensively used as a versatile tool for the characterization of graphene.[17] Exfoliation of graphite to graphene, and the quality of the dispersion was assessed by Raman spectroscopy of dried graphene films on a glass surface. Typical Raman spectra of graphene (**Figure 5.4.A**, in blue) showed G (~1585 cm^{-1}), D (~1350 cm^{-1}) and 2D (2705 cm^{-1}) bands, with significant differences in intensity and shape, compared to the parent graphite flakes (in red). The signature of 2D

band was very prominent in the exfoliated samples, i.e. a broader (FWHM ~ 75 cm^{-1}) and symmetric peak was appeared, in contrast to unsymmetrical graphite (FWHM ~57 cm^{-1}) peak.

The apparent changes in intensity of Raman peaks give an idea about the size, defect and number of layers present in the exfoliated graphene.[13] Remarkably, the increase in intensity of D band, which quantitatively represents disorders and edge carbon atoms, has increased after the exfoliation. An increase in I_D/I_G ratio from ~0.1 to ~0.6 is observed after 30 minutes of exfoliation. Another noticeable change was the appearance of the shoulder peak the G band called D' band, which is activated by defects.[17] The increase in intensity of 2D band resulted in I_{2D}/I_G ~ 0.9 qualitatively represents the presence of FLG in the suspension. Further, a statistical analysis of number of layers (N_G), lateral size (<L>) and type of defects in our samples was examined using the Raman intensity ratios (**Figure 5.4.C and D**).[13]

The statistical analysis was perfomed using equation 1 and 2, from the intensity ratios of six different spectra. The number of layers in the graphene was calculated using the ratio of I_{2D} to its shoulder peak (I_{2D} – 30 cm^{-1}), which is prominent only in the graphite spectrum (**Figure 5.4.A**, red lines). The above ratio in the graphene samples was noramlized with the ratio of precursor graphite, according to the published empirical formula.[13] The analysis gave N_G as 3.6 (±0.4) in the samples, regardless of the exfoliation period (**Figure 5.3.B**). It is noteworthy that the Raman spectra are done in dried, precipitated samples, so the cacluated value would be overestimated, and suggested to be substantiated using microscopy studies.[11,13,17]

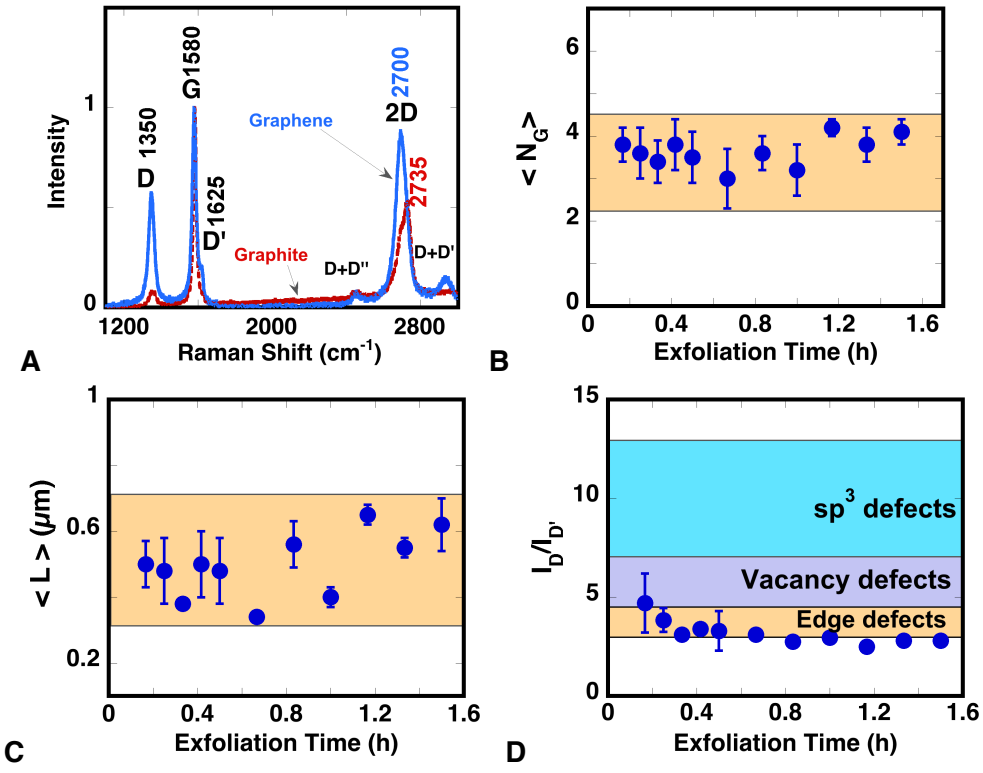

Figure 5.4. A. Raman spectra of graphene (blue) in comparison with graphite (red). **B.** Change in number layers in graphene with exfoliation time, as calculated using equation (1). **C.** Change in lateral size of graphene sheets with exfoliation time, as calculated using equation (2). **D.** Raman analysis of graphene showing minor edge defects. All the analysis were done using six Raman spectral data sets per sample.

The lateral size of exfoliated graphene is calculated from I_D/I_G ratios, using Equation (2)[13] as a function of exfoliation time. The average size of the sheets was 0.5 (±.1) μm and appeared to be highly uniform (**Figure 5.4.C**). This suggests that the delamination and fragmentation of the platelets are happening simultaneously at the intial stages of exfoliation process. To futher validate the exfoliation mechanism we carried out the FLG was subjected to blending for 90 more minutes. The blending of biofunctionalized FLG was tested for fragmentation and delamination using Raman spectroscopy (**Figure 5.5**). The findings suggest that there is no further delamination or fragmentation was occurred at this step. This supports the recent kinetic theory on exfoliation of 2D materials that the exfoliation is driven by the delamination multilayared graphite and further exfoliation of FLG is kinetically unfavorable.[18]

The ratio of I_D to $I_{D'}$ represents the type of defect(s) present in the graphene.[13] The maginitude of $I_D/I_{D'}$ in our samples was 3.2 (±.6), which is within the range of edge type defects (**Figure 5.4.D**). It is very important to note that we do not have any major sp^3 defects, which suggests that no oxidation to the sheets was noticed during the exfoliation process. As such, the Raman studies clearly endorse the successful exfoliation of graphite to few layer, micron size and defect free graphene. The findings from Raman studies were further verified using microscopy studies as follows.

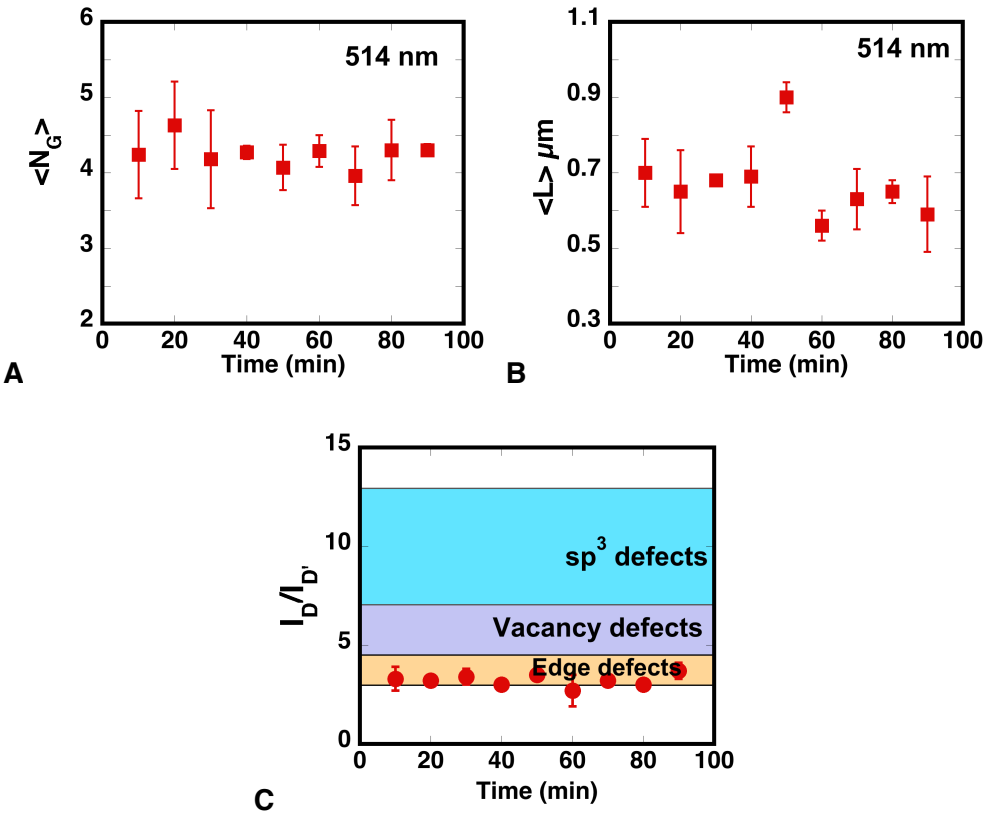

Figure 5.5. Distribution of number of layers (**A**) , lateral size (**B**) and defects (**C**) Few layer graphene (FLG) subjected to blending after removing unexfoliated graphite. This shows that further delamination or fragmentation of FLG has not effected by the process.

5.4.11. Microscopy studies. Transmission electron microscopy (TEM) images were used to distinguish the number of layers present in the solution, which confirms the degree of exfoliation. TEM images were collected using dried, deposited graphene (20 μg mL^{-1}) on a Cu-grid (**Figure 5.7 A-D**) and compared with the Scanning Electron Microscopy (SEM) image of graphite (**Figure 5.6**) .

Representative images shown in **Figure 5.7**, suggest the presense of 1-3 layers of stacked graphene sheets with an average 0.33 micron lateral size. The histogram of the sheet size measured from 10-15 sheets using diffrerent TEM images is given in **Figure 5.7.F**. The sheets are found to have a folded or crumbled morphology, which reduces the average lateral size (**Figure 5.7, A-D**). This could be the reason for the decrease in average size (0.33 μm) of sheets measured by TEM (**Figure 5.7.F**), when compared to Raman analysis (0.5 μm, **Figure 5.4.C**). A selected area electron diffrection pattern of the larger sheet in **Figure 5.7.A** is shown in **Figure 5.7.E** , which implied a polycrystalline phase which could be due to the presence of amorphous BSA functionalization on the sheets and foldings. Overall, the TEM studies supported the successful exfoliation of graphite to micron size biofunctionalized FLG.

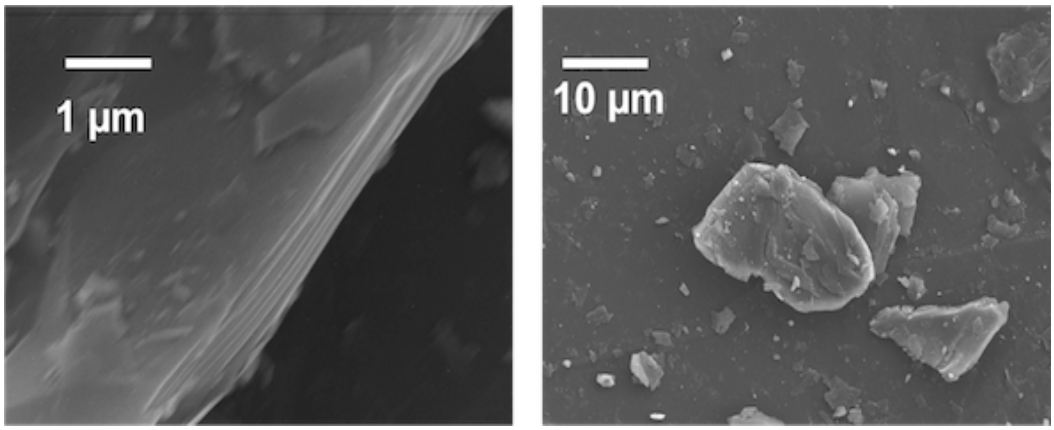

Figure 5.6. The SEM images of graphite showing multi layered, micron size platelets.

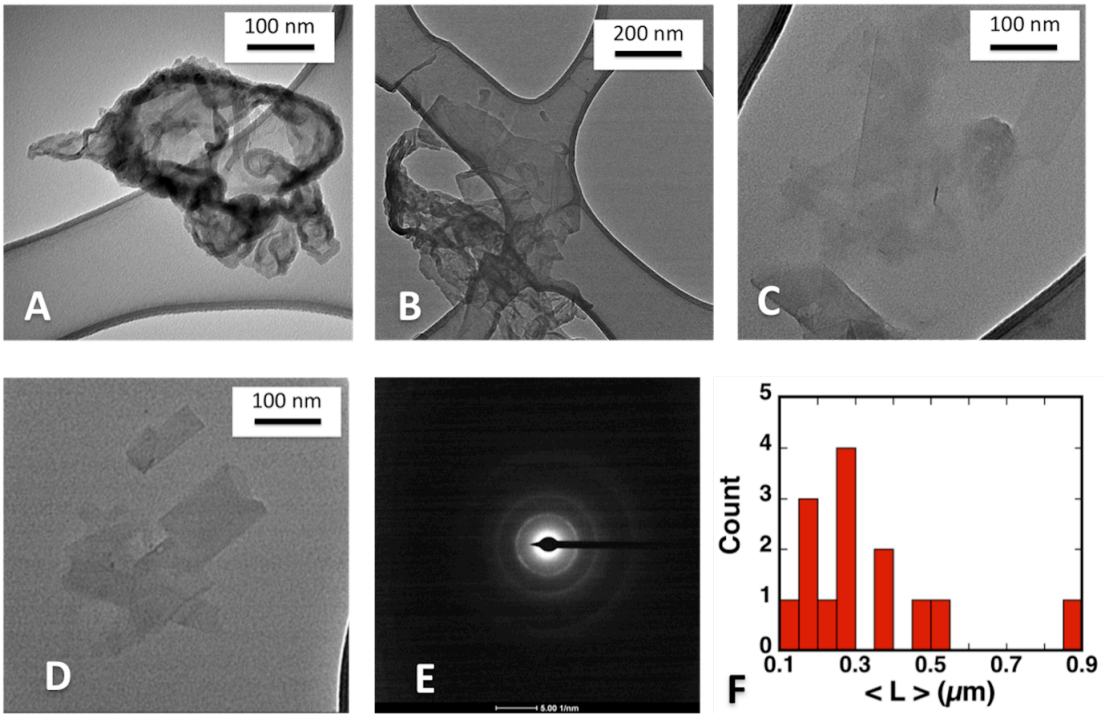

Figure 5.7. TEM images of graphene samples show folded (**A** and **B**), bi/tri layer distribution (**C** and **D**) in the samples. **E.** Selected area electron diffraction pattern of folded sheet in A. **F.** Histogram showing the size distribution of graphene measured from TEM images.

5.4.12. Biofunctionalization of Graphene. Production of aqueous graphene dispersions, in particular, with stability in biological conditions is an active research area in chemical and biomaterial sciences. Water stability of graphene derivatives is usually attributed to hydrophilic modification. Here, by *in situ* modification of graphene with BSA, we achieved graphene aqueous dispersions with concentrations as high as 6.8 mg mL^{-1}.

To prove the *in situ* biofunctionalization, the presence of bound BSA to graphene sheets is confirmed using UV spectroscopy and zeta potential studies. Due to strong graphene absorption at 200-300 nm, resolving the 280 nm absorption (A_{280}) of the bound protein was inconclusive (**Figure 5.8.A**). Alternatively, we determined the unbound BSA concentration using A_{280} after separating the bound BSA by centrifugation (12000 rpm for 45 minutes). We examined the free [BSA] as a function of the exfoliation time and from that we calculated the $[BSA]_{bound.}$ We observed that the $[BSA]_{bound}$ gradually increasing (blue lines) as more graphene was produced in the medium (**Figure 5.8.B**, inset). Conversely, one can propose that BSA binding and exfoliation happen simultaneously using this treatment. Nonetheless, the exchange of BSA from solution to graphene phase proves the *in situ* biofunctionalization of graphene.

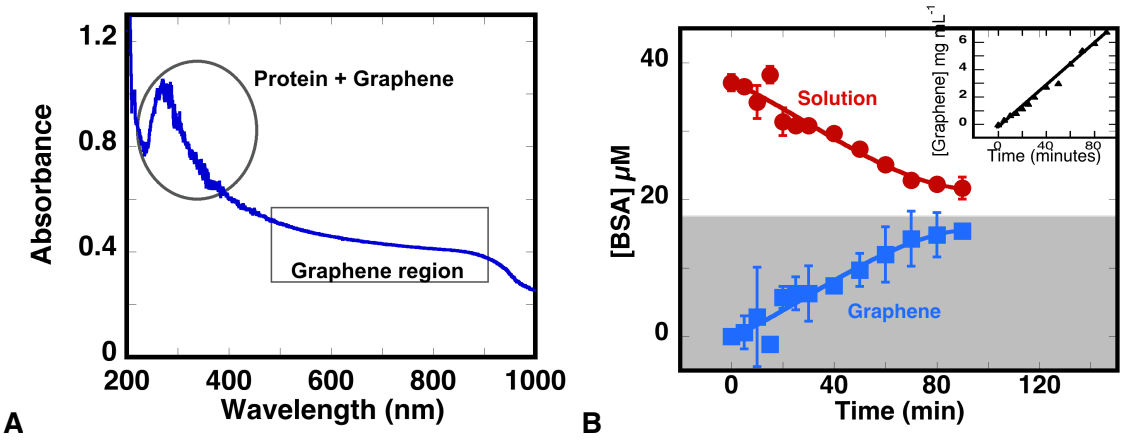

Figure 5.8. A. Absorption spectrum of the biofunctionalized graphene. Absorbance at 250-400 nm was combined with BSA and the graphene. The combination of absorbance, extinction and scattering of graphene sheets centered around 600 nm. **B.** *In situ* biofunctionalization of graphene is confirmed by the exchange of BSA from the solution (red) to the graphene (blue) with increasing exfoliation time. The increase in graphene concentration in the system is shown in the inset.

After 90 minutes of exfoliation, the $[BSA]_{bound}$ was 15 μM which is ~40 % of $[BSA]_{int}$ and 18% (mass/mass) of total graphene concentration (6.8 mg mL^{-1}). The $[BSA]_{bound}$ corresponds to 3% area covered by BSA on graphene sheets, assuming that graphene is monolayer and BSA is completely intact in structure. However, since the graphene is few layered and BSA showed changes in secondary structure on binding to the graphene surface (from CD studies, **Figure 5.9.A**), we propose that 15-20% of the exposed graphene sheets are functionalized by BSA.

The biofunctionalization was further verified using time dependent zeta potential measurements shown in **Figure 5.9.B** We measured the zeta potential of graphene dispersions as the exfoliation progressed and found that the surface potential was constant around -27 (± 3) mV at pH 7.0. The observed surface potential of graphene is attributed to the presence of bound BSA, since the pristine graphene has no sp^3 defects due to charged oxygen functional groups, such as in graphene oxide. This validates the hypothesis that the protein is been modified to the graphene and the negative charge of BSA is stabilizing the sheets in the aqueous media.

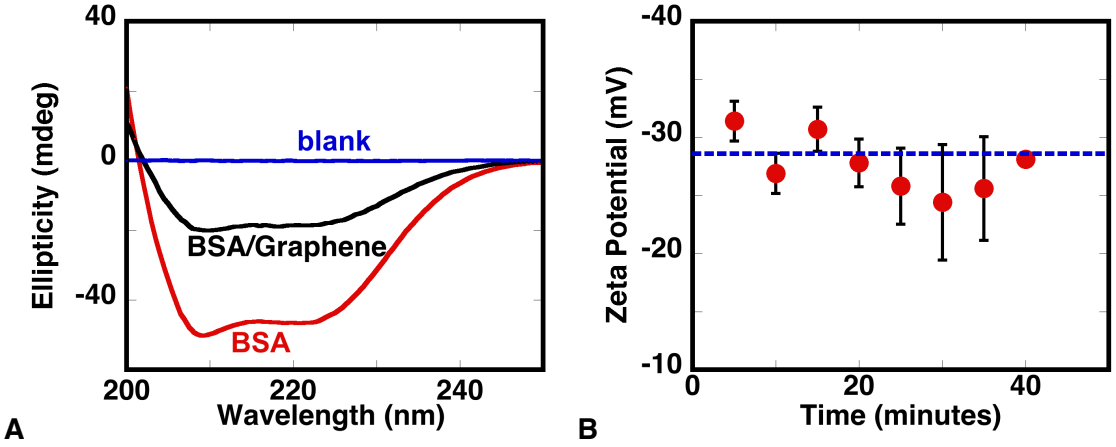

Figure 5.9. A. Circular dichroism spectra of BSA after functionalized to graphene (black) in comparison with unbound BSA showed significant changes in secondary structure. A quantitative comparison using spectral intensities is limited by the unavailability of precise [BSA] at the bound state. **B.** The change in Zeta potential of graphene is plotted as a function of the exfoliation time. The observed negative zeta potential of graphene is due to the presence of functioned BSA.

5.4.13. Colloidal stability of Graphene dispersions. The biological stability of aqueous graphene dispersions under relevant conditions, with varying temperatures and pHs, and in fetal bovine serum (FBS) is studied. Stability of graphene/GO dispersions at the aforementioned conditions depends on the type and degree of functionalization.[19] In the present study, BSA is the stabilizing agent for graphene, which can undergo structural changes in stresses such as pH and temperature.[20] Consequently, these changes can influence the stability of graphene dispersions and this has been investigated by UV-Vis spectroscopy, and zeta potential studies.

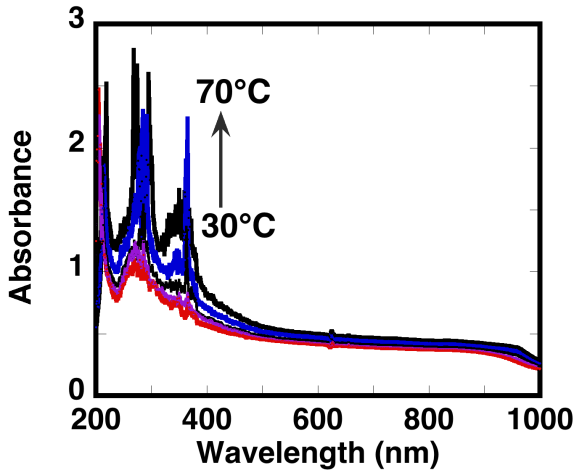

Figure 5.10. Changes in absorption spectrum of graphene at elevated temperatures.

Effect of temperature: The role of temperature in the formation of aggregated graphene was studied in two different aspects. First, we studied the effect of temperature on aggregation at increasing temperatures from 25 to 80°C by measuring the extinction at 660 nm. There was no significant change in concentration of graphene (using E_{660}) at elevated temperatures (**Figure 5.10**). However, significant spectral changes in the 250 to 400 nm region, occurred after 60°C, which is noticeably close to the denaturation temperature of BSA.[21] An increase in absorption at 660 nm is also due to the changes in graphene/BSA complex upon structural changes in BSA. Second, the storage stability of graphene at three different temperatures (5, 25 and 50°C) in DI water at pH 7.0 was studied by measuring E_{660} at specific intervals for more than a month and there has been no aggregate formation (**Figure 5.11.A**). The E_{660} of the graphene dispersions after 20 days showed no significant changes.

Biological uses of nanomaterials require stability in biological fluids such as serum. It is possible that graphene can bind to the biomolecules present in the serum and aggregate, which would limit its practical uses. We studied the storage stability of graphene in a 50% FBS solution at 5°C and checked the E_{660} daily for more than two weeks. There was no detectable precipitation or aggregation when 50% FBS was added (**Figure 5.11.B**) but the E_{660} showed gradual decrease (**Figure 5.11.B**).

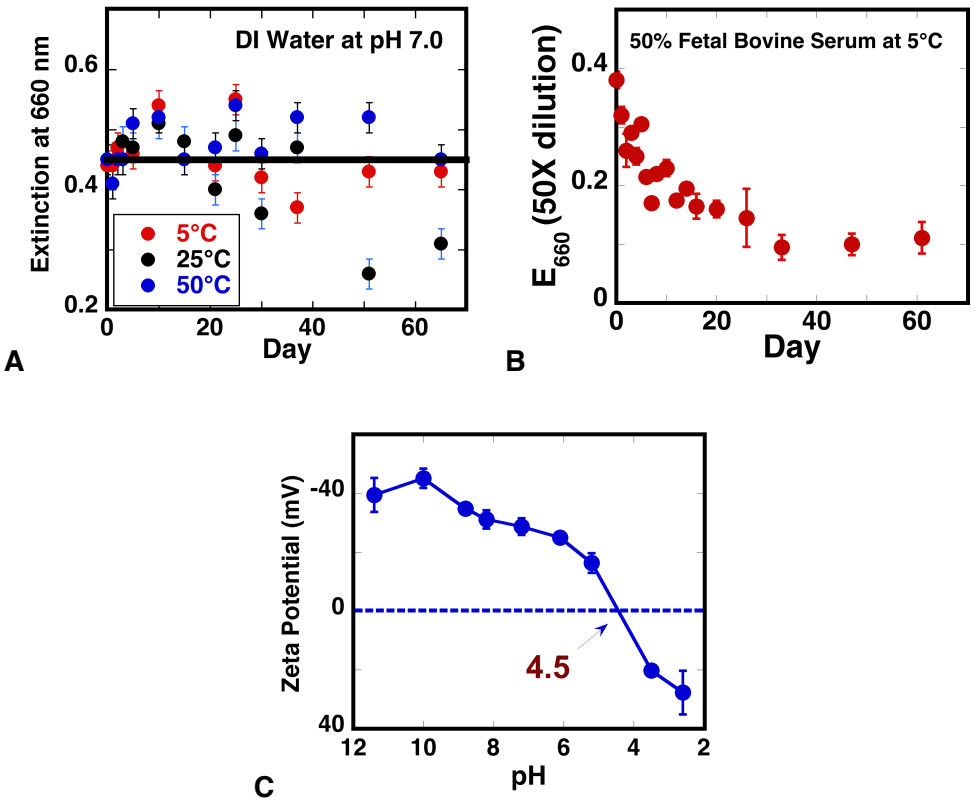

Figure 5.11. **A**. Change in graphene concentration of dispersions stored at 5, 25 and 50°C. **B.** Stability of graphene in 50% fetal bovine serum (FBS). **C**. Zeta potentials of graphene dispersions as a function of pH.

After one week, the concentration of graphene was reduced to half of its original value but retained that concentration for two more weeks with no significant drop. We hypothesize that this might be due to the activity of the proteases that are present in FBS, which might deteriorate BSA present on the grapheme sheets and induce aggregation. This was confirmed by checking the stability of graphene in the presence of a protease, trypsin (0.2 mg mL^{-1}), in DI water at pH 7.4. After one hour of incubation with trypsin at 37ºC, there was precipitation. Therefore, the protein molecule is necessary for aqueous stability of graphene sheets, which was noted by other groups as well.[10] However, the observed half-life of 10 days in FBS is relevant for biological/cellular studies of graphene. This analysis could potentially broaden the uses of our graphene in various applications, such as sensing and toxicity studies in biological fluids.

Effect of pH: The role of pH on graphene stability was studied using zeta potential measurements. **Figure 5.12.A** shows the change in zeta potential (ξ) of graphene with pH, where the observed negative surface charge of graphene is due to the presence of the BSA functionalization. As the pH decreased from 11 to 2.5 the zeta potential varied from -40 to +40 mV, and the isoelectric point (ξ =0 mV) was noted at ~ 4.5 which is close to the isoelectric point of BSA.[20] Additionally, the zeta potential of graphene incubated at varying pHs was measured after incubation at 25 °C for a week. The zeta potential of the solutions was retained (~100%) after one week (**Figure 5.12.A**), which proves the colloidal stability of graphene dispersions over a wide range of pH (3-11). The stability was further supported by measuring E_{660} of graphene at the different pHs before and after incubation (**Figure 5.12.B**). However, at pH value near ξ =0 mV, aggregated graphene was formed and a substantial decrease in concentration at pH 5.1 was noted. This emphasizes the crucial role of electrostatic repulsion between protein molecules in stabilizing graphene in aqueous media. Also, this study brings out a new opportunity to design biographene with desirable pI values by using particular proteins for exfoliation.

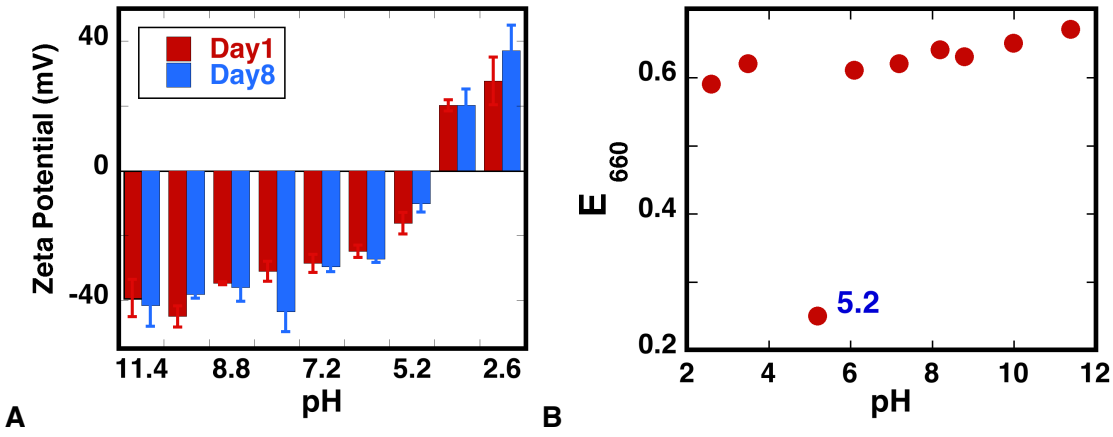

Figure 5.12. A. Zeta potential of biofunctionized graphene after incubation at different pHs showed insignificant changes after a week at 25°C. **B.** The absorbance of graphene at varying pHs. A decrease in absorbance at pH 5.2 was noted because of the aggregation near the isoelectric point of BSA (5.5).

5.4.14. Conductivity Measurements. Graphene sheets with few layers and microns of lateral area have high electrical conductivity.[13] The exfoliated graphene was painted onto a standard printing paper (cellulose) (22cm x 14cm, 650 μg/cm^2), and the conductivity has been measured using standard 4-point probe resistivity, which is more accurate than 2-point method.[22] (**Figure 5.13.A and B**). The adsorption of graphene onto the paper was confirmed by SEM images (**Figure 5.13.C**).

The system showed excellent, continuous conductivity over a range from 0 to 45 V with a steady output current. The thickness of graphene layer was measured from the cross-sectional SEM image (**Figure 5.13.C**) was 3 μm, which was further confirmed by theoretical calculation based on the adsorption efficiency (650 μg cm^{-2}) and density of graphite (2.2 g cm^{-3}). The sheet conductivity of the paper was calculated to be as high as 32,000 S m^{-1} using Equation 3 ($R = \rho L/Wt$) with sheet resistance (R_s) of 50 Ω sq^{-1}. High conductivity was also demonstrated in a circuit connecting an LED and a 12 V battery in **Figure 5.13.D**.

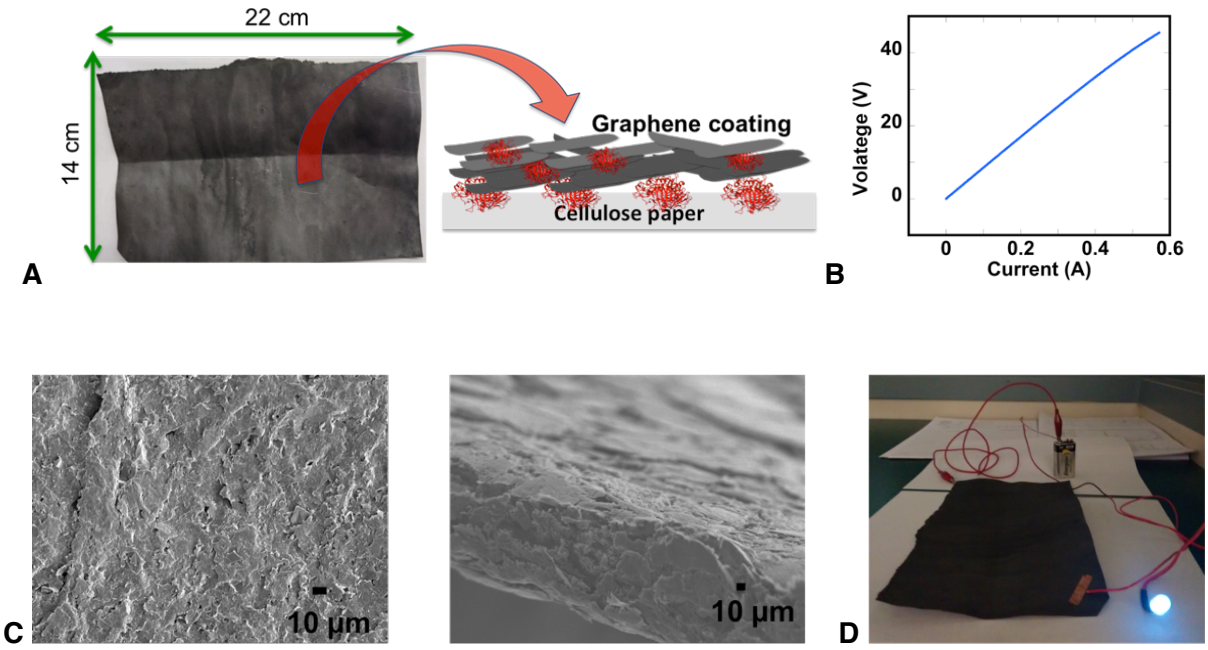

Figure 5.13. A. Photograph of graphene-coated paper **B.** Linear I-V response of the paper measured using a standard 4-point circuit. **C.** Representative SEM images of the graphene-coated paper confirming the presence of bound graphene. **D.** Conductivity of the paper is illustrated by using the paper in an LED circuit.

5.5. Discussion

An efficient, simple and robust approach for multi-gram production of biofunctionalized graphene from graphite, under ambient conditions, is presented here. In this top down approach, micromechanical exfoliation of graphite was achieved by the shear/turbulence in a kitchen blender and proteins were used to biofunctionalize pristine graphene sheets. The aqueous graphene suspensions show storage stability under biologically relevant conditions.

Exfoliation of graphite using biomolecules such as proteins,[9,10,11,23] carbohydrates[24] and polysaccharides[25,26] offer green, biocompatible carbon based nanomaterials for various biomedical and drug delivery applications. Recently, proteins such as BSA, lysozyme and hydrophobins were used for liquid phase exfoliation of graphite to FLG by ultrasonication.[9,10,11]

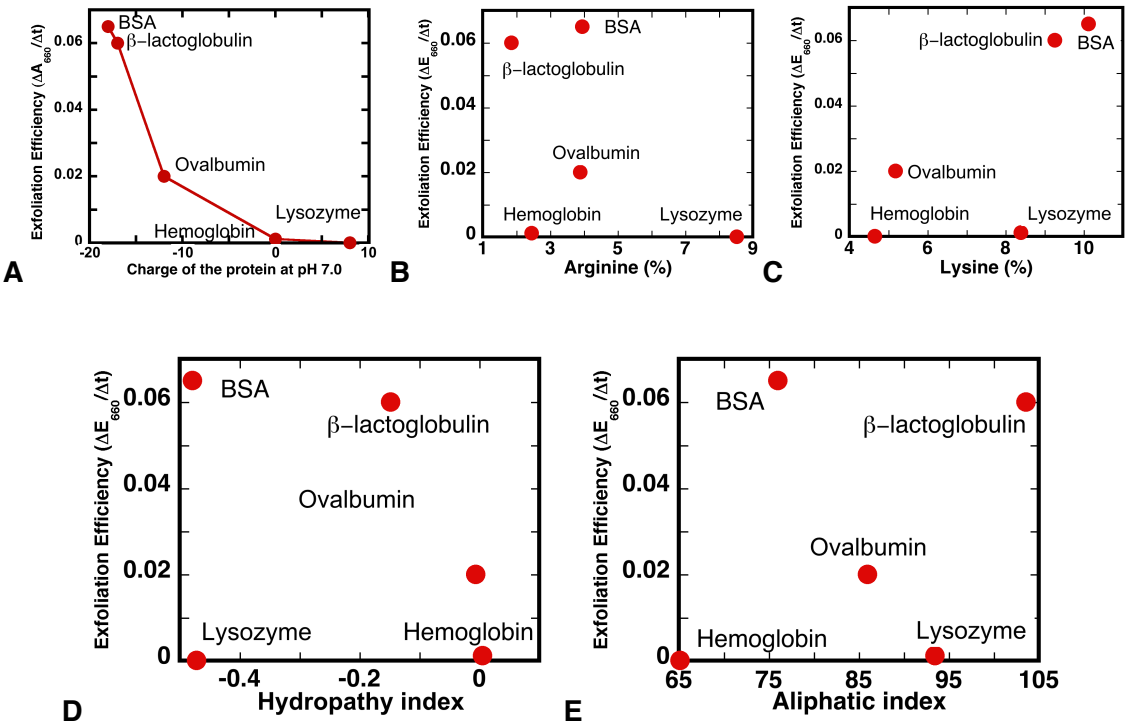

Figure 5.14. Exfoliation efficiency of different proteins is correlated with **A.** Charge **B.** Lysine (%) **C.** Arginine (%) **D.** Hydropathy index and **E.** Aliphatic index. The analysis suggests that charge is the key factor in determining the exfoliation efficiency of proteins.

Proteins are suggested to interact with graphene through hydrophobic residues but the effect of proteins in stabilizing the dispersions is yet to be established.[9] Herein, by using proteins with different surface (amino acid distribution) and bulk properties (charge and hydrophobicity), protein charge has been shown to be an important parameter for exfoliation. Not only protein adsorption on the flakes would be able to reduce the sheet-to-sheet (van der Waal's) interactions, but also the charge on the protein is critical for the overall stability of the functionalized sheets. So, we noted that the proteins with sufficient surface charge (in our case >-15) showed maximum yield when compared to smaller proteins with less net charge, such as lysozyme (**Figure 5.14**). Moreover, we found no correlation with other parameters such as hydrophilicity, number of charged amino acids and volume of aliphatic residues in the protein.

In general, sonication based exfoliation was reported to have low exfoliation rates, cracking of the platelets and their oxidative damage.[12] Exfoliation rates by several methods are compared in **Figure 5.15.A**. Sonication assisted exfoliation methods, for example, using BSA, lysozyme and hydrophobins (in 60% ethanol) demonstrated exfoliation rates of 0.27, 0.33 and 0.83 mg mL^{-1} h^{-1}, respectively.[9,10,11] Current approach achieved rates of 4-7 mg mL^{-1} h^{-1} in a completely aqueous medium, and the exfoliation rate was found to be linear over an extended period of time (1.5 h, **SI Figure 5.8.B**). To the best of our knowledge, this is the highest rate for liquid phase exfoliation in water (**Figure 5.15.A**). The exfoliation rates were found to be affected by factors such as 1) $[BSA]_o$, 2) $[Graphite]_o$, 3) pH, 4) total volume, 5) blade speed, 6) viscosity, 8) surface tension, to name a few. Experiments with varying $[BSA]_o$ and $[Graphite]_o$ were conducted while keeping factors 3-6 constant.

Assuming that the viscosity and surface tension changes are intrinsic to protein concentrations in our experiments, the following relation for the rate of exfoliation (r) can be deduced as given in the following equation:

$$r \propto [BSA]_o^{\,a} \times [Graphite]_o^{\,b} (pH)^c (Volume)^d (blade\ speed)^e$$

where *a-e* are the corresponding orders of the reaction. Experiments with increasing $[BSA]_o$ showed saturation of exfoliation rate at around 3 mg mL^{-1} (**Figure 5.3.A**) and above this value, 'a' is set to zero. But the rate depended more steeply and linearly on $[Graphite]_o$. This sheds light onto the mechanistic aspect of the exfoliation, in which the graphite-to-graphite collisions, with threshold Reynolds's frequency, is rate limiting in the overall exfoliation process. The bombardment causes fragmentation of the graphite platelets, which facilitates the shear exfoliation process, because of low van der Waals forces between small graphene layers.[3] In turn, BSA molecules kinetically trap the exfoliated sheets very rapidly and protect them from restacking. In addition, the other experimental variable pH, volume, protein charge, and blade speed also contributed to the exfoliation rates (**Figure 5.3**). We fitted these data to linear plots (an approximation), and extracted the following values for our guidance: b=1.2; c=0.29, d=0.99, and e=1.7 in the above equation. Based on these, we postulate that multiple factors control the exfoliation rate, and it can be maximized in many dimensions as desired.

BSA plays three other roles in exfoliation: 1) lowering the surface tension of the medium,[27] 2) binding to the exposed graphite surface[9] and lower its surface free energy, and 3) stabilize the graphene sheets in water by positioning the charged and/or hydrophilic functional groups for favorable interactions with the solvent or enhance solvation of the platelets. [28] The intrinsic hydrophobicity of carbon nanomaterials limits their bio-processability.[29] The availability of hydrophilic graphene is largely restricted to GO, which

was shown to have structural defects, oxidative debris and metallic impurities limiting its biological use.[30] The biofunctionalized grapheme, reported here, was highly stable in water at various pHs and room temperature, which was not demonstrated in previous studies. Stability and *in vivo* and *in vitro* performance of nanomaterials are challenging due to aggregation, protein corona formation, and protease activity in biological fluids, particularly in serum.[31,32] Here, the biofunctionalized graphene showed initial aggregation or degradation in 50% FBS due to protease activity but no further changes occurred over several days. Biographene made here opens up new opportunities to modify its surface with many other (bio)molecules, as previously demonstrated with GO.[33]

Electrical conductivity of graphene also depends on the method of exfoliation and the degree of oxidation.[34] Surprisingly, the BSA coated graphene showed excellent sheet conductivity, which is 6-7 times better than previously reported graphene based polymeric composites (**Figure 5.15.B**).[35] Values of 32,000 S m^{-1} for our biographene coated paper (22 cm x 14 cm) is close to the highest reported value of 45,000 S m^{-1}, in which a relatively smaller area (5 cm in diameter) was used, and the graphene was produced by GO reduction, followed by filtration.[41] Compared to these other conductive graphene papers which require laborious filtration, annealing or reduction,[39,40,41] this flexible, larger area metal-free conducting sheets indicated some of the highest values, over a large voltage window, following Ohm's law. Since many composite films show conductivities over a small voltage window (usually in mV), our sample has some advantages. The first time illustration of highly conductive graphene produced by direct exfoliation of graphite is demonstrated here with edible proteins and a kitchen blender, inexpensive apparatus without using toxic chemicals, metals or solvents.

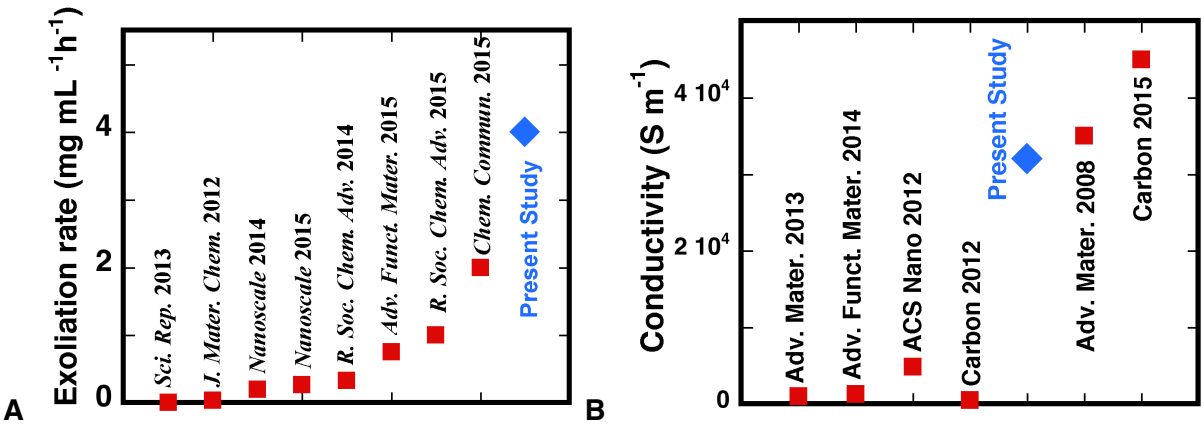

Figure 5.15. A) Comparison of the rate of exfoliation in aqueous media achieved in the current method with published approaches.[5,9,10,11,14,23,25,26] **B)** The high conductivity of biographene deposited on paper when compared to the conductivities of similar materials.[36,37,38,39,40,41] Reference numbers for the corresponding data are shown in each of the panels.

5.6. Conclusions

High quality graphene suspended in aqueous media is highly desirable for the biological applications of this 'wonder material'. Due to its inherent hydrophobicity, graphene needs adequate biofunctionlization for its dispersion in water. Proteins were recently used as the exfoliating agents, as well as modifiers, to yield aqueous graphene dispersions via ultrasonication, which gave slow exfoliation rates (< 1 mg mL^{-1} h^{-1}), limited scalability (<100 mL) but induced basal plane defects (O content of 10-25%).[12,13] Breaking of the sheets, production of reactive sites and reaction of the damaged sites with oxygen were suggested to be some of the disadvantages of sonication.[12] To overcome these disadvantages, shear/turbulence forces were used as a successful alternative, although, to date, the approach has been limited to organic media and surfactant solutions.

Here, the exciting possibilities of shear/turbulence method were coupled with the surface active properties of edible proteins and produced multi-gram scale synthesis of unoxidized, low-defect graphene suspensions in water. The protein charge played a key role in exfoliation of graphite, the strongly negatively charged BSA showed maximum efficiency. The GO or chemically reduced GO (rGO) used is prepared by tedious oxidation/reduction treatments; contaminate the GO with metallic or other impurities.[2] The biographene is obtained directly from graphite and proteins, which could be an alternative to GO or rGO for a variety of applications. Moreover, this approach could be extended to many other proteins, as desired for particular applications.

Herein, the graphene concentration as high as 7 mg mL^{-1} was achieved, at high rates of exfoliation, and exfoliation rate is tied with specific attributes of the reaction medium for future scale-up. An empirical relation was deduced for further optimization of the exfoliation

rates. Biographene with particular isoelectric points or tunable charge can be produced by selecting appropriate proteins for the exfoliation or by controlling the pH of the medium.

These suspensions also showed long-term thermal, pH and storage stabilities under biologically relevant conditions, including in a biological fluid (fetal serum) which a very good test for biological applications. These aqueous graphene dispersions, with improved biological stability, could be good alternatives to widely used GO or rGO for a variety of applications in biomedical and bioengineering fields.[42] The biographene-coated cellulose paper is unique in that it is the first conductive, metal-free cellulose-protein-graphene hybrid material that has not been reported before. This simple exfoliation method could lead to greater access of graphene for laboratories with limited resources or applications that need large quantities, and it could further revolutionize the graphene field.

5.7. References

1. C. Chung, Y. K. Kim, D. Shin, S. R. Ryoo, B. H. Hong, D. H. Min, Biomedical applications of graphene and graphene oxide, *Acc. Chem. Res.* **2013**, *46*, 2211-2224.

2. Wong, C. H. A.; Sofer, Z.; Kubešová, M.; Kučera, J.; Matějková, S.; Pumera, M. Synthetic routes contaminate graphene materials with a whole spectrum of unanticipated metallic elements. *Pro. Natl. Acad. Sci.,* **2014**, *111*, 13774-13779.

3. Yi, M.; Shen, Z. A review on mechanical exfoliation for the scalable production of graphene. *J. Mater. Chem. A,* **2015**, *3*, 11700-11715.

4. Chen, X.; Dobson, J. F.; Raston, C. L. Vortex fluidic exfoliation of graphite and boron nitride. *Chem. Commun.* **2012**, *48*, 3703-3705.

5. Morishita, T.; Okamoto, H.; Katagiri, Y.; Matsushita, M.; Fukumori, K. High-yield ionic liquid-promoted synthesis of boron nitride nanosheets by direct exfoliation. *Chem. Commun.* **2015,** *15*, 12068-12071.

6. Chen, I. W. P.; Chen, Y. S.; Kao, N. J.; Wu, C. W.; Zhang, Y. W.; Li, H. T. Scalable and high-yield production of exfoliated graphene sheets in water and its application to an all-solid-state supercapacitor. *Carbon* **2015**, *90*, 16-24.

7. Lotya, M.; King, P. J.; Khan, U.; De, S.; Coleman, J. N. High-Concentration, Surfactant-Stabilized Graphene Dispersions. ACS Nano **2010**, 4, 3155-3162.

8. Yang, K.; Li, Y.; Tan, X.; Peng, R.; Liu, Z. Behavior and Toxicity of Graphene and Its Functionalized Derivatives in Biological Systems. *Small* **2013**, *9*, 1492-1503.

9. Ahadian, S.; Estili, M.; Surya, V. J.; Ramon-Azcon, J.; Liang, X.; Shiku, H.; Ramalingam, M.; Matsue, T.; Sakka, Y.; Bae, H. *et al.* A. Facile and green production of aqueous graphene dispersions for biomedical applications. *Nanoscale* **2015**, *7*, 6436-6443.

10. Joseph, D.; Tyagi, N.; Ghimire, A.; Geckeler, K. E. A direct route towards preparing pH-sensitive graphene nanosheets with anti-cancer activity. R. Soc. Chem. Adv. **2014**, 4, 4085-4093.

11. Gravagnuolo, A. M.; Morales-Narváez, E.; Longobardi, S.; da Silva, E. T.; Giardina, P.; Merkoçi, A. In Situ Production of Biofunctionalized Few-Layer Defect-Free Microsheets of Graphene. *Adv. Funct. Mater.* **2015**, *25*, 2771-2779.

12. Skaltsas, T.; Ke, X.; Bittencourt, C.; Tagmatarchis, N. Ultrasonication Induces Oxygenated Species and Defects onto Exfoliated Graphene. *J. Phys. Chem. C* **2013**, *117*, 23272-23278.

13. Paton, K. R.; Varrla, E.; Backes, C.; Smith, R. J.; Khan, U.; O'Neill, A.; Boland, C.; Lotya, M.; Istrate, O. M.; King, P. *et al.* Scalable production of large quantities of defect-free few-layer graphene by shear exfoliation in liquids. *Nat. Mater.* **2014**, *13*, 624-630.

14. Varrla, E.; Paton, K. R.; Backes, C.; Harvey, A.; Smith, R. J.; McCauley, J.; Coleman, J. N. Turbulence-assisted shear exfoliation of graphene using household detergent and a kitchen blender. *Nanoscale* **2014**, *6*, 11810-11819.

15. Yi, M.; Shen, Z. Kitchen blender for producing high-quality few-layer graphene. *Carbon* **2014**, *78*, 622-626.

16. Yun-Hwa P, H.; Jack, A, O. Food-Grade Proteins from Animal By-Products. In *Handbook of Analysis of Edible Animal By-Products*; Fidel, T., Ed.; CRC Press: 2011; pp 13-35.

17. Ferrari, A. C.; Basko, D. M. Raman spectroscopy as a versatile tool for studying the properties of graphene. *Nat. Nano.* **2013**, *8*, 235-246.

18 Texter, J. A Kinetic Model for Exfoliation Kinetics of Layered Materials. *Angew. Chem.* **2015**, *54*, 10258-10262.

19. Georgakilas, V.; Otyepka, M.; Bourlinos, A. B.; Chandra, V.; Kim, N.; Kemp, K. C.; Hobza, P.; Zboril, R.; Kim, K. S. Functionalization of Graphene: Covalent and Non-Covalent Approaches, Derivatives and Applications. *Chem. Rev.* **2012**, *112*, 6156-6214.

20. Foster, J. F. Some aspects of the structure and conformational properties of serum albumin. In *Albumin: Structure, Function and Uses*, Rosenoer, V. M., Oratz, M., Rothschild, M. A., Eds. Pergamon: 1977; pp 53-84.

21. Takeda, K.; Wada, A.; Yamamoto, K.; Moriyama, Y.; Aoki, K. Conformational change of bovine serum albumin by heat treatment. *J. Protein Chem.* **1989**, *8*, 653-659.

22. Smits, F. M. Measurement of sheet resistivities with the four-point probe. *Bell Syst Tech. J.* **1958**, *34*, 711-718.

23. Ge, Y.; Wang, J.; Shi, Z.; Yin, J. Gelatin-assisted fabrication of water-dispersible graphene and its inorganic analogues. *J. Mater. Chem.* **2012**, *22*, 17619-17624.

24. Punith Kumar, M. K.; Shanthini, S.; Srivastava, C. Electrochemical exfoliation of graphite for producing graphene using saccharin. *R. Soc. Chem. Adv.* **2015**, *5*, 53865-53869.

25. Chabot, V.; Kim, B.; Sloper, B.; Tzoganakis, C.; Yu, A. High yield production and purification of few layer graphene by Gum Arabic assisted physical sonication. Sci. Rep. **2013**, 3.

26. Uysal Unalan, I.; Wan, C.; Trabattoni, S.; Piergiovanni, L.; Farris, S. Polysaccharide-assisted rapid exfoliation of graphite platelets into high quality water-dispersible graphene sheets. *R. Soc. Chem. Adv.* **2015**, *5*, 26482-26490.

27. Niño, M.; Patino, J. M. R. Surface tension of bovine serum albumin and tween 20 at the air-aqueous interface. *J. Am. Oil Chem. Soc.* **1998**, *75*, 1241-1248.

28. Shih, C. J.; Lin, S.; Strano, M. S.; Blankschtein, D. Understanding the Stabilization of Liquid-Phase-Exfoliated Graphene in Polar Solvents: Molecular Dynamics Simulations and Kinetic Theory of Colloid Aggregation. J. Am. Chem. Soc. **2010**, 132, 14638-14648.

29. Feng, L., Liu, Z., Graphene in biomedicine: opportunities and challenges, *Nanomedicine,* **2011**, *6*, 317-324.

30. Pattammattel, A, Williams, C. L., Pande, P., Tsui, W. G., Basu, A. K., Kumar, C. V., Biological relevance of oxidative debris present in as-prepared graphene oxide, *R. Soc. Chem. Adv.* **2015**, *5*, 59364-59372.

31. Tenzer, S.; Docter, D.; Kuharev, J.; Musyanovych, A.; Fetz, V.; Hecht, R.; Schlenk, F.; Fischer, D.; Kiouptsi, K.; Reinhardt, C. *et al.* Rapid formation of plasma protein corona critically affects nanoparticle pathophysiology. *Nat. Nano.* **2013**, *8*, 772-781.

32. Monopoli, M. P.; Walczyk, D.; Campbell, A.; Elia, G.; Lynch, I.; Baldelli Bombelli, F.; Dawson, K. A. Physical–Chemical Aspects of Protein Corona: Relevance to in Vitro and in Vivo Biological Impacts of Nanoparticles. *J. Am. Chem. Soc.* **2011**, *133*, 2525-2534.

[33] Pattammattel, A.; Puglia, M.; Chakraborty, S.; Deshapriya, I. K.; Dutta, P. K.; Kumar, C. V. Tuning the Activities and Structures of Enzymes Bound to Graphene Oxide with a Protein Glue. *Langmuir* **2013**, *29*, 15643-15654.

34. Vicarelli, L.; Heerema, S. J.; Dekker, C.; Zandbergen, H. W. Controlling Defects in Graphene for Optimizing the Electrical Properties of Graphene Nanodevices. *ACS Nano* **2015**, *9*, 3428-3435.

35. Li, Y. Q.; Yu, T.; Yang, T. Y.; Zheng, L. X.; Liao, K. Bio-Inspired Nacre-like Composite Films Based on Graphene with Superior Mechanical, Electrical, and Biocompatible Properties. *Adv. Mater.* **2012**, *24*, 3426-3431.

36. Yun, Y. J.; Hong, W. G.; Kim, W. J.; Jun, Y.; Kim, B. H. A Novel Method for Applying Reduced Graphene Oxide Directly to Electronic Textiles from Yarns to Fabrics. *Adv. Mater.* **2013**, *25*, 5701-5705.

37. Šimek, P.; Sofer, Z.; Jankovský, O.; Sedmidubský, D.; Pumera, M. Oxygen-Free Highly Conductive Graphene Papers. *Adv. Funct. Mater.* **2014**, *24*, 4878-4885.

38. Xu, Z.; Zhang, Y.; Li, P.; Gao, C. Strong, Conductive, Lightweight, Neat Graphene Aerogel Fibers with Aligned Pores. *ACS Nano* **2012**, *6*, 7103-7113.

39. Vallés, C.; David Núñez, J.; Benito, A. M.; Maser, W. K. Flexible conductive graphene paper obtained by direct and gentle annealing of graphene oxide paper. *Carbon* **2012**, *50*, 835-844.

40. Chen, H.; Müller, M. B.; Gilmore, K. J.; Wallace, G. G.; Li, D. Mechanically Strong, Electrically Conductive, and Biocompatible Graphene Paper. Adv. Mater. **2008**, 20, 3557-3561.

41. Lian, M.; Fan, J.; Shi, Z.; Zhang, S.; Li, H.; Yin, J. Gelatin-assisted fabrication of graphene-based nacre with high strength, toughness, and electrical conductivity. *Carbon* **2015**, *89*, 279-289.

42. Ferrari, A. C.; Bonaccorso, F.; Fal'ko, V.; Novoselov, K. S.; Roche, S.; Boggild, P.; Borini, S.; Koppens, F. H. L.; Palermo, V.; Pugno, N. *et al.* Science and technology roadmap for graphene, related two-dimensional crystals, and hybrid systems. *Nanoscale* **2015**, *7*, 4598-4810.